学位論文

Numerical studies of solar chromospheric jets

(太陽彩層ジェットの数値的研究)

平成27年12月博士（理学）申請

東京大学大学院理学系研究科
地球惑星科学専攻

飯島陽久

Numerical studies of solar chromospheric jets

by

Haruhisa Iijima

A Dissertation

submitted to The University of Tokyo

in partial fulfillment of the requirements for the degree of

Doctor of Philosophy

Department of Earth and Planetary Science

December, 2015

Abstract

The solar chromospheric jet is one of the most characteristic structures near the solar surface. The quantitative understanding of chromospheric jets is of substantial importance for not only the partially ionized phenomena in the chromosphere but also the energy input and dissipation processes in the corona. In this dissertation, the formation and dynamics of chromospheric jets are investigated using the radiation magnetohydrodynamic simulations.

We newly develop a numerical code for the radiation magnetohydrodynamic simulations of the comprehensive modeling of solar atmosphere. Because the solar chromosphere is highly nonlinear, magnetic pressure dominated, and turbulent, a robust and high-resolution numerical scheme is required. In Chapter 2, we propose a new algorithm for the simulation of magnetohydrodynamics. Through the test problems and accuracy analyses, the proposed scheme is proved to satisfy the requirements.

In Chapter 3, the effect of the non-local radiation energy transport, Spitzer-type thermal conduction, latent heat of partial ionization and molecule formation, and gravity are implemented to the magnetohydrodynamic code. The numerical schemes for the radiation transport and thermal conduction is carefully chosen in a view of the efficiency and compatibility with the parallel computation.

Based on the developed radiation magnetohydrodynamic code, the formation and dynamics of chromospheric jets are investigated. In Chapter 4, we investigate the dependence of chromospheric jets on the coronal temperature in the two-dimensional simulations. Various scale of chromospheric jets with the parabolic trajectory are found with

the maximum height of 2–8 Mm, lifetime of 2–7 min, maximum upward velocity of 10–50 km/s, and deceleration of 100–350 m/s^2. We find that chromospheric jets are more elongated under the cool corona and shorter under the hot corona. We also find that the pressure gradient force caused by the periodic shock waves accelerates some of the short chromospheric jets. The taller jets tend to follow ballistic trajectory. The contribution of the coronal conditions are quantitatively modeled in the form of a power law based on the amplification of shock waves under the density stratified medium.

In Chapter 5, the role of the magnetic field is investigated using the two-dimensional simulations. We distinguish the contribution of the corona and magnetic field using the power law. The average magnetic field strength produces only a small effect on the scale of chromospheric jets. The observed regional difference is mainly explained by the difference of the coronal conditions, which is caused by the different magnetic field structure. We also find shorter chromospheric jets above the strong magnetic flux tube. This is in contrast to the observational studies.

In Chapter 6, a three-dimensional simulation is presented to investigate the effect of three-dimensionality on the scale of chromospheric jets and the dependence on the photospheric magnetic field structure. The tall chromospheric jets with the maximum height of 10–11 Mm and lifetime of 8–10 min are formed. These tall jets are located above the strong magnetic field concentration. This result is different from the two-dimensional study and consistent with the observational reports. The strongly entangled chromospheric magnetic field drives these tall chromospheric jets through the Lorentz force. We also find that the produced chromospheric jets form a cluster with the diameter of several Mm with finer strands.

In Chapter 7, we summarize and discuss our new findings and their implications for the solar chromospheric jets. The regional difference of chromospheric jets is explained through the coronal temperature and density, which is produced by the heating process with the different strength and structure of the magnetic field. The observational relation between the magnetic network and chromospheric jets are interpreted through the mag-

netic energy release in the complex photospheric magnetic field with mixed-polarity. The formation of the horizontal structure like the multi-threaded nature of solar spicules and the possible driver of observed chromospheric jets are also discussed. The comprehensive numerical model developed in this dissertation allows various future applications for the dynamics on the sun.

The most important new results in this dissertation are (1) the reproduction of tall ($>$ 6 Mm) chromospheric jets using the simulation with realistic physical processes, (2) the quantification of the effect of the coronal condition and magnetic field on the scale of jets, and (3) the reproduction of the cluster of jets with fine-scale internal structure. We conclude that the solar chromospheric jets reflect the information of not only the magnetic field but also the corona and fine-scale motion in the lower atmosphere.

Acknowledgments

I would like to express my sincere gratitude to my supervisor, Takaaki Yokoyama, for his great encouragement and patience during my PhD course.

Special thanks goes to Ryoji Matsumoto, Kengo Nakajima, Masaharu Matsumoto and other participants on the JHPCN project for the valuable discussions and comments on the computational algorithm.

I would also like to thank Mats Carlsson and researchers in Institute of Theoretical Astrophysics, The University of Oslo, Norway, for their help and insightful discussions during my stay.

Many thanks to my colleagues in Yokoyama lab, Yusuke Iida, Naomasa Kitagawa, Shin Toriumi, Hideyuki Hotta, Yuki Matsui, Takafumi Kaneko, Shuoyang Wang, Tetsuya Nasuda, Shunya Kono, Munehito Shoda, Chiaki Ichimura, Yoshiaki Oi, and Yikang Wang, and other members in the Solar-Terrestrial Physics Colloquium for the helpful discussions and making my years in graduate school more than academic.

I would like to acknowledge the researchers in the Kyoto University, ISAS/JAXA, NAOJ, Nagoya University, and many other institutes for the valuable discussions.

I have been supported by JSPS, JHPCN, HPCI, and the Program for Leading Graduate Schools, MEXT, in Japan. Numerical computations were carried out on the Cray XC30 supercomputer at CfCA/NAOJ and the Fujitsu PRIMEHPC FX10 System in the Information Technology Center, The University of Tokyo.

Finally, a special note of thanks is extended to my family for their long-standing support and encouragement.

Contents

Chapter 1

General introduction

1.1 Structure of solar atmosphere

Figure 1.1 shows the semi-empirical model chromosphere in quiet regions given by Avrett & Loeser (2008). The vertical variation of physical quantities is chosen so that the simulated intensity matches the observed spectra. The magnetic field is highly structured and non-uniform in the solar atmosphere. At least, we can argue that the scale height of horizontally averaged magnetic pressure is longer than of gas pressure because of the conservation of magnetic flux. The vertical variation of the magnetic pressure is adopted from the simplified approach in Leake et al. (2014) defined by:

$$\begin{aligned} P_m(z) &= P_m(0) \exp\left(-\gamma_m \int_0^z \frac{dz}{H_p}\right) \\ &= P_m(0) \left(\frac{P_g(z)}{P_g(0)}\right)^{\gamma_m} \end{aligned} \tag{1.1}$$

Here, we assume that the scale height of the magnetic pressure is proportional to the scale height of gas pressure H_p. We assume the proportional constant $\gamma_m = 0.75$ and the strength of photospheric magnetic field of 1000 G.

The gas temperature monotonically decreases from the center of the sun to the surface. It becomes minimum around the height of 600 km. Above this minimum, the temperature

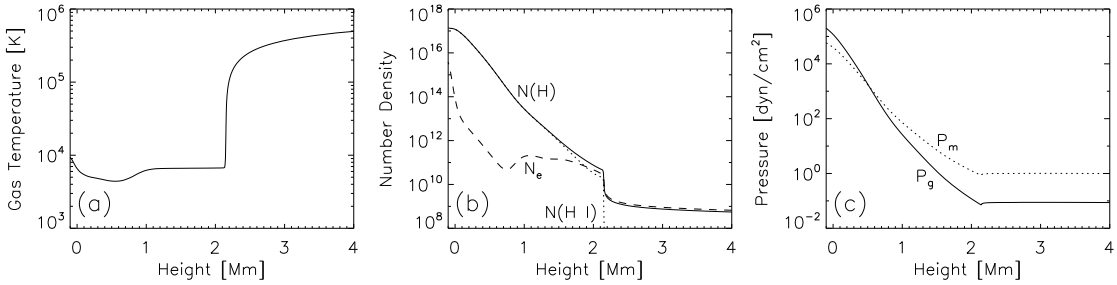

Figure 1.1: Vertical structure of solar atmospheric model by Avrett & Loeser (2008). Gas temperature T (panel (a)), Number density of total (neutral plus ionized) hydrogen $N(\mathrm{H})$ (panel (b), solid line), neutral hydrogen $N(\mathrm{HI})$ (panel (b), dotted line), electron N_e (panel (b), dashed line), gas pressure P_g (panel (c), solid line), and magnetic pressure P_m (panel (c), dotted line) are shown. The height dependence of magnetic pressure Eq. (1.1) is assumed, using the photospheric magnetic field strength of 1000 G.

gradually increases in the chromosphere. At the chromosphere-corona transition region, the temperature suddenly increases and reaches the coronal temperature. The transition region has small width of several tens to hundreds of kilometers. The mass density and temperature varies about two orders of magnitude below and above this thin region without the large variation of gas pressure. Therefore, the transition region is sometimes assumed to be a contact discontinuity. The plasma in the chromosphere is partially ionized by the low temperature of several thousand K. The ionization degree becomes lower than 10^{-4}. Because of this, various physical processes of the partially ionized plasma are important in the chromosphere, such as the ambipolar magnetic diffusion by the drift motion between the neutrals and ions and the non-equilibrium ionization/excitation coupled with the radiation. Therefore, the solar chromosphere is one of the best places to observe the behavior of the partially ionized plasma in the universe. See Leake et al. (2014) for a detailed review.

The chromosphere has small gas pressure scale height considering the small thickness of chromosphere, which makes the six orders of magnitude of the variation of gas pressure from the photosphere to the upper chromosphere. Under the strong stratification, the acoustic waves excited by the upper convection zone (Nordlund & Stein, 2001; Stein &

Nordlund, 2001) easily steepen into shock waves. The chromosphere is filled with strong shock waves. The small gas pressure scale height also produces the rapid variation of the plasma beta (gas pressure divided by magnetic pressure) because the magnetic pressure has the larger scale height by the conservation of magnetic flux. This strong variation of plasma condition affects the magnetohydrodynamic (MHD) waves in various ways such as reflection and mode conversion (Rosenthal et al., 2002; Bogdan et al., 2003).

Understanding of the chromosphere leads to understand the coronal heating problem, which is one of the most important problems in the solar physics. Because of the large mass density in the chromosphere, the radiative energy loss in the chromosphere is much greater than in the corona. For example, the chromospheric radiative energy loss in the quiet region that is required to maintain the chromospheric temperature, is typically 4×10^6 erg cm^{-2} sec^{-1}, which is ten times greater than the coronal total (conductive plus radiative) energy loss of 3×10^5 erg cm^{-2} sec^{-1} (Withbroe & Noyes, 1977). The most of the energy injected from the convection zone dissipates in the chromosphere without reaching the corona. The quantitative understanding of the response of the chromosphere to the energy injection from the photosphere is inevitable to understand the coronal heating problem.

Most of the energy injected into the chromosphere originally comes from the turbulent motion in the convection zone. The granulation (Figure 1.2, left column) is one of the clearest structures in the photosphere. It has the typical diameter of 1 Mm, and the typical lifetime of 10 min. This structure is understood as the overshoot from the upper convection zone to the convectively stable photosphere. The Doppler velocity map in the photosphere also suggests the existence of the larger scale structure called supergranulation (Leighton et al., 1962). The typical diameter of the supergranulation is 30 Mm and the typical lifetime is one day.

The turbulent convective motion generates the magnetic flux ubiquitously in the convection zone from the small scale of sub-granular size to the global scale. This dynamo process produces various magnetic structures in the solar surface. (Figure 1.3). Espe-

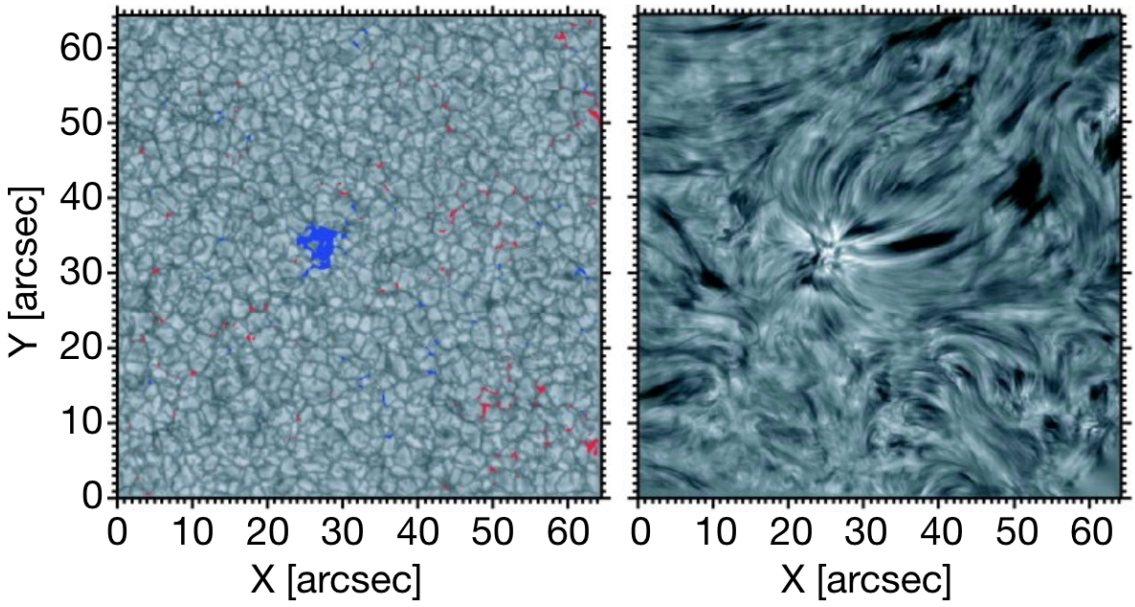

Figure 1.2: Left: Photospheric granulation pattern in continuum images. Positive (blue) and negative (red) magnetic flux are also shown. Right: Chromosphere observed in Hα line core (top) and summed Hα ± 35 pm (bottom). Image extracted from Rouppe van der Voort et al. (2007).

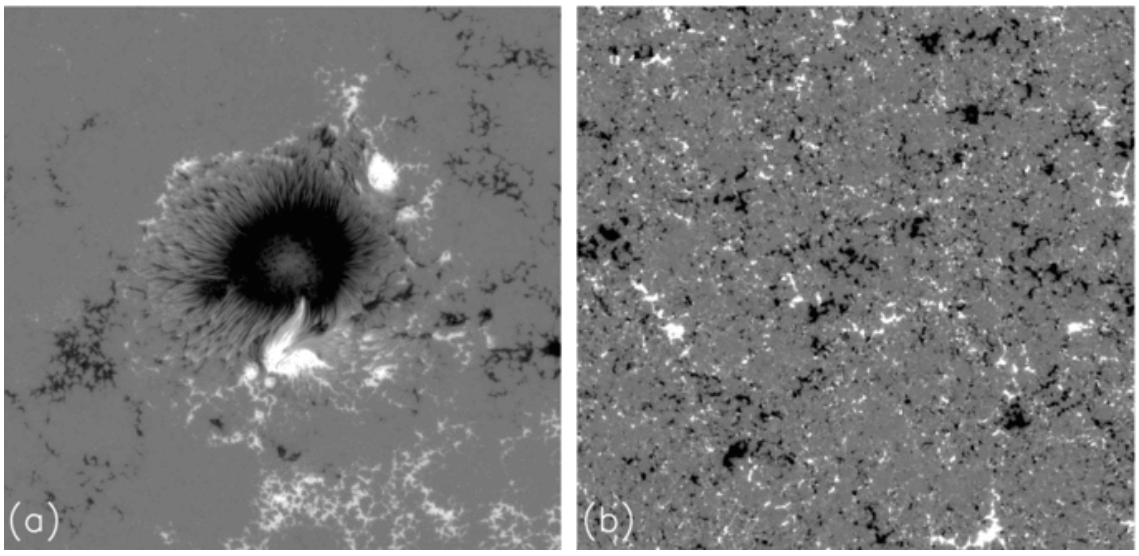

Figure 1.3: Distribution of positive (white) and negative (black) line-of-sight magnetic field around a sunspot (left panel) and in a quiet region (right panel), observed by Hinode SOT/SP. Both images cover the same area of 110×110 Mm^2. Image extracted from Parnell et al. (2009).

Table 1.1: Typical parameters and observed jets in active regions, quiet regions, and coronal holes. The values of coronal temperature are taken from Withbroe & Noyes (1977).

	Active region	Quiet region	Coronal hole
Temperature at 1.1 $R_\odot$ [MK]	2.5	1.1–1.6	1
Flux imbalance [G]	~ 100	~ 10	~ 10
Typical chromospheric jets	Dynamic fibrils	Spicules, Mottles	Spicules

cially, the magnetic network around the boundary of the supergranular cells often have a counterpart in the chromosphere called the chromospheric network (Simon & Leighton, 1964), which is supposed to have important role in the chromospheric dynamics. The convective motion with the strong magnetic field concentration in the photosphere drives various MHD waves and injects the energy into the upper atmosphere.

1.2 Observation of solar chromospheric jets

Various jets are observed in the solar chromosphere. In this section, we mainly review relatively small-scale jets that fill the chromosphere. The typical parameters and chromospheric jets in observed regions are summarized in Table 1.1. More detailed review on the observational studies were provided by Beckers (1968, 1972), Zaqarashvili & Erdélyi (2009), and Tsiropoula et al. (2012).

1.2.1 Spicules

Spicules (Figure 1.4) are the most representative and common chromospheric jets. They are the long and thin jets observed at the solar limb in quiet regions and coronal holes. The jets were first observed by Secchi (1875). The name of "spicules" is given by Roberts (1945). Spicules consist of the cool (9,000–17,000 K) and dense (10^{10}–10^{11} cm^{-3}) chromospheric plasma (Beckers, 1972).

Beckers (1972) reported that the typical spicule has the maximum height of 4–10 Mm, lifetime of 1–7 min, and maximum upward velocity of 20–100 km/s. These observed

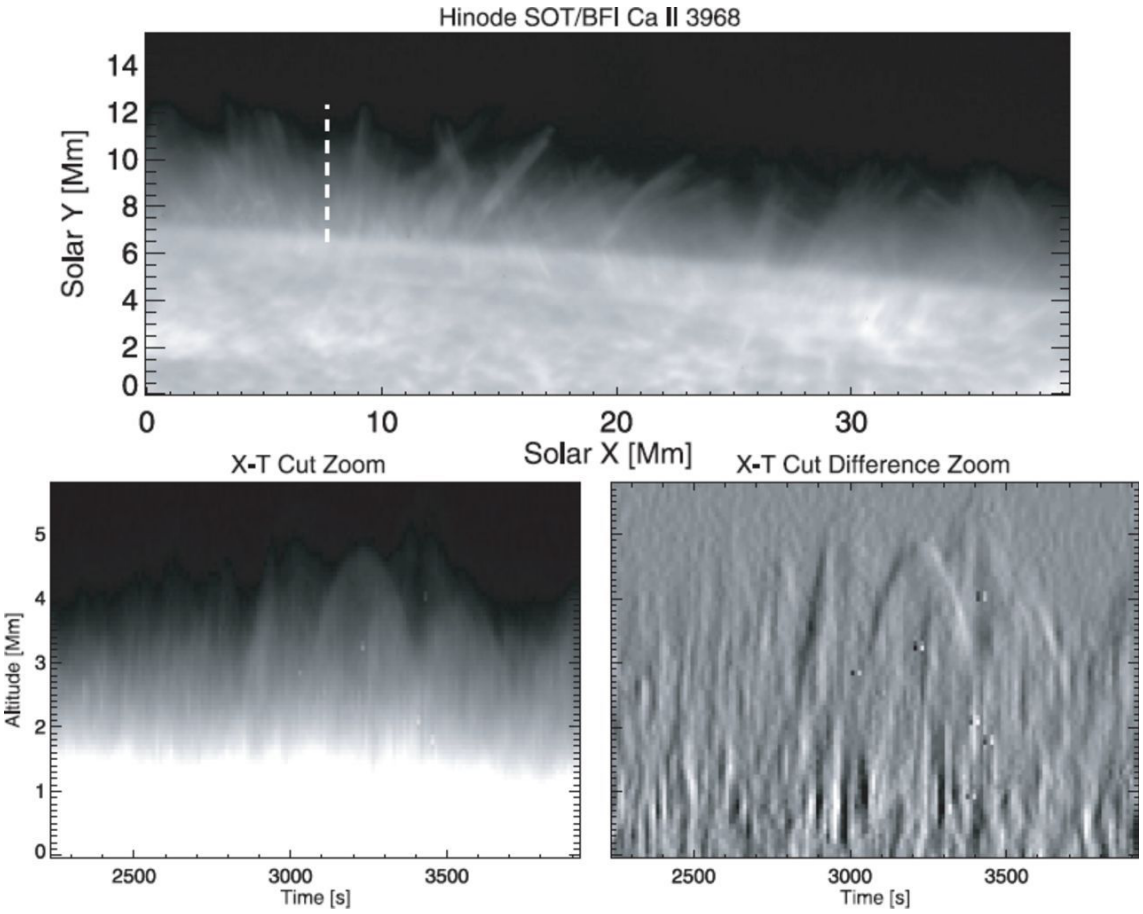

Figure 1.4: Spicules observed at the solar limb of a quiet region, in Hinode SOT/BFI Ca II H 396.8 nm data. A snapshot of observed intensity (top panel) and space-time plots along the white dashed line in the top panel, for the original data (bottom left panel) and time-differenced data (bottom right panel). Image extracted from De Pontieu et al. (2007b).

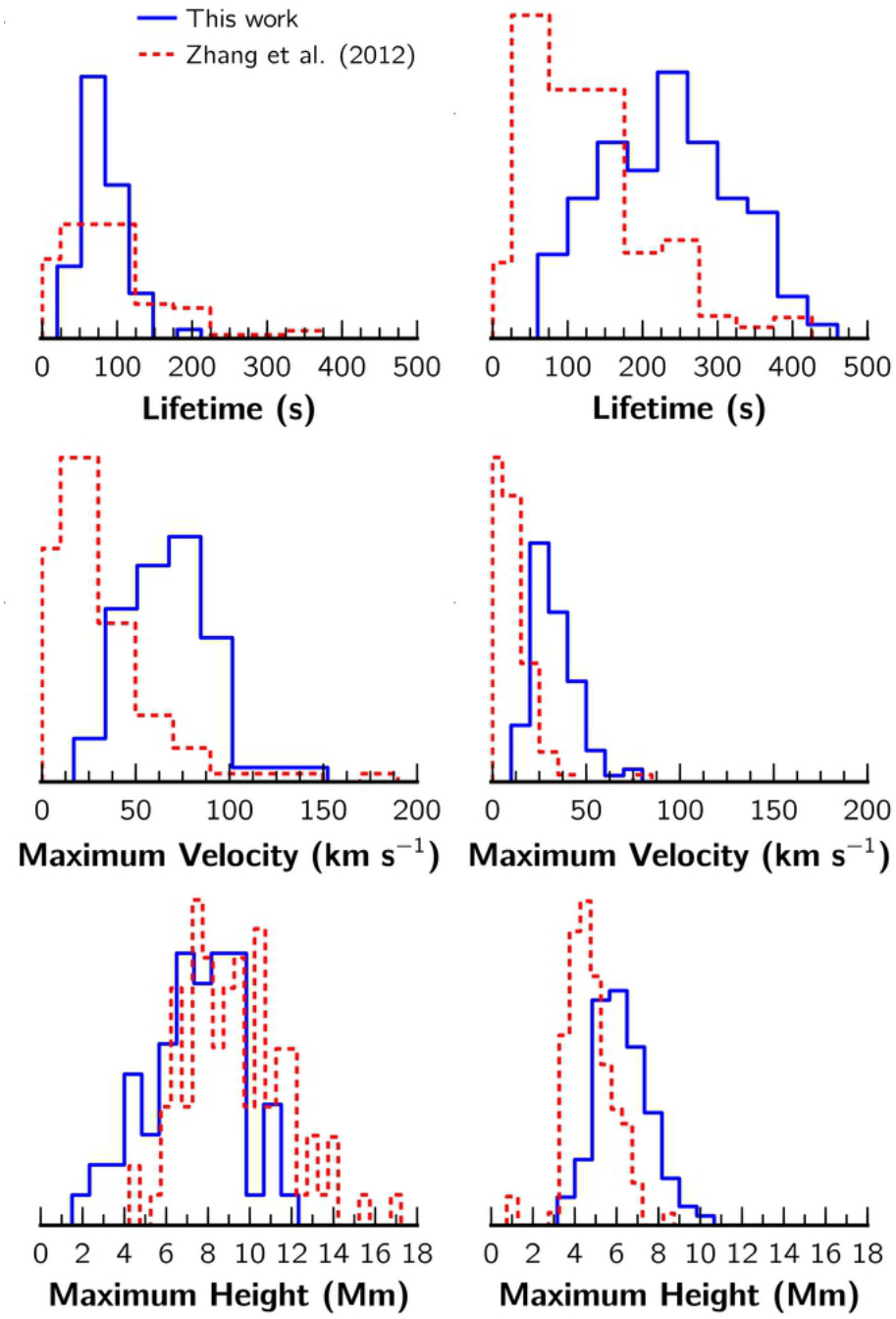

Figure 1.5: Normalized histograms of the chromospheric jets observed in a coronal hole (left column) and a quiet region (right column). The physical parameters derived by Pereira et al. (2012) (blue solid line) and Zhang et al. (2012) (red dashed line) are shown. Image extracted from Pereira et al. (2012).

values depends on the observed region, e.g., spicules in coronal holes are larger than in quiet regions (e.g., Zhang et al., 2012; Pereira et al., 2012, see also Figure 1.5).

The top of spicules shows both upward motion followed by downward motion, only upward motion, and only downward motion (Beckers, 1972). When both upward and downward motions are observed, we can estimate the deceleration of vertical motion assuming the parabolic trajectory. De Pontieu et al. (2007b) report that the deceleration is around 50–400 m/s^2. Zhang et al. (2012) report 130 m/s^2 as an average in the quiet region and Pereira et al. (2012) report 182–343 m/s^2.

The width of spicules is often defined as the full-width-half-maximum of the radiative emission. Beckers (1968) reported the typical width of 700–2500 km. This parameter is affected by the spatial resolution, observational seeing, and observed wavelength. It is sometimes reported that spicules have width smaller than several hundreds of kilometers (e.g., De Pontieu et al., 2007b; Pasachoff et al., 2009; Zhang et al., 2012; Pereira et al., 2012).

De Pontieu et al. (2007b) reported a new kind of spicules with much higher velocity, shorter lifetime, and only upward motion. This phenomenon is called "type II spicule". The bottom right panel in Figure 1.4 shows type II spicules with the lifetime of around 1 min, superposed on longer living classical type I spicules with parabolic trajectory. The existence of type II spicules is still under debate. Zhang et al. (2012) reported that they could not find any evidence of type II spicules in the same data set of De Pontieu et al. (2007b). On the other hand, Pereira et al. (2012) analyzed the same data set and reported that most of spicules observed in quiet regions and coronal holes exhibit linear trajectory (only upward motion) and do not show parabolic trajectory. They argued that most of spicules should be categorized as type II spicules.

Pereira et al. (2014) reported the multi-wavelength observation of spicules in the quiet region and found that many spicules observed in the Ca II H line with the linear trajectory have the parabolic trajectory in other wavelength with higher formation temperature, like Mg II k and Si IV lines. They interpreted this results as a consequence of the heating

during the upward motion of type II spicules. Skogsrud et al. (2015) reported the statistical analysis of spicules in the multi-wavelength observation. They argue that the type II spicules have parabolic path like type I spicules, but type II spicules are more violent and undergo heating. Further questions will be raised on the type II spicules, like whether type I and II spicules have different drivers or they are the two extreme cases from a continuous distribution.

1.2.2 Disk-counterparts of type II spicules

Rutten (2006, 2007) found brighter and thinner structures than mottles in the Ca II H line center image. The structures are named "straws". De Pontieu et al. (2007b) argued that straws are the disk-counterpart of type II spicules. The dark and thin structures called rapid blue-shifted events (also called as rapid blue-shifted excursions or RBEs) are observed in the blue wing of Ca II 854.2 nm line (Langangen et al., 2008b). They have the typical length of 1.2 Mm, width of 0.5 Mm, and lifetime of 45 s. Rouppe van der Voort et al. (2009) found similar structures in the blue wing of Hα. The Doppler velocity of RBEs in Hα is slightly larger than Ca II 854.2 nm, but the length and lifetime are roughly consistent.

1.2.3 Mottles

Mottles are dark (absorbing) features in the chromospheric lines observed on the disk in quiet regions (Figure 1.2, middle column). Suematsu et al. (1995) reported that they have the maximum length of 2–10 Mm, extension velocity of 10–30 km/s, and lifetime of 5–15 min. Mottles are found near the boundary of magnetic network cells (Suematsu et al., 1995), and considered to be the disk-counterpart of spicules in quiet regions (e.g., de Jager, 1957; Bhavilai, 1965; Suematsu et al., 1995). Tsiropoula & Schmieder (1997) estimated that mottles have the mass density of 1.1×10^{-13} g/cm^3, electron number density of 3.4×10^{10} cm^{-3}, and temperature of 10,000–14,000 K in average.

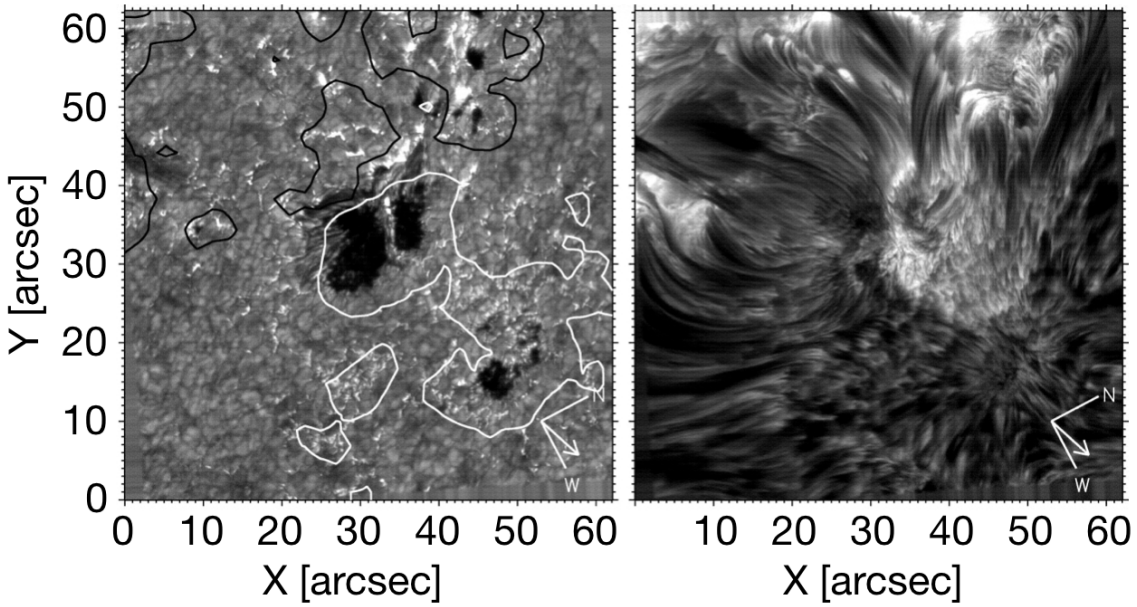

Figure 1.6: Active region observed in Hα wideband (left) and Hα line center (right) taken by Swedish 1 m Solar Telescope (SST). Image extracted from De Pontieu et al. (2007a).

Mottles have upward motion followed by downward motion from the measurement of Doppler shift (Beckers, 1963) and apparent motion from the radiative intensity (Suematsu et al., 1995). Rouppe van der Voort et al. (2007) tracked the trajectory of mottles and found that the maximum upward velocity is roughly proportional to the deceleration, like dynamic fibrils. They also pointed out that tracking the motion of mottles is often difficult due to the diffuse nature of the top of mottles.

1.2.4 Dynamic fibrils

Dynamic fibrils are dark structures observed on the disk near active regions (Figure 1.6). They are considered to be the active region counterpart of mottles. The trajectory of dynamic fibrils is more precisely determined than mottles. Hansteen et al. (2006) and De Pontieu et al. (2007a) estimated the maximum length, lifetime, maximum velocity and deceleration assuming the parabolic path (Figure 1.7). They found the correlation between maximum velocity and deceleration similar to that of mottles. They further argued that mottles and dynamic fibrils share the same driver of acoustic p-mode oscillation in the

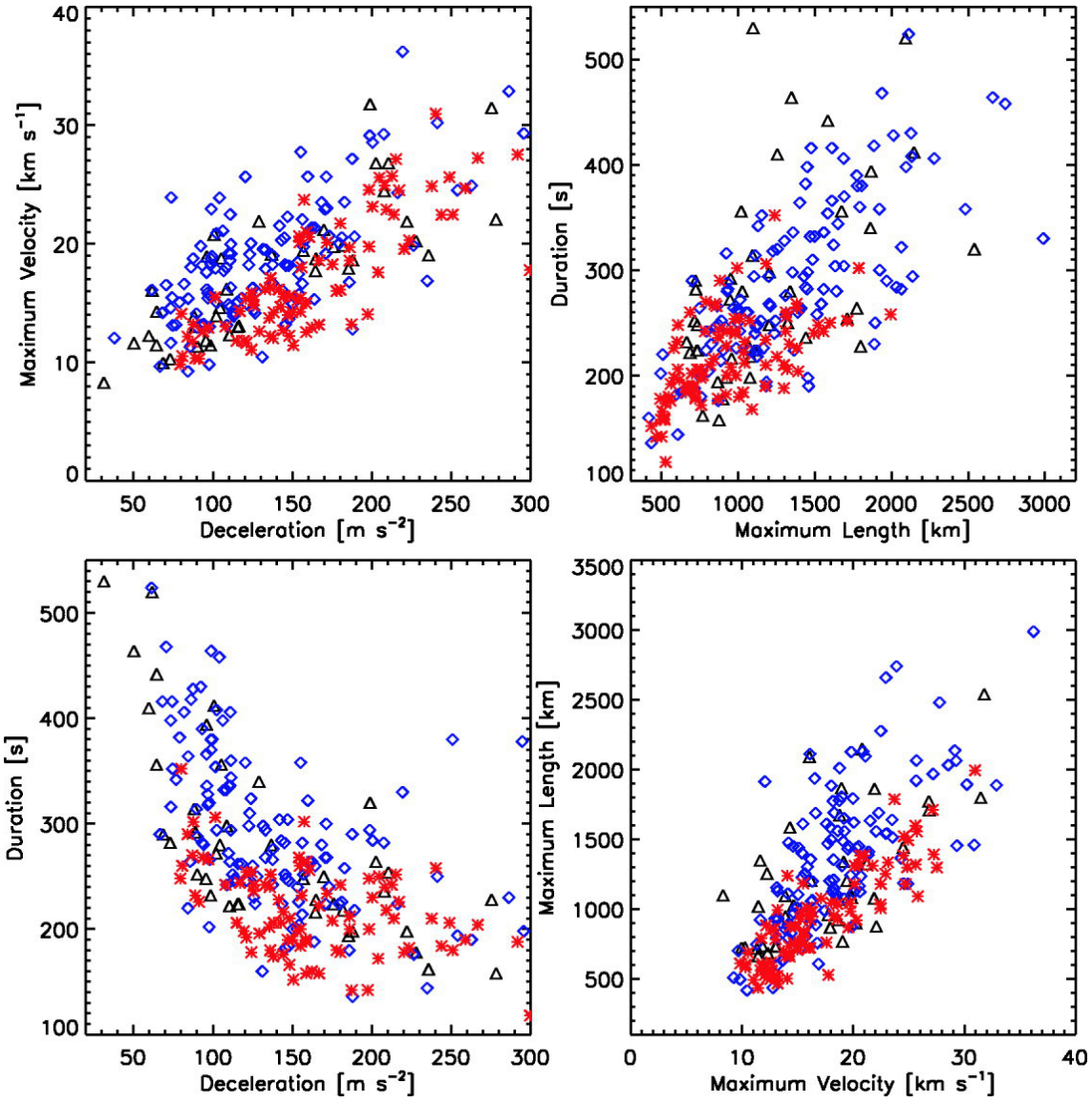

Figure 1.7: Scatter plots on the parabolic trajectory of dynamic fibrils. Deceleration vs. maximum velocity (top left), maximum length vs. duration (top right), deceleration vs. duration (bottom left), and maximum velocity vs. maximum length (bottom right) are shown. Image extracted from De Pontieu et al. (2007a).

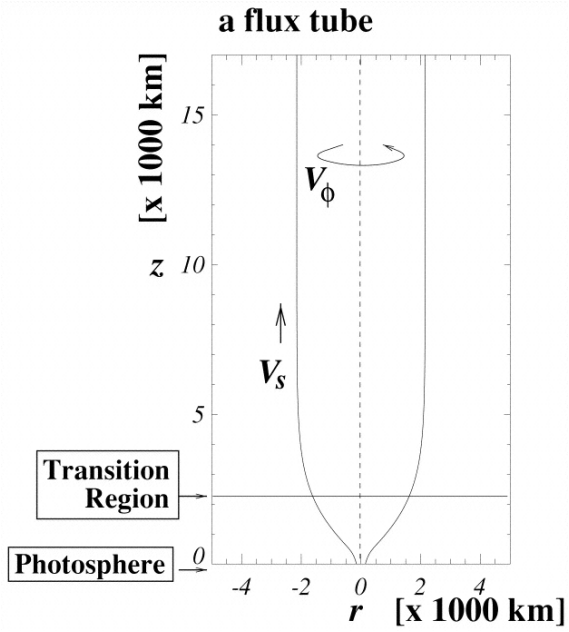

Figure 1.8: Shape of the magnetic flux tube assumed in the one-dimensional numerical study by Kudoh & Shibata (1999). Image extracted from Kudoh & Shibata (1999).

photosphere. The dynamic fibrils are also observed in other wavelengths (Langangen et al., 2008a; Pietarila et al., 2009; Anan et al., 2010) and roughly consistent with the Hα dynamic fibrils.

1.3 Theoretical and numerical approach

Many theoretical and numerical studies have been devoted on the mechanism of chromospheric jets. In this section, we introduce the three representative models of chromospheric jets: (1) acoustic wave model, (2) Alfvén wave model, and (3) magnetic reconnection model. Sterling (2000) provided more detailed review mainly on the dynamical one-dimensional numerical studies.

1.3.1 Acoustic wave models

The convective motion makes strong magnetic field concentrations in the photosphere through flux expulsion (e.g., Galloway & Weiss, 1981) and convective intensification

(e.g., Parker, 1978; Spruit, 1979; Schüssler, 1990). The plasma beta in the convectively collapsed magnetic flux tubes is equal or lower than unity. The flux tubes act as the guide of MHD waves, like slow-mode magneto-acoustic and Alfvén waves. This allows to approximate the vertical dynamics inside the flux tube in the one-dimensional (magneto-)hydrodynamic models (Figure 1.8).

One of the proposed models is driven by acoustic waves (e.g., Thomas, 1948; Uchida, 1961; Osterbrock, 1961; Parker, 1964; Suematsu et al., 1982; Shibata & Suematsu, 1982; Sterling et al., 1993). The photospheric convective motion produces the acoustic perturbation inside the flux tube. This perturbation propagates along the magnetic field line. In these models, the magnetic field acts only as the wave guide of slow-mode acoustic waves and the fundamental picture is understood from the one-dimensional hydrodynamics.

The acoustic waves propagate upward in the stratified chromosphere. In the WKB approximation, the acoustic wave conserves the energy flux, i.e., $S\rho V_{\parallel}^2 C_s = \mathrm{constant}$. Here S is the cross-section of the magnetic flux tube, C_s is the sound speed, and $V_{\parallel}$ is the velocity parallel to the magnetic field. This relation is reduced to $V_{\parallel} \propto (S\rho C_s)^{-1/2}$. Under the strong density stratification in the chromosphere, the acoustic waves are rapidly amplified and form shock waves. Once the shock front is formed, this dependency becomes weaker. According to the semi-analytic study of the shock wave propagation in the isothermal stratification by Ôno et al. (1960), the dependency becomes $V/C_s \propto P^{-0.236}$.

The chromospheric shock waves hit the chromosphere-corona transition region, which is assumed to be a contact discontinuity. The transition region is elevated through the shock-transition region interaction (e.g., Hollweg, 1982). This elevated cool and dense chromospheric material is observed as chromospheric jets.

In the real solar atmosphere, acoustic waves are often periodic. The acoustic p-mode oscillation has the relatively long period of 3–5 min. Under the short gas pressure scale height near the temperature minimum, acoustic waves with the period longer than the acoustic cut-off period of several minutes become evanescent. The inclination of the magnetic flux tube is suggested as a candidate to relax this cut-off (Suematsu, 1990; De

Pontieu et al., 2005; Heggland et al., 2007). The rebound shock model (Hollweg, 1982) uses this limitation as another process for the production of chromospheric jets. The acoustic waves with the longer period are trapped in the upper photosphere, which excites a train of upward-propagating shocks with relatively small amplitude. The transition region is gradually lifted upward by the continual interactions with these rebound shocks.

The chromospheric jets with the parabolic trajectory are usually assumed to be decelerated by the gravity. Heggland et al. (2007) suggests a new deceleration process, called "shock deceleration hypothesis", in which the expansion waves in the periodic N-shaped shock waves decelerate the transition region. In this hypothesis, the deceleration should be proportional to the maximum upward velocity, which is consistent with the correlation observed for mottles and dynamic fibrils. Following this discussion, Hansteen et al. (2006) and De Pontieu et al. (2007a) suggested the p-mode oscillation as the origin of mottles and dynamic fibrils.

1.3.2 Alfvén wave models

The Alfvén waves are also suggested as a candidate of the driver of chromospheric jets (Hollweg et al., 1982; Kudoh & Shibata, 1999). The photospheric convection with the strong magnetic field concentration makes the incompressible waves not only the acoustic waves (e.g., Steiner et al., 1998). Such incompressible (swaying and/or torsional) motion is also observed in the photosphere and chromosphere (e.g., Ulrich, 1996; Fujimura & Tsuneta, 2009; Wedemeyer-Böhm et al., 2012). Zaqarashvili & Erdélyi (2009) review the various waves propagating along spicules. In the WKB approximation, Alfvén waves follow the relation of $V_\perp \propto \rho^{-1/4}$ under the stratification. Here, $V_\perp$ is the velocity perpendicular to the magnetic field. Amplified nonlinear Alfvén waves forms the longitudinal (acoustic) waves through the magnetic pressure gradient. These acoustic waves steepen into shock waves and lift the transition region upward, as in the acoustic wave models. Hollweg (1992) also suggests the possibility of the reflection of Alfvén waves in

the strong slow-mode shock front, which contributes to the heating of chromosphere and acceleration of chromospheric jets.

The models mentioned above are mainly on the relatively low frequency Alfvén waves. There are models on the Alfvén waves with higher frequency. The low ionization degree in the chromosphere causes the magnetic diffusion like the ambipolar diffusion by the drift motion between neutrals and ions. According to Haerendel (1992) and De Pontieu (1999), high frequency Alfvén waves are damped by this effect and produces chromospheric jets. On the other hand, James & Erdélyi (2002) suggested that the acceleration of chromospheric jets are mainly by the formation of shock waves by the turbulent interaction of Alfvén waves.

1.3.3 Magnetic reconnection models

Various multi-dimensional magnetic reconnection models are suggested for the chromospheric jets (e.g., Uchida, 1969; Pikel'ner, 1969, 1971; Heggland et al., 2009; Singh et al., 2011; Takasao et al., 2013; Yang et al., 2013). A part of one-dimensional acoustic wave models introduced above sometimes assume the heating by the magnetic reconnection as the driver. The magnetic reconnection can accelerate the chromospheric material not only by the generation of shock waves but also by the magnetic tension force. (Takasao et al., 2013). This allows strong upward forcing in the low-beta chromosphere. This is the reason why the magnetic reconnection is sometimes assumed to be the driver of the type II spicules (e.g., De Pontieu et al., 2007b; Moore et al., 2011; Shimizu, 2015).

The magnetic reconnection requires the anti-parallel component of the magnetic field. The possible candidates are suggested, such as the interaction between the ambient field and emerging flux (Shibata et al., 2007; Singh et al., 2011; Moore et al., 2011) as in the models of X-ray coronal jets and Hα surges (Yokoyama & Shibata, 1995), kink instability of flux tube by the vortex in the photosphere (Pariat et al., 2009, 2010, 2015), and three-dimensional component reconnection by torsional motion (Shimizu, 2015). The sheared

field configuration in the sunspot penumbra (Nakamura et al., 2012) is also suggested as the origin of tiny transient chromospheric jets (Katsukawa et al., 2007).

The existence of the fast reconnection in the chromosphere is not clear because the chromosphere is collisional and partially ionized in contrast to the corona. Some features resembling to the reconnection current sheet were observed in the chromospheric anemone jets around the sunspot (Shibata et al., 2007; Singh et al., 2011). Parker (1963) and Brandenburg & Zweibel (1994) suggested that the ambipolar diffusion contributes to make thinner current sheet, which will enhance the magnetic reconnection. Leake et al. (2012) reported that the fast reconnection is expected under the chromospheric condition using the two-fluid (ions and neutrals) magneto-hydrodynamic simulations.

1.3.4 Effect of non-ideal physical processes

Abovementioned theoretical and numerical studies are relatively simplified models. In the real solar chromosphere, various effects like the radiative cooling, thermal conduction, latent heat from the partial ionization, multi-dimensional interaction of MHD waves and magnetic flux tubes should be considered for the quantitative understanding of chromospheric jets (e.g., Sterling & Mariska, 1990; Sterling et al., 1993; Guerreiro et al., 2013). Moreover, the energy injection processes, e.g., perturbation in the one-dimensional models and the structure of the magnetic field in the reconnection models, are assumed in these studies.

The uncertainties of the driving forces in the idealized models can be resolved by using the self-consistent dynamical model of the solar atmosphere with sufficiently realistic physical processes. Nordlund (1982) found that the radiation hydrodynamic simulation from the upper convection zone to the lower chromosphere with the effect of the radiative energy transport and latent heat by the partial ionization can reproduce the near-surface convection in the excellent accuracy (Figures 1.9 and 1.10). Bifrost code (Gudiksen et al., 2011) extended the upper boundary of the numerical box up to the corona and included

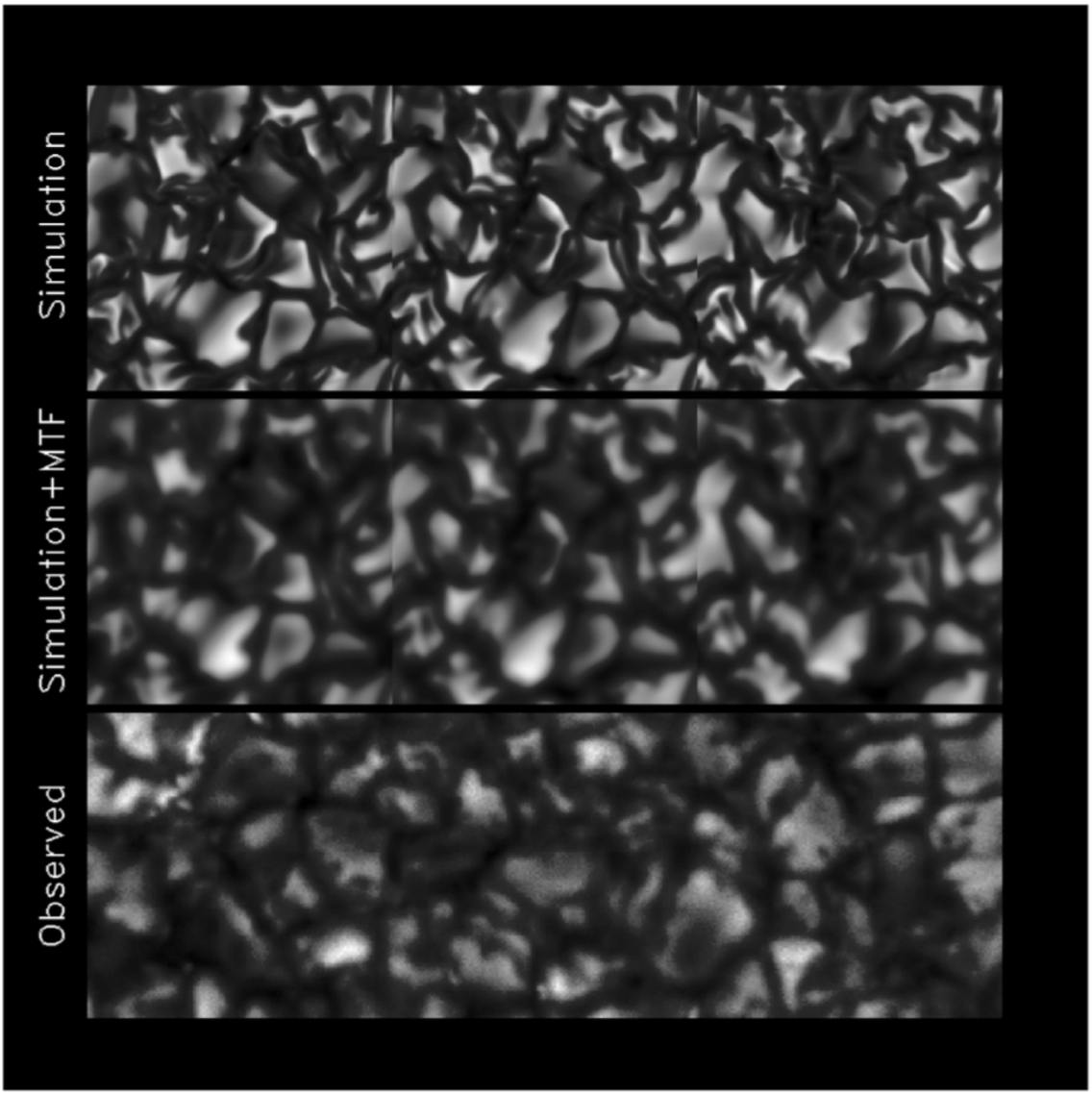

Figure 1.9: Comparison of emerging radiative intensity from the radiation hydrodynamic simulation of photospheric convection (Top), the simulation convolved with a point-spread function (Middle), and the observation by the Swedish Vacuum Solar Telescope on La Palma (Bottom). Image extracted from Stein & Nordlund (1998).

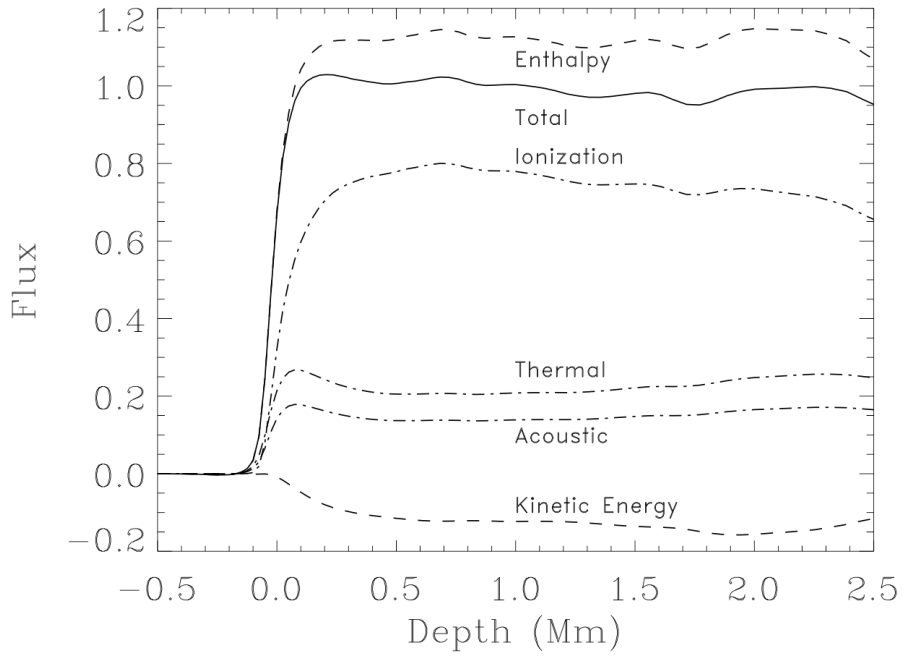

Figure 1.10: Vertical variation of horizontally and temporary averaged energy flux in the radiation hydrodynamic simulation of photospheric convection. Positive energy flux represents upward flux. Enthalpy flux $(e_{\rm int} + P)V_z$、 ionization energy (latent heat) flux $(e_{\rm int} - 3P/2)V_z$、 thermal energy flux $(3P/2)V_z$、 acoustic energy flux PV_z、 kinetic energy flux $(\rho V^2/2)V_z$、 and total energy flux $(e_{\rm int} + P + \rho V^2/2)V_z$ are shown. The energy transport by the horizontally uniform vertical mass transport is subtracted. The large fraction $(2/3)$ of the energy is transported as the ionization energy flux. Image extracted from Stein & Nordlund (1998).

the Spitzer-type thermal conduction, in addition to the radiation and latent heat, for the realistic modeling of the chromosphere and corona. This is the only code with such various physical processes and applied to various studies (e.g., Martínez-Sykora et al., 2008; Hansteen et al., 2010; Carlsson & Leenaarts, 2012; Hansteen et al., 2015). However, we could not cross-check nor validate the results without the other realistic code. There are also some problems in the numerical methods implemented in the code, which is reviewed in Chapter 3.

Heggland et al. (2011) investigated the propagation of chromospheric acoustic wave, especially on the effect of acoustic cut-off with inclined magnetic field in the two-dimensional simulations by the Bifrost code (Figure 1.11). Martínez-Sykora et al. (2009) analyzed the chromospheric jets found in the three-dimensional flux emergence simulation and reported the existence of various drivers. Martínez-Sykora et al. (2011) investigated the origin of one tall jet in the simulation assuming that it is the type II spicule. Martínez-Sykora et al. (2013) reported that the structure similar to the type II spicule have the density significantly smaller than the observed type II spicules. The common problem among these studies is that they could not reproduce tall (> 6 Mm) chromospheric jets, although the numerical setting is aimed to mimic quiet regions.

1.4 Motivation

The chromospheric jet is the most ubiquitous fundamental structure in the solar chromosphere. Its mysterious nature has been attracted many scientists for over 100 years. It is also crucially important to understand the various properties of chromospheric jets for the other scientific targets in the chromosphere as represented by the physical phenomena of partially ionized plasma and energy transport into the corona. For example, the latent heat by the ionization states changes the thermodynamic property of chromospheric plasma and the scale of chromospheric jets. The collision between neutrals and ions helps the fast magnetic reconnection in the collisional chromospheric plasma, which enhances

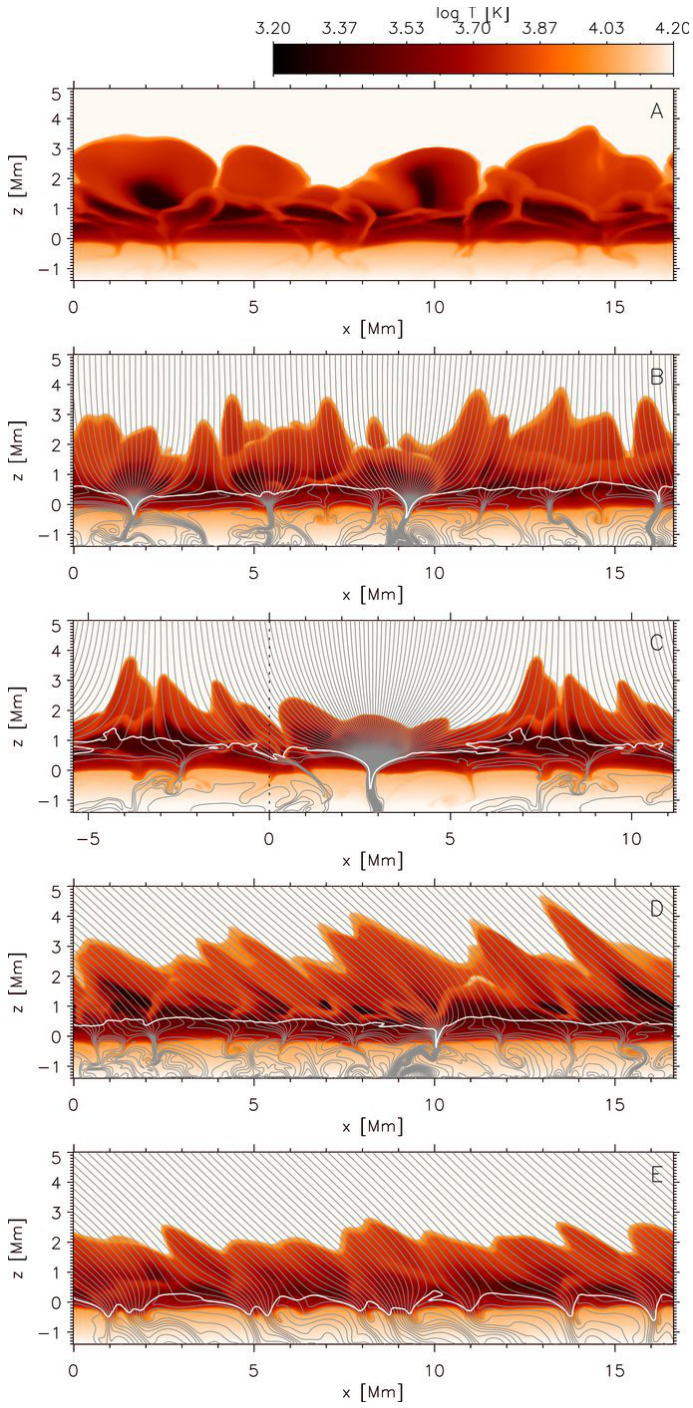

Figure 1.11: Snapshots from the two-dimensional radiation magnetohydrodynamic simulation by Heggland et al. (2011). Gas temperature from five different magnetic field configuration, i.e., extremely weak magnetic field (Case A), vertical magnetic field with moderate strength (Case B), strong expanding tube (Case C), inclined magnetic field with moderate strength (Case D), and inclined strong magnetic field (Case E), are shown. The white lines indicate $\beta = 1$. The gray lines indicate the magnetic field lines. Image extracted from Heggland et al. (2011).

the production of reconnection-driven jets. The repetition and strength of the MHD waves propagating along the jets should be quantified to understand the amount of energy dissipated in the chromosphere or transported into the corona. The formation process of chromospheric jets directly relates to the generation process of chromospheric waves. The quantitative understanding of chromospheric jets is inevitable for understanding the whole solar atmosphere.

The origin of chromospheric jets, especially of spicules, has been debated. Various simplified and realistic models are devoted on this topic. The multidimensional radiation MHD modeling of the chromosphere started recently, but it could not reproduce sufficiently tall (> 6 Mm) chromospheric jets as observed in quiet regions and coronal holes.

In this dissertation, we develop a new radiation MHD code with most important physical processes in the solar atmosphere for the comprehensive dynamical modeling of the solar atmosphere. Using the developed numerical code, we conduct radiation MHD simulations for the quantitative investigation of the formation and dynamics of chromospheric jets.

The rest of this dissertation is structured as follows. In Chapter 2, we propose a new algorithm for the high-resolution magnetohydrodynamic simulation in the strongly magnetic pressure-dominated medium, which is the case in the solar chromosphere and corona. In Chapter 3, we develop a new numerical code for the radiation magnetohydrodynamic simulations of solar atmosphere, from the upper convection zone to the corona. Based on the developed numerical code, the effect of coronal conditions on the scale and dynamics of chromospheric jets is investigated in Chapter 4. In Chapter 5, the role of magnetic field on the scale and formation process of chromospheric jets is studied. In Chapter 6, we investigate the effect of three-dimensionality on chromospheric jets. Finally, we summarize and discuss the results in Chapter 7.

Chapter 2

New numerical scheme of ideal magnetohydrodynamics

2.1 Introduction

The solar atmosphere is known to be turbulent and highly nonlinear region with low plasma beta. We need a high-resolution, upwind, and essentially divergence-free magnetohydrodynamics scheme to capture the dynamics in these regions correctly. In this study, we develop a new numerical scheme of ideal magnetohydrodynamics for the basis of the realistic simulation of solar atmosphere.

The numerical magnetohydrodynamics (MHD) simulation is an important tool for understanding the various nonlinear phenomena in fields related to the plasma dynamics, e.g., astrophysics, geophysics, and engineering. One of the difficulties with such multi-dimensional MHD simulations is the preservation of the constraint of the divergence-free magnetic field during the time integration process. The violation of the divergence-free condition causes artificial forces and heating in the simulation results, particularly when the magnetic energy is stronger than the internal energy of the plasma.

Various methods of maintaining the divergence-free constraint have been proposed. The central difference method on a collocated mesh (Tóth, 2000; Kawai, 2013) is one

of the simplest ways to maintain the divergence-free constraint with machine precision. However, it is difficult to avoid odd-even decoupling using this method. The divergence-cleaning method is widely used when small divergence errors are permitted, e.g., in the high plasma-beta region. Various divergence cleaning methods have been proposed, including the projection method (Brackbill & Barnes, 1980), eight-wave method (Powell et al., 1999), and Lagrangian multiplier method (Dedner et al., 2002). However, the divergence cleaning methods sometimes demands a significant computational cost to achieve sufficiently small divergence errors in the low plasma-beta region. The constrained transport method (Evans & Hawley, 1988) on a staggered mesh can construct an essentially divergence-free scheme without introducing odd-even decoupling. A more detailed comparison of the various methods used to control the divergence error can be found in Tóth (2000), Balsara & Kim (2004), and Miyoshi & Kusano (2011).

The constrained transport scheme requires the evaluation of the electric fields at cell edges. Many authors have discussed the construction of the electric field (Balsara & Spicer, 1999; Ryu et al., 1995; Londrillo & del Zanna, 2004; Gardiner & Stone, 2005; Lee & Deane, 2009; Balsara, 2010). One efficient way to perform this evaluation is with a divergence-free reconstruction of the magnetic field. This strategy was first proposed by Balsara (2001) for use in the prolongation process in adaptive mesh refinement. Balsara (2004) developed robust second-order MHD schemes on the basis of the proposed reconstruction. Balsara (2009) also proposed higher-order extensions (up to fourth order) of the method for centered WENO (Weighted Essentially Non-Oscillatory) reconstruction (Dumbser & Käser, 2007). Although this method is accurate and robust, it is designed for centered WENO reconstruction only. Thus, the scheme cannot be directly applied to a wide variety of reconstruction schemes, including PPM (Piecewise Parabolic Method; Colella & Woodward, 1984), WENO-JS (Jiang & Shu, 1996), MP5 (Suresh & Huynh, 1997), and WENO-Z (Borges et al., 2008).

Here we present a new form of the third-order divergence-free reconstruction of magnetic fields that can be applied to a wider variety of one-dimensional reconstruction pro-

cedures. In Section 2.2, we describe a new form of the divergence-free reconstruction. In Section 2.3, the details of the numerical scheme used for the test problem are described. In Section 2.4, we provide test problems to check the convergence rate. The proposed scheme is tested with several problems in Section 2.5.

2.2 New form of the divergence-free reconstruction of magnetic fields

In this section, we propose a new variant of third-order divergence-free magnetic fields reconstruction. We first drop some cross-differential terms in the multidimensional reconstruction for simplicity and for reducing the numerical cost. This process is described in subsection 2.2.1. Following this, we reinterpret the general one-dimensional reconstruction as a third-order reconstruction and present an efficient method for deriving the coefficient for the reconstruction. This step is described in subsection 2.2.2.

2.2.1 Third-order divergence-free reconstruction without cross-differential terms

Balsara (2009) described the derivation of the divergence-free reconstruction up to fourth-order. His original third-order form includes cross-differential terms to account for the multidimensional character of the reconstruction accurately. Here, we summarize a version in which some cross-differential terms are dropped.

To simplify the description, we assume that each control volume in a cell has been mapped to a unit cube of dimension $(x, y, z) \in [-1/2, 1/2] \times [-1/2, 1/2] \times [-1/2, 1/2]$. Following Balsara (2009), we choose the Legendre polynomial $P_n(x)$ as the basis function of the reconstruction. The explicit form of the Legendre polynomials is given as

follows:

$$P_0(x) = 1;\ P_1(x) = x;\ P_2(x) = x^2 - \frac{1}{12};\ P_3(x) = x^3 - \frac{3}{20}x \tag{2.1}$$

As the boundary conditions, the profile of the magnetic field on both sides of the cell face, normal to the component of the magnetic field, is given as follows:

$$\begin{aligned}
B_x(x = \pm 1/2, y, z) &= A^0_\pm + A^y_\pm P_1(y) + A^{yy}_\pm P_2(y) \\
&\quad + A^z_\pm P_1(z) + A^{zz}_\pm P_2(z) \\
B_y(x, y = \pm 1/2, z) &= B^0_\pm + B^x_\pm P_1(x) + B^{xx}_\pm P_2(x) \\
&\quad + B^z_\pm P_1(z) + B^{zz}_\pm P_2(z) \\
B_z(x, y, z = \pm 1/2) &= C^0_\pm + C^x_\pm P_1(x) + C^{xx}_\pm P_2(x) \\
&\quad + C^y_\pm P_1(y) + C^{yy}_\pm P_2(y)
\end{aligned} \tag{2.2}$$

Each of the coefficients is determined from one-dimensional reconstruction in the usual manner. The details of this are given in Section 2.2.2.

In Eq. (2.2), we dropped the cross-differential terms included in Balsara (2009), to reduce the numerical cost. This choice does not alter the edge averaged magnetic field reconstructed at the cell edge (e.g., at $(x, y, z) = (+1/2, -1/2, 0)$); however, it could potentially reduce the multidimensional accuracy of the reconstruction to second order in the worst case. In compensation for this reduction in accuracy, our scheme achieves high cost effectiveness in terms of the numerical cost and numerical dissipation.

The multidimensional profile of the reconstructed magnetic field inside each control

volume is expressed as follows:

$$
\begin{aligned}
B_x(x,y,z) &= a^0 + a^x P_1(x) + a^{xx} P_2(x) + a^{xxx} P_3(x) \\
&\quad + a^y P_1(y) + a^{yy} P_2(y) \\
&\quad + a^z P_1(z) + a^{zz} P_2(z) \\
&\quad + a^{xy} P_1(x) P_1(y) + a^{xyy} P_1(x) P_2(y) \\
&\quad + a^{xz} P_1(x) P_1(z) + a^{xzz} P_1(x) P_2(z) \\
B_y(x,y,z) &= b^0 + b^y P_1(y) + b^{yy} P_2(y) + b^{yyy} P_3(y) \\
&\quad + b^x P_1(x) + b^{xx} P_2(x) \\
&\quad + b^z P_1(z) + b^{zz} P_2(z) \\
&\quad + b^{xy} P_1(x) P_1(y) + b^{xxy} P_2(x) P_1(y) \\
&\quad + b^{yz} P_1(y) P_1(z) + b^{yzz} P_1(y) P_2(z) \\
B_z(x,y,z) &= c^0 + c^z P_1(z) + c^{zz} P_2(z) + c^{zzz} P_3(z) \\
&\quad + c^x P_1(x) + c^{xx} P_2(x) \\
&\quad + c^y P_1(y) + c^{yy} P_2(y) \\
&\quad + c^{xz} P_1(x) P_1(z) + c^{xxz} P_2(x) P_1(z) \\
&\quad + c^{yz} P_1(y) P_1(z) + c^{yyz} P_2(y) P_1(z)
\end{aligned}
\tag{2.3}
$$

This set of coefficients represents the minimum degree of freedom for a smooth profile and the divergence-free property inside the control volume when the boundary condition is given as in Eq. (2.2).

The coefficients in Eq. (2.3) are determined from two constraints. The first is that the boundary conditions at the cell faces must be normal to the component of the magnetic field (Eq. 2.2). By substituting, e.g., $x = \pm 1/2$, into Eq. (2.3) and comparing with Eq.

(2.2), we obtain the following:

$$
\begin{aligned}
a^0 &= \frac{1}{2}(A^0_+ + A^0_-) - \frac{1}{6}a^{xx};\ a^x = (A^0_+ - A^0_-) - \frac{1}{10}a^{xxx} \\
b^0 &= \frac{1}{2}(B^0_+ + B^0_-) - \frac{1}{6}b^{yy};\ b^y = (B^0_+ - B^0_-) - \frac{1}{10}b^{yyy} \\
c^0 &= \frac{1}{2}(C^0_+ + C^0_-) - \frac{1}{6}c^{zz};\ c^z = (C^0_+ - C^0_-) - \frac{1}{10}c^{zzz}
\end{aligned}
\tag{2.4}
$$

$$
\begin{aligned}
a^y &= \frac{1}{2}(A^y_+ + A^y_-);\ a^z = \frac{1}{2}(A^z_+ + A^z_-) \\
a^{yy} &= \frac{1}{2}(A^{yy}_+ + A^{yy}_-);\ a^{zz} = \frac{1}{2}(A^{zz}_+ + A^{zz}_-) \\
b^x &= \frac{1}{2}(B^x_+ + B^x_-);\ b^z = \frac{1}{2}(B^z_+ + B^z_-) \\
b^{xx} &= \frac{1}{2}(B^{xx}_+ + B^{xx}_-);\ b^{zz} = \frac{1}{2}(B^{zz}_+ + B^{zz}_-) \\
c^x &= \frac{1}{2}(C^x_+ + C^x_-);\ c^y = \frac{1}{2}(C^y_+ + C^y_-) \\
c^{xx} &= \frac{1}{2}(C^{xx}_+ + C^{xx}_-);\ c^{yy} = \frac{1}{2}(C^{yy}_+ + C^{yy}_-)
\end{aligned}
\tag{2.5}
$$

$$
\begin{aligned}
a^{xy} &= A^y_+ - A^y_-;\ a^{xz} = A^z_+ - A^z_- \\
a^{xyy} &= A^{yy}_+ - A^{yy}_-;\ a^{xzz} = A^{zz}_+ - A^{zz}_- \\
b^{xy} &= B^x_+ - B^x_-;\ b^{yz} = B^z_+ - B^z_- \\
b^{xxy} &= B^{xx}_+ - B^{xx}_-;\ b^{yzz} = B^{zz}_+ - B^{zz}_- \\
c^{xz} &= C^x_+ - C^x_-;\ c^{yz} = C^y_+ - C^y_- \\
c^{xxz} &= C^{xx}_+ - C^{xx}_-;\ c^{yyz} = C^{yy}_+ - C^{yy}_-
\end{aligned}
\tag{2.6}
$$

As the second constraint, the divergence-free condition of the magnetic field

$$
\frac{\partial B_x(x,y,z)}{\partial x} + \frac{\partial B_y(x,y,z)}{\partial y} + \frac{\partial B_z(x,y,z)}{\partial z} = 0 \tag{2.7}
$$

must be enforced for any points inside the control volume. From Eq. (2.7), we obtain the

following:

$$(a^x + b^y + c^z) + \frac{1}{10}(a^{xxx} + b^{yyy} + c^{zzz}) = 0 \tag{2.8}$$

$$\begin{aligned} a^{xx} = -\frac{1}{2}(b^{xy} + c^{xz});\ b^{yy} = -\frac{1}{2}(a^{xy} + c^{yz});\ c^{zz} = -\frac{1}{2}(a^{xz} + b^{yz}) \\ a^{xxx} = -\frac{1}{3}(b^{xxy} + c^{xxz});\ b^{yyy} = -\frac{1}{3}(a^{xyy} + c^{yyz});\ c^{zzz} = -\frac{1}{3}(a^{xzz} + b^{yzz}) \end{aligned} \tag{2.9}$$

a^{xx}, a^{xxx}, and others are determined by substituting Eq. (2.5) and Eq. (2.6) into Eq. (2.9), and the remaining coefficients, a^0, a^x, and others are derived from Eq. (2.4).

The divergence-free condition is automatically satisfied during the update using the constraint transport method. This condition appears in Eq. (2.8), which is not used to determine the coefficients. From Eq. (2.4), the equation is equivalent to the integral form of the divergence-free condition:

$$(A^0_+ - A^0_-) + (B^0_+ - B^0_-) + (C^0_+ - C^0_-) = 0 \tag{2.10}$$

This condition is the integral version of the divergence-free condition. For the control volume at (i, j, k) with the cell size of $\Delta x \times \Delta y \times \Delta z$, Eq. (2.10) can be rewritten in the dimensional form as follows:

$$\begin{aligned} &\Delta y \Delta z \left(B_{x,i+1/2,j,k} - B_{x,i-1/2,j,k}\right) \\ &+\Delta x \Delta z \left(B_{y,i,j+1/2,k} - B_{y,i,j-1/2,k}\right) \\ &+\Delta x \Delta y \left(B_{z,i,j,k+1/2} - B_{z,i,j,k-1/2}\right) = 0 \end{aligned} \tag{2.11}$$

The original version by Balsara (2009) includes more cross-differential terms. It requires a condition for the minimum magnetic energy in addition to the divergence-free and boundary ones, to determine the coefficients uniquely. As we have shown above, the minimization process is not required in our approach. Balsara (2009) also notes this point.

2.2.2 Reinterpretation of the one-dimensional reconstruction

In this subsection, we propose an efficient method for obtaining the coefficients of the boundary condition in Eq. (2.2). The main idea is the reinterpretation of the arbitrary-order one-dimensional reconstruction as a third-order reconstruction.

In the one-dimensional control volume $x \in [-1/2, 1/2]$ with a volume-averaged value $\langle u \rangle$, one can derive the cell face values $u(x = \pm 1/2)$ from a one-dimensional reconstruction. In the third-order form, the profile $u(x)$ can be written as follows:

$$u(x) = u^0 + u^x P_1(x) + u^{xx} P_2(x) \tag{2.12}$$

The coefficients are given as follows:

$$u^0 = \langle u \rangle;\ u^x = \Delta_x^L u - \Delta_x^R u;\ u^{xx} = 3(\Delta_x^L u + \Delta_x^R u) \tag{2.13}$$

Here we define the reconstruction slopes $\Delta_x^L u = u(x = +1/2) - \langle u \rangle$ and $\Delta_x^R u = u(x = -1/2) - \langle u \rangle$. The coefficients u^0, u^x, and u^{xx} are chosen to reproduce the values for the volume average $\langle u \rangle$ and at the cell surfaces $u(x = \pm 1/2)$. Although Eq. (2.12) is only accurate to third order, the expression in Eq. (2.13) can be applied to various one-dimensional schemes with arbitrary accuracy, maintaining the original value for the volume average $\langle u \rangle$ and the reconstructed value $u(x = \pm 1/2)$.

Following the proposed strategy, the coefficients of the boundary condition in Eq.

(2.2) are rewritten as follows:

$$
\begin{aligned}
A^0_{\pm} &= B_{x,i\pm1/2,j,k} \\
A^y_{\pm} &= \Delta^L_y B_{x,i\pm1/2,j,k} - \Delta^R_y B_{x,i\pm1/2,j,k} \\
A^{yy}_{\pm} &= 3(\Delta^L_y B_{x,i\pm1/2,j,k} + \Delta^R_y B_{x,i\pm1/2,j,k}) \\
A^z_{\pm} &= \Delta^L_z B_{x,i\pm1/2,j,k} - \Delta^R_z B_{x,i\pm1/2,j,k} \\
A^{zz}_{\pm} &= 3(\Delta^L_z B_{x,i\pm1/2,j,k} + \Delta^R_z B_{x,i\pm1/2,j,k}) \\
B^0_{\pm} &= B_{y,i,j\pm1/2,k} \\
B^x_{\pm} &= \Delta^L_x B_{y,i,j\pm1/2,k} - \Delta^R_x B_{y,i,j\pm1/2,k} \\
B^{xx}_{\pm} &= 3(\Delta^L_x B_{y,i,j\pm1/2,k} + \Delta^R_x B_{y,i,j\pm1/2,k}) \\
B^z_{\pm} &= \Delta^L_z B_{y,i,j\pm1/2,k} - \Delta^R_z B_{y,i,j\pm1/2,k} \\
B^{zz}_{\pm} &= 3(\Delta^L_z B_{y,i,j\pm1/2,k} + \Delta^R_z B_{y,i,j\pm1/2,k}) \\
C^0_{\pm} &= B_{z,i,j,k\pm1/2} \\
C^x_{\pm} &= \Delta^L_x B_{z,i,j,k\pm1/2} - \Delta^R_x B_{z,i,j,k\pm1/2} \\
C^{xx}_{\pm} &= 3(\Delta^L_x B_{z,i,j,k\pm1/2} + \Delta^R_x B_{z,i,j,k\pm1/2}) \\
C^y_{\pm} &= \Delta^L_y B_{z,i,j,k\pm1/2} - \Delta^R_y B_{z,i,j,k\pm1/2} \\
C^{yy}_{\pm} &= 3(\Delta^L_y B_{z,i,j,k\pm1/2} + \Delta^R_y B_{z,i,j,k\pm1/2})
\end{aligned}
\tag{2.14}
$$

The third-order divergence-free reconstruction described in the previous subsection can be applied directly. For example, we describe the derivation of the volume-averaged magnetic fields a^0, b^0, and c^0. The first-order cross-differential coefficients in Eq. (2.6)

are given as follows:

$$
\begin{aligned}
a^{xy} &= \left(\Delta_y^L B_{x,i+1/2,j,k} - \Delta_y^R B_{x,i+1/2,j,k}\right) \\
&\quad - \left(\Delta_y^L B_{x,i-1/2,j,k} - \Delta_y^R B_{x,i-1/2,j,k}\right) \\
a^{xz} &= \left(\Delta_z^L B_{x,i+1/2,j,k} - \Delta_z^R B_{x,i+1/2,j,k}\right) \\
&\quad - \left(\Delta_z^L B_{x,i-1/2,j,k} - \Delta_z^R B_{x,i-1/2,j,k}\right) \\
b^{xy} &= \left(\Delta_x^L B_{y,i,j+1/2,k} - \Delta_x^R B_{y,i,j+1/2,k}\right) \\
&\quad - \left(\Delta_x^L B_{y,i,j-1/2,k} - \Delta_x^R B_{y,i,j-1/2,k}\right) \\
b^{yz} &= \left(\Delta_z^L B_{y,i,j+1/2,k} - \Delta_z^R B_{y,i,j+1/2,k}\right) \\
&\quad - \left(\Delta_z^L B_{y,i,j-1/2,k} - \Delta_z^R B_{y,i,j-1/2,k}\right) \\
c^{xz} &= \left(\Delta_x^L B_{z,i,j,k+1/2} - \Delta_x^R B_{z,i,j,k+1/2}\right) \\
&\quad - \left(\Delta_x^L B_{z,i,j,k-1/2} - \Delta_x^R B_{z,i,j,k-1/2}\right) \\
c^{yz} &= \left(\Delta_y^L B_{z,i,j,k+1/2} - \Delta_y^R B_{z,i,j,k+1/2}\right) \\
&\quad - \left(\Delta_y^L B_{z,i,j,k-1/2} - \Delta_y^R B_{z,i,j,k-1/2}\right)
\end{aligned}
\tag{2.15}
$$

The second-order differential coefficients a^{xx}, b^{yy}, and c^{zz} are derived from Eq. (2.9) or in the dimensional form:

$$
a^{xx} = -\frac{\Delta x}{2}\left(\frac{b^{xy}}{\Delta y} + \frac{c^{xz}}{\Delta z}\right);\ b^{yy} = -\frac{\Delta y}{2}\left(\frac{a^{xy}}{\Delta x} + \frac{c^{yz}}{\Delta z}\right);\ c^{zz} = -\frac{\Delta z}{2}\left(\frac{a^{xz}}{\Delta x} + \frac{b^{yz}}{\Delta y}\right) \tag{2.16}
$$

We then obtain the volume-averaged magnetic fields:

$$
\begin{aligned}
\langle B_x \rangle_{i,j,k} &= a^0 = \frac{1}{2}\left(B_{x,i+1/2,j,k} + B_{x,i-1/2,j,k}\right) - \frac{1}{6}a^{xx} \\
\langle B_y \rangle_{i,j,k} &= b^0 = \frac{1}{2}\left(B_{y,i,j+1/2,k} + B_{y,i,j-1/2,k}\right) - \frac{1}{6}b^{yy} \\
\langle B_z \rangle_{i,j,k} &= c^0 = \frac{1}{2}\left(B_{z,i,j,k+1/2} + B_{z,i,j,k-1/2}\right) - \frac{1}{6}c^{zz}
\end{aligned}
\tag{2.17}
$$

Another example is the area-averaged magnetic field at $(i, j+1/2, k)$ reconstructed from

the control volume at (i, j, k), which can be written as follows:

$$\begin{aligned}
B^L_{x,i,j+1/2,k} &= a^0 + a^y P_1(1/2) + a^{yy} P_2(1/2) \\
&= \langle B_x \rangle_{i,j,k} + \frac{1}{2}\left(\Delta^L_y B_{x,i+1/2,j,k} + \Delta^L_y B_{x,i-1/2,j,k}\right) \\
B^L_{y,i,j+1/2,k} &= b^0 + b^y P_1(1/2) + b^{yy} P_2(1/2) + b^{yyy} P_3(1/2) \\
&= \langle B_y \rangle_{i,j,k} + \frac{1}{6} b^{yy} + \frac{1}{2}\left(B_{y,i,j+1/2,k} - B_{y,i,j-1/2,k}\right) = B_{y,i,j+1/2,k} \\
B^L_{z,i,j+1/2,k} &= c^0 + c^y P_1(1/2) + c^{yy} P_2(1/2) \\
&= \langle B_z \rangle_{i,j,k} + \frac{1}{2}\left(\Delta^L_y B_{z,i+1/2,j,k} + \Delta^L_y B_{z,i-1/2,j,k}\right)
\end{aligned} \tag{2.18}$$

Here the superscript L denotes that the variable is reconstructed from the "left"-hand side, i.e., the negative x-direction from $(i, j + 1/2, k)$. Other face-centered variables can be derived similarly. The final example is the edge-averaged magnetic field at $(i+1/2, j-1/2, k)$, reconstructed from the control volume at (i, j, k), given as follows:

$$\begin{aligned}
B^{LU}_{x,i+1/2,j-1/2,k} =& a^0 + a^x P_1(1/2) + a^{xx} P_2(1/2) + a^{xxx} P_3(1/2) + a^y P_1(-1/2) \\
&+ a^{yy} P_2(-1/2) + a^{xy} P_1(1/2) P_1(-1/2) + a^{xyy} P_1(1/2) P_2(-1/2) \\
=& B_{x,i+1/2,j,k} + \Delta^R_y B_{x,i+1/2,j,k} \\
B^{LU}_{y,i+1/2,j-1/2,k} =& b^0 + b^y P_1(-1/2) + b^{yy} P_2(-1/2) + b^{yyy} P_3(-1/2) + b^x P_1(1/2) \\
&+ b^{xx} P_2(1/2) + b^{xy} P_1(1/2) P_1(-1/2) + b^{xxy} P_2(1/2) P_1(-1/2) \\
=& B_{y,i,j-1/2,k} + \Delta^L_x B_{y,i,j-1/2,k} \\
B^{LU}_{z,i+1/2,j-1/2,k} =& c^0 + c^x P_1(1/2) + c^{xx} P_2(1/2) + c^y P_1(-1/2) + c^{yy} P_2(-1/2) \\
=& \langle B_z \rangle_{i,j,k} + \frac{1}{2}\left(\Delta^L_x B_{z,i+1/2,j,k} + \Delta^L_x B_{z,i-1/2,j,k}\right. \\
&\left. + \Delta^R_y B_{z,i+1/2,j,k} + \Delta^R_y B_{z,i-1/2,j,k}\right)
\end{aligned} \tag{2.19}$$

Here the superscript U denotes that the variable is reconstructed from the "upward" direction, i.e., the negative x-direction from $(i, j + 1/2, k)$.

It is worth noting that in practical implementation, many of the coefficients in Eq. (2.3) do not need to be calculated or stored. We choose to store the reconstruction slopes as a form of $\langle u \rangle$ and $\Delta_x^{L/R} u$ defined for Eqs. (2.12) and (2.13). In the case of the x-component of the magnetic field, $B_{x,i\pm1/2,j,k}$ and $\Delta_{y/z}^{L/R} B_{x,i\pm1/2,j,k}$ are stored to obtain the quantities at $(i \pm 1/2, j, k)$, $(i \pm 1/2, j \pm 1/2, k)$, and $(i \pm 1/2, j, k \pm 1/2)$. The volume-averaged magnetic field $\langle B_x \rangle_{i,j,k}$, derived from Eqs. (2.3), (2.15), and (2.17), is also stored. The face-centered variables at $(i, j \pm 1/2, k)$ and $(i, j, k \pm 1/2)$ can be easily derived from the volume-averaged magnetic field $\langle B_x \rangle_{i,j,k}$, along with the reconstruction slopes $\Delta_{y/z}^{L/R} B_{x,i\pm1/2,j,k}$, as shown in Eq. (2.18). Here we complete the description of the modified version of the third-order divergence-free reconstruction of the magnetic field.

We must stress several important points regarding the proposed scheme.

1. One of the advantages of the proposed scheme is the low numerical cost of the reconstruction. We need only two one-dimensional reconstruction calculations per unit cell per single component of the magnetic field for the multidimensional reconstruction. This number does not increase even if we employ higher-order one-dimensional reconstructions.

2. Another advantage of this scheme is that the various types of one-dimensional reconstruction can be used. The original divergence-free reconstruction is designed only for use with centered WENO schemes; however, our scheme can be combined with a wider variety of low-dissipative, higher-order schemes straight forwardly.

3. As reported previously (Balsara, 2004), the second-order term in the volume-averaged magnetic field contributes to preserving the positivity of the gas pressure. This is advantageous for the simulation in low-beta regions.

4. The degree of the numerical dissipation of the magnetic field is mainly determined by the one-dimensional reconstruction on the cell face. This is advantageous in achieving the low-dissipative advection properties of the magnetic field.

5. Our scheme does not employ the minimization of the volume-averaged magnetic energy as in Balsara (2009). Although it makes the derivation simple, the positivity of the gas pressure is less robust than that in the original third-order divergence-free reconstruction with cross-differential terms.

6. The convergence accuracy in the multidimensional problem can be affected by the dropping of the cross-differential terms. Theoretically, it can reduce the convergence rate down to second order in the worst case. However, as we will show in the following section, the proposed scheme achieves a sufficiently high convergence rate, particularly when the main cause of the numerical error comes from the numerical dissipation and not from the dispersion error.

2.3 Constrained transport scheme for ideal magnetohydrodynamics

In this section, we briefly describe a new numerical scheme based on the constrained transport method with the proposed divergence-free reconstruction. The equations of the ideal magnetohydrodynamics are written in the conservative form as follows:

$$\frac{\partial \mathbf{Q}}{\partial t} + \frac{\partial \mathbf{F}}{\partial x} + \frac{\partial \mathbf{G}}{\partial y} + \frac{\partial \mathbf{H}}{\partial z} = 0 \tag{2.20}$$

The conservative variables $\mathbf{Q}$ and the fluxes $\mathbf{F}$, $\mathbf{G}$, and $\mathbf{H}$ are as follows:

$$\mathbf{Q} = \begin{pmatrix} \rho \\ \rho V_x \\ \rho V_y \\ \rho V_z \\ e_{\rm tot} \\ B_x \\ B_y \\ B_z \end{pmatrix} ; \; \mathbf{F} = \begin{pmatrix} \rho V_x \\ \rho V_x^2 + P + B^2/8\pi - B_x^2/4\pi \\ \rho V_y V_x - B_y B_x/4\pi \\ \rho V_z V_x - B_z B_x/4\pi \\ (e_{\rm tot} + P + B^2/8\pi) V_x - (\mathbf{V}\cdot\mathbf{B}) B_x/4\pi \\ 0 \\ -cE_z \\ cE_y \end{pmatrix} \tag{2.21}$$

$$\mathbf{G} = \begin{pmatrix} \rho V_y \\ \rho V_x V_y - B_x B_y/4\pi \\ \rho V_y^2 + P + B^2/8\pi - B_y^2/4\pi \\ \rho V_z V_y - B_z B_y/4\pi \\ (e_{\rm tot} + P + B^2/8\pi) V_y - (\mathbf{V}\cdot\mathbf{B}) B_y/4\pi \\ cE_z \\ 0 \\ -cE_x \end{pmatrix} \tag{2.22}$$

$$\mathbf{H} = \begin{pmatrix} \rho V_z \\ \rho V_x V_z - B_x B_z/4\pi \\ \rho V_y V_z - B_y B_z/4\pi \\ \rho V_z^2 + P + B^2/8\pi - B_z^2/4\pi \\ (e_{\rm tot} + P + B^2/8\pi) V_z - (\mathbf{V}\cdot\mathbf{B}) B_z/4\pi \\ -cE_y \\ cE_x \\ 0 \end{pmatrix} \tag{2.23}$$

where ρ is the mass density, $\mathbf{V}$ is the velocity, $\mathbf{B}$ is the magnetic field, $e_{\rm tot} = P/(\gamma-1) + \rho V^2/2 + B^2/(8\pi)$ is the total energy density, γ is the adiabatic index, c is the speed of light, and

$$\mathbf{E} = \begin{pmatrix} E_x \\ E_y \\ E_z \end{pmatrix} = \frac{1}{c} \begin{pmatrix} -V_y B_z + V_z B_y \\ -V_z B_x + V_x B_z \\ -V_x B_y + V_y B_x \end{pmatrix} \tag{2.24}$$

is the electric field. In accordance with the previous constrained transport schemes (Ryu et al., 1998; Balsara & Spicer, 1999; Gardiner & Stone, 2005), the mass density ρ, the momentum vectors $\rho\mathbf{V}$, and the total energy densities $e_{\rm tot}$ are defined as volume-averaged quantities located at the cell centers, and the magnetic field vectors $\mathbf{B}$ are defined as area-averaged quantities located at the face centers.

2.3.1 One-dimensional reconstruction

One of the advantages of our scheme is that a wider variety of one-dimensional reconstruction methods can be used, such as PPM (Colella & Woodward, 1984), MP5 (Suresh & Huynh, 1997), WENO-JS (Jiang & Shu, 1996) and WENO-Z (Borges et al., 2008). Here two of these are used in the test problems.

The first is the third-order centered WENO scheme by Dumbser & Käser (2007) (WENO-DK3). This was also used in the original study on the divergence-free reconstruction for the third-order scheme (Balsara, 2009). This reconstruction is useful for clarifying the effect of the cross-differential terms accounted for the third-order scheme in Balsara (2009).

The second example is the fifth-order WENO-Z scheme by Borges et al. (2008) (WENO-Z5). This scheme provides lesser dissipation than the classical fifth-order WENO scheme with $r = 3$ (Jiang & Shu, 1996), with the same stencil as the third-order centered WENO scheme. It is employed to check the utility of the proposed scheme in combination with higher-order one-dimensional reconstructions.

2.3.2 Evaluation of the nonlinear term

We need nonlinear algebra for the derivation of the primitive variables from the conservative variables, along with the evaluation of the face-averaged numerical flux and the edge-averaged electric field. In the higher-order finite volume scheme, the proper evaluation of the nonlinear terms involves some delicate issues. One possible method is to evaluate the point-wise values at the proper points of the cell, and to use the fourth-order Simpson's rules or their variants. However, this requires a considerable numerical cost.

Here we evaluate the spatially averaged product/quotient as the product/quotient of the spatially averaged values. Although this is an evaluation to second-order accuracy and could potentially reduce the convergence property of the proposed scheme, we find that this method performs as well as that shown in Section 2.4, considering the numerical cost and the ease of the implementation.

2.3.3 Multidimensional reconstruction

We choose to reconstruct the variables in the primitive form $\mathbf{U} = (\rho, \mathbf{V}, P, \mathbf{B})$. First, the magnetic field vectors $U_{6,7,8} = (\mathbf{B})$ are reconstructed to obtain the volume-averaged magnetic field as shown in Section 2.2. Following this, the hydrodynamic variables $U_{1,\ldots,5} = (\rho, \mathbf{V}, P)$ are reconstructed. These variables $U_{1,\ldots,5}$ are expressed as follows:

$$\begin{aligned} U(x,y,z) = u^0 + u^x P_1(x) + u^{xx} P_2(x) \\ + u^y P_1(y) + u^{yy} P_2(y) + u^z P_1(z) + u^{zz} P_2(z) \end{aligned} \tag{2.25}$$

Here we drop the cross-differential terms. This does not affect the reconstruction of the face-centered variables but reduces the accuracy of the reconstruction of the edge-centered variables, which are used for the evaluation of the electric field. In other words, the face-centered variables are reconstructed in the usual manner with one-dimensional reconstruction schemes. The edge-centered variables are reconstructed with the vector

sum of the reconstruction slope in each direction, as follows:

$$U^{LU}_{i+1/2,j-1/2,k} = U_{i,j,k} + \Delta^L_x U_{i,j,k} + \Delta^R_y U_{i,j,k} \tag{2.26}$$

Here the superscripts L (Left) and U (Up) denote that the variable is reconstructed from the negative x-direction and the positive y-direction, respectively.

2.3.4 Evaluation of the flux and electric field

The face-centered numerical fluxes are evaluated from the face-averaged quantities using the local Lax–Friedrich (LLF) scheme. For example, the x-component of the numerical flux is described as follows:

$$F_{1,\ldots,5,i+1/2,j,k} = \frac{1}{2}\left(F^L_{1,\ldots,5,i+1/2,j,k} + F^R_{1,\ldots,5,i+1/2,j,k}\right) - \frac{a}{2}\left(Q^R_{1,\ldots,5,i+1/2,j,k} - Q^L_{1,\ldots,5,i+1/2,j,k}\right) \tag{2.27}$$

Here a represents the maximum characteristic speed between the two adjoining cells.

The edge-centered electric field is also obtained from the LLF scheme. For example, the electric field E_z at the cell edge is evaluated as follows:

$$\begin{aligned} cE_{z,i+1/2,j+1/2,k} &= -F_{7,i+1/2,j+1/2,k} = G_{6,i+1/2,j+1/2,k} \\ &= \frac{c}{4}(E^{RU}_{z,i+1/2,j+1/2,k} + E^{RD}_{z,i+1/2,j+1/2,k} + E^{LU}_{z,i+1/2,j+1/2,k} + E^{LD}_{z,i+1/2,j+1/2,k}) \\ &+ \frac{a}{4}(B^{RU}_{y,i+1/2,j+1/2,k} + B^{RD}_{y,i+1/2,j+1/2,k} - B^{LU}_{y,i+1/2,j+1/2,k} - B^{LD}_{y,i+1/2,j+1/2,k}) \\ &- \frac{a}{4}(B^{RU}_{x,i+1/2,j+1/2,k} - B^{RD}_{x,i+1/2,j+1/2,k} + B^{LU}_{x,i+1/2,j+1/2,k} - B^{LD}_{x,i+1/2,j+1/2,k}) \end{aligned} \tag{2.28}$$

Here the superscripts R (L) and U (D) denote that the variable is reconstructed from the positive (negative) x-direction and the positive (negative) y-direction, respectively, and a represents the maximum characteristic speed among the four adjoining cells. We note

the equality of $B_y^{RU} = B_y^{RD}$, $B_y^{LU} = B_y^{LD}$, $B_x^{RU} = B_x^{LU}$, and $B_x^{RD} = B_x^{LD}$, due to the boundary conditions of the divergence-free reconstruction. The proper upwinding of the electric field has been a topic of discussion. Our approach follows the studies (Ryu et al., 1998; Londrillo & del Zanna, 2004), where the dissipation terms were doubled compared with the simple flux-averaging scheme given by (Balsara & Spicer, 1999). This reduces to the properly upwinded one-dimensional scheme when the domain approaches one dimension. Another option is to use a multidimensional version of the Riemann solvers (Balsara, 2010).

2.3.5 Time advancement

We employ the third-order SSP Runge–Kutta method (Jiang & Shu, 1996; Gottlieb et al., 2001, 2009) for time advancement. When demonstrating the accuracy analysis of the fifth-order WENO-Z5 scheme in Section 2.4, we multiply the Courant number by a certain factor when the number of meshes increases so that the relation $(\Delta t)^3 \propto (\Delta x)^5$ is satisfied. A constant Courant number is used in the accuracy analysis of the WENO-DK3 scheme.

2.4 Accuracy analysis

In this section, we provide the results of the accuracy analysis in the multidimensional problems of magnetohydrodynamics to show that the new divergence-free reconstruction scheme shows high-order convergence for the problems that require accurate evolution of the magnetic field. The Courant number is set to 0.4 for all runs with the WENO-DK3 scheme and for the lowest resolution runs with the WENO-Z5 scheme. As mentioned previously, we reduce the Courant number to achieve $(\Delta t)^3 \propto (\Delta x)^5$ for the spatial fifth-order WENO-Z5 scheme so that we can focus on the errors arising from the spatial discretization.

Table 2.1: The accuracy analysis for the magnetized isodensity vortex problem in two-dimensions. The errors are measured in the x-component of the magnetic field.

Method	Number of mesh	L_1 error	L_1 order	L_∞ error	L_∞ order
WENO-DK3	32×32	1.23391×10^{-2}		2.01523×10^{-1}	
	64×64	2.76382×10^{-3}	2.16	4.79692×10^{-2}	2.07
	128×128	3.79622×10^{-4}	2.86	7.01097×10^{-3}	2.77
	256×256	4.80638×10^{-5}	2.98	9.04273×10^{-4}	2.95
WENO-Z5	32×32	6.28667×10^{-3}		3.09841×10^{-1}	
	64×64	8.57310×10^{-4}	2.87	5.82211×10^{-2}	2.41
	128×128	4.47140×10^{-5}	4.26	2.95134×10^{-3}	4.30
	256×256	2.89276×10^{-6}	3.95	2.32102×10^{-4}	3.67

2.4.1 The magnetized isodensity vortex in two dimensions

This test problem is described in Balsara (2004), and is used for a convergence check of the divergence-free reconstruction to second order (Balsara, 2004) and higher (Balsara, 2009). The magnetized vortex in the dynamical balance is advected in an oblique direction to the two-dimensional mesh. This is a genuine two-dimensional problem, and it complements the masked errors of the one-dimensional problems with an oblique direction, as presented in the next subsection.

The numerical domain is given by $[-5, 5] \times [-5, 5]$ and integrated over a time of 10 units for the WENO-DK3 scheme. For the WENO-Z5 scheme, the domain is increased to $[-10, 10] \times [-10, 10]$, and the integration time is increased to 20 units. This comes from the loss of accuracy near the boundary because of the inconsistency of the initial and boundary conditions, which becomes significant in the higher-order scheme (Balsara, 2009). Periodic boundary conditions are assumed. The unperturbed state is initialized as $(\rho, V_x, V_y, V_z, P, B_x, B_y, B_z) = (1, 1, 1, 0, 1, 0, 0, 0)$. The adiabatic index γ is set to $5/3$. The vortex is produced as a perturbation on the velocity

$$(\delta V_x, \delta V_x) = V_0 \mathrm{e}^{(1-r^2)/2}(-y, x), \tag{2.29}$$

and on the magnetic field initialized by the vector potential

$$\delta A_z = B_0 \mathrm{e}^{(1-r^2)/2}, \tag{2.30}$$

where $r = \sqrt{x^2 + y^2}$. We choose the parameter of $(V_0, B_0) = (1/(2\pi), 1/\sqrt{\pi})$. The total force balance is achieved by creating a perturbation in the gas pressure

$$\delta P = \frac{1}{8\pi} B_0^2 (1 - r^2) \mathrm{e}^{1-r^2} - \frac{1}{2} \rho V_0^2 \mathrm{e}^{1-r^2}, \tag{2.31}$$

No perturbation is required for (ρ, V_z, B_z).

Table 2.1 shows the convergence rate in this problem. The error is measured for the x-component of the magnetic field. The L_1/L_∞ error is defined as the average/maximum of the absolute value of the difference between the initial and final state over the whole domain. Both schemes achieve the desired level of accuracy. The results obtained with the WENO-DK3 scheme are directly compared with those of the third-order WENO-RK scheme in Table 1 in Balsara (2009). The errors of our WENO-DK3 scheme are several times larger than those of the third-order scheme by Balsara (2009) for all mesh numbers. This is because he employs the linearized Riemann solver, the high-order evaluation of nonlinear terms, and cross-differential terms in the reconstruction. However, our WENO-DK3 scheme produces an order of accuracy similar to that produced by the scheme proposed in Balsara (2009). The result of the WENO-Z5 scheme shows much less numerical diffusion than the WENO-DK3 scheme and a high convergence rate, although it does not reach the spatial accuracy of the one-dimensional fifth-order WENO-Z reconstruction. The abovementioned results prove that our modification on the divergence-free reconstruction performs well for this problem.

Table 2.2: The accuracy analysis for the circularly polarized Alfvén wave problem in two-dimensions of $\theta = \pi/3$ case. The errors are measured in the x-component of the magnetic field.

Method	Number of mesh	L_1 error	L_1 order	L_∞ error	L_∞ order
WENO-DK3	8×8	3.49481×10^{-2}		5.80017×10^{-2}	
	16×16	2.22055×10^{-2}	0.65	3.52868×10^{-2}	0.72
	32×32	4.02669×10^{-3}	2.46	6.33940×10^{-3}	2.48
	64×64	5.29214×10^{-4}	2.93	8.31611×10^{-4}	2.93
WENO-Z5	8×8	2.25209×10^{-2}		3.69293×10^{-2}	
	16×16	1.18054×10^{-3}	4.25	1.84657×10^{-3}	4.32
	32×32	3.54686×10^{-5}	5.06	5.73430×10^{-5}	5.01
	64×64	1.11858×10^{-6}	5.01	1.77847×10^{-6}	4.99

2.4.2 The circularly polarized Alfvén wave in two dimensions

The obliquely propagating, one-dimensional, circularly polarized Alfvén wave can be used to check the convergence rate in a multidimensional domain (Tóth, 2000). Here we employ a two-dimensional version of the problem with the parameters used in Balsara (2009), which are chosen to reduce the effects of parametric instability on the circularly polarized Alfvén wave.

The circularly polarized Alfvén wave propagates at an angle of $\alpha = \pi/3$ relative to the x-axis. The domain size is $[0, 1/\cos\alpha] \times [0, 1/\sin\alpha]$, and the wave length is set to unity. Each variables are initialized as follows:

$$
\begin{aligned}
&\rho = \rho_0,\ P = P_0, \\
&V_x = V_\parallel \cos\alpha + V_\perp \sin\alpha \cos(2\pi x_\parallel),\ B_x = B_\parallel \cos\alpha - B_\perp \sin\alpha \cos(2\pi x_\parallel), \\
&V_y = V_\parallel \sin\alpha - V_\perp \cos\alpha \cos(2\pi x_\parallel),\ B_y = B_\parallel \sin\alpha + B_\perp \cos\alpha \cos(2\pi x_\parallel), \\
&V_z = -V_\perp \sin(2\pi x_\parallel),\ B_z = B_\perp \sin(2\pi x_\parallel),
\end{aligned}
\tag{2.32}
$$

where $x_\parallel = x\cos\alpha + y\sin\alpha$ is the coordinate along the propagation direction. The x and y-components of the magnetic field are initialized by the vector potential

$$
A_z = B_\parallel y\cos\alpha - B_\parallel x\sin\alpha - B_\perp \sin(2\pi x_\parallel)/(2\pi). \tag{2.33}
$$

We use the parameters $\rho_0 = 1$, $P_0 = 1000$, $V_\parallel = 1$, $V_\perp = B_\perp/\sqrt{4\pi\rho_0} = 0.02$, and $B_\parallel = \sqrt{4\pi\rho_0}$. The resulting wave propagation speed is 2 units, and the calculation is stopped at a time of $1/2$.

Table 2.2 shows the results of this accuracy analysis. The error is measured for the x-component of the magnetic field. The low convergence rate appears between 8×8 and 16×16 meshes in the WENO-DK3 scheme. This is because the wave is damped to almost zero by the strong numerical dissipation in both cases. The WENO-DK3 scheme recovers the high convergence rate with a larger number of meshes. The WENO-Z5 scheme performs very well and produces the desired accuracy. The results seem to not be affected by the parametric instability as reported previously (Balsara et al., 2009). The abovementioned results show that our new method provides sufficient convergence properties for this problem. It is notable that the WENO-DK3 scheme and the WENO-Z5 scheme have the same stencil and essentially the same numerical cost. This demonstrates the high cost effectiveness of the WENO-Z5 scheme.

2.5 Test problems

In this section, we present the results of several standard test problems of magnetohydrodynamics. The Courant number is set to 0.4 for all test problems.

2.5.1 The field loop advection in two-dimensions

The field loop advection problem (Gardiner & Stone, 2005) is set up on a domain of $[-0.5, 0.5] \times [-0.5, 0.5]$. A weak magnetic loop is advected in the high plasma beta region. This problem is used to assess the multidimensional properties of the numerical dissipation by the scheme.

Fig.2.1 shows the results obtained with the WENO-DK3 scheme (panel (a)) and the WENO-Z5 scheme (panel (b)). The results show no oscillations within the loop and lesser directional bias than the second-order upwind schemes with less dissipative Rie-

mann solvers (Gardiner & Stone, 2005; Lee & Deane, 2009). The directional bias in both schemes seems to be larger than that in the recent scheme (Balsara et al., 2013) that employs the centered WENO scheme with many more cross-differential terms than our reconstructions. We also note that the reconstruction in Balsara et al. (2013) does not employ the divergence-free reconstruction. It is noted that the directional bias due to the LLF scheme is smaller than that due to the HLL(E), HLLC, HLLD or linearized Riemann solvers with less dissipation. The reconstruction of the velocity field does not affect the results in this problem. We also note that even if the cross-differential terms are appropriately accounted for in the reconstruction step, the directional bias in this level cannot be avoided. This is because any cross-differential term of the magnetic field reconstruction does not contribute to the evaluation of the edge-averaged electric field when the velocity field is uniform. These results indicate that the proposed scheme sufficiently reproduces the multidimensional advection of the magnetic field.

2.5.2 The rotor problem in two-dimensions

The rotor problem (Balsara & Spicer, 1999; Tóth, 2000) is set up on a domain of $[-0.5, 0.5] \times [-0.5, 0.5]$. We demonstrate a version of this problem as described in (Balsara, 2004). Fig.2.2 shows the results calculated by the WENO-Z5 scheme on a 200×200 mesh. The results are consistent with those of the previous study (Balsara & Spicer, 1999). This shows that our new usage of the divergence-free reconstruction works well on this genuinely multidimensional problem with a discontinuity.

2.5.3 The blast problem in two-dimensions

The blast problem (Balsara & Spicer, 1999) is commonly used to check the robustness of a numerical scheme for shock propagation in the low plasma beta region. Fig.2.3 is a version of the problem proposed by Gardiner & Stone (2005), obtained using the WENO-Z5 scheme on a 200×200 mesh. The plasma beta in the ambient medium is $\beta = 2 \times 10^{-2}$.

The results are consistent with those of the previous study (Gardiner & Stone, 2005). The abovementioned results indicate that the proposed scheme also works well for this strong shock propagation problem in the low plasma beta region.

2.6 Conclusions

We have presented a method to construct a higher-order scheme on the basis of the divergence-free magnetic field reconstruction. The new magnetohydrodynamics scheme based on the proposed method using the third-order centered WENO and the fifth-order WENO-Z reconstructions have been presented and tested. The proposed method can be applied to a wide variety of one-dimensional reconstructions such as PPM, classical fifth-order WENO, and MP5. The proposed divergence-free reconstruction is invariant for the choice of the one-dimensional reconstruction, and it performs with high cost-effectiveness when it is combined with a less-dissipative WENO-Z scheme.

Our numerical methods include some important approximations that could potentially reduce the convergence accuracy to second order in the worst case. Firstly, in the evaluation of the velocity field at the cell edges, we employed Eq. (2.25), where we dropped some cross terms. This reduces the multidimensional accuracy of the reconstruction. The second approximation we made was the evaluation of the nonlinear terms from the spatially averaged quantities in Section 2.3.2. This is also a potential source of accuracy loss. Despite the points mentioned above, the accuracy analysis proposed in Section 2.4 proves sufficient convergence. In conclusion, all the tests presented here suggest that the proposed scheme is highly cost effective and sufficiently robust for practical use.

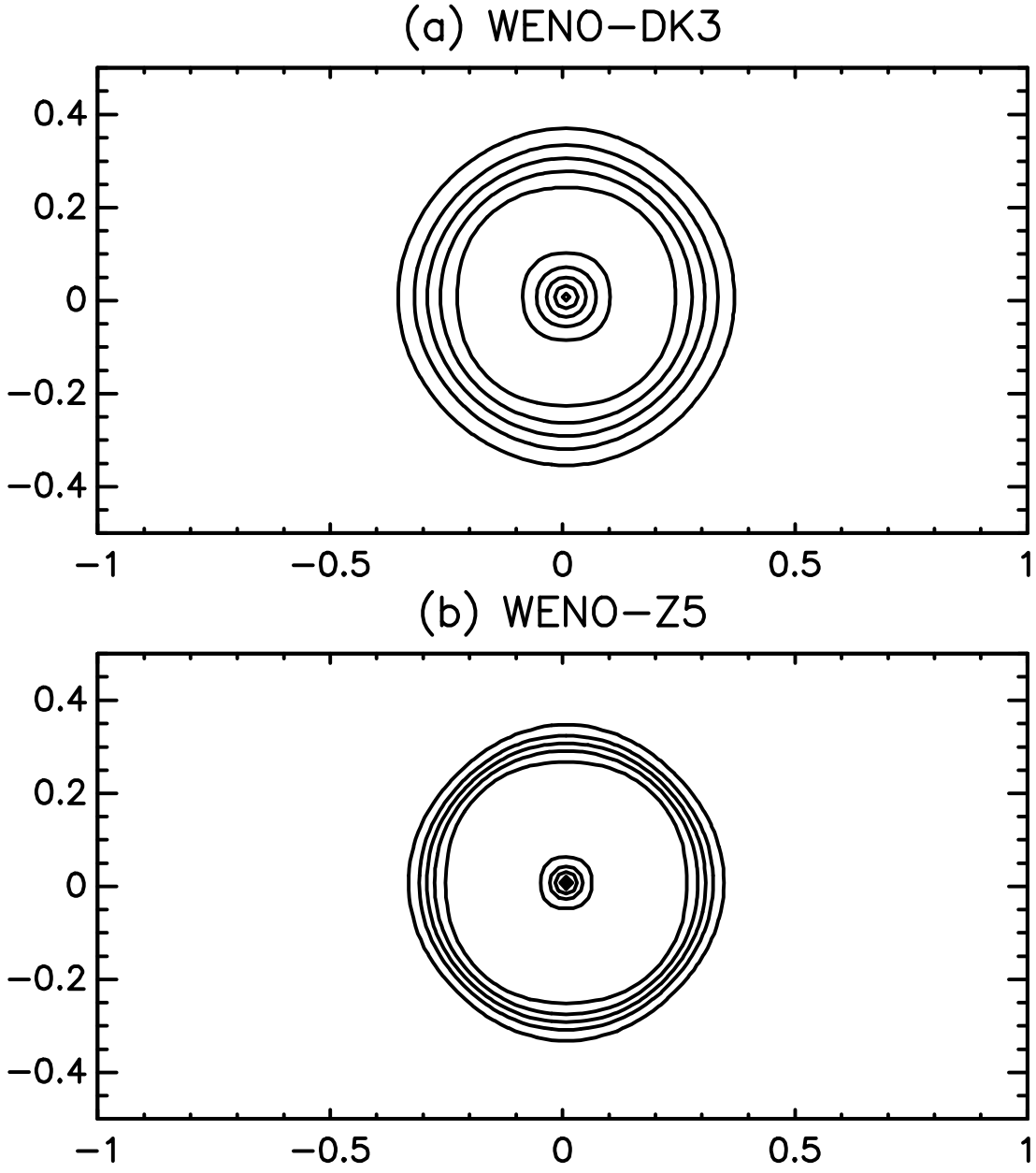

Figure 2.1: The magnitude of the magnetic field for the field loop advection problem. The results obtained with (a) the WENO-DK3 scheme and (b) the WENO-Z5 scheme on a 128×64 mesh are shown. Five equally spaced contour lines are plotted between the minimum and the maximum values.

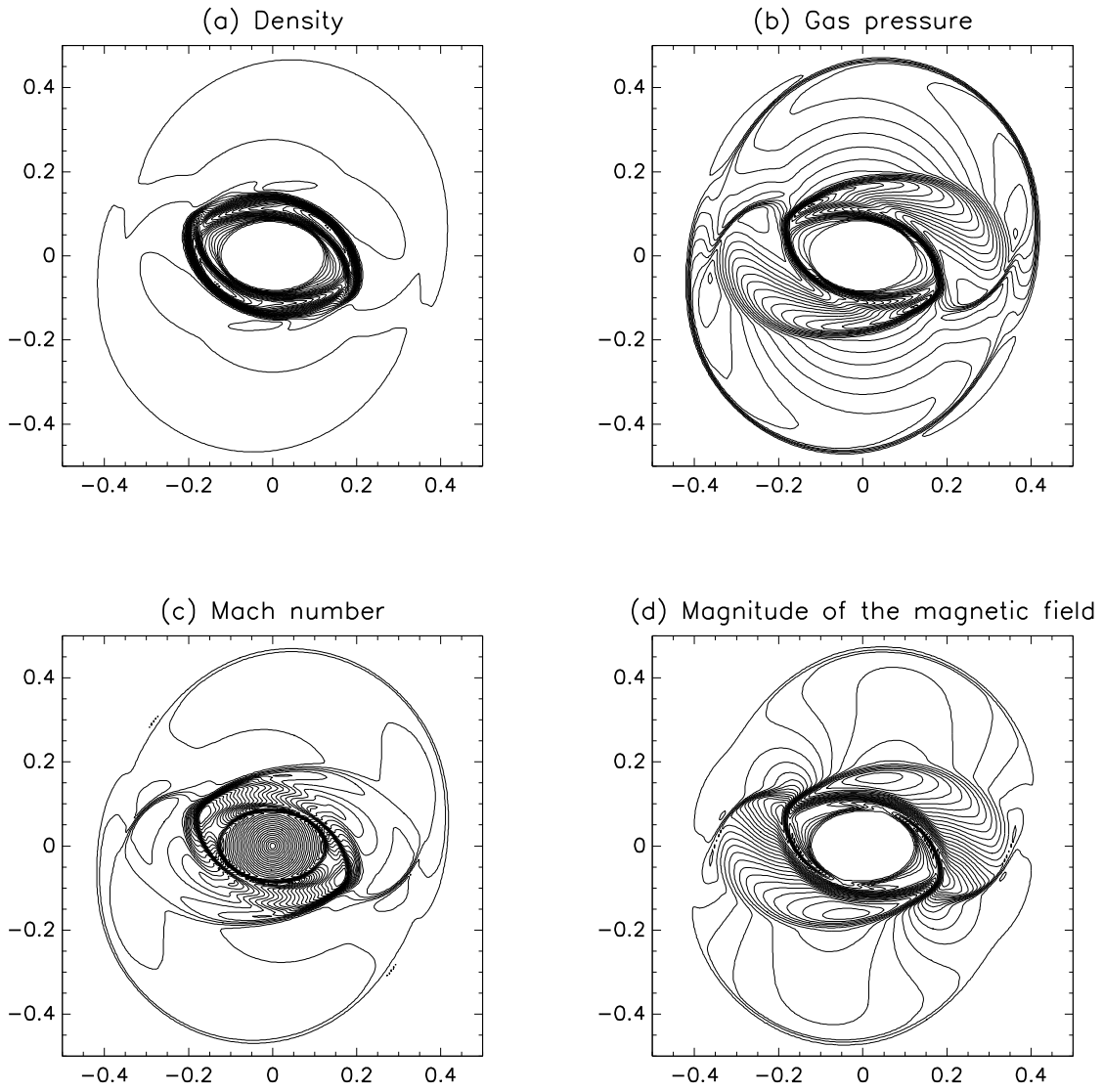

Figure 2.2: (a) Density, (b) gas pressure, (c) Mach number, and (d) the magnitude of the magnetic field for the rotor problem. Thirty equally spaced contours are shown for the ranges $0 \leq \rho \leq 10.41$, $0 \leq P \leq 0.739$, $0 \leq V/C_s \leq 2.354$, and $0 \leq B \leq 4.183$. The results are obtained with the WENO-Z5 scheme on a 200×200 mesh.

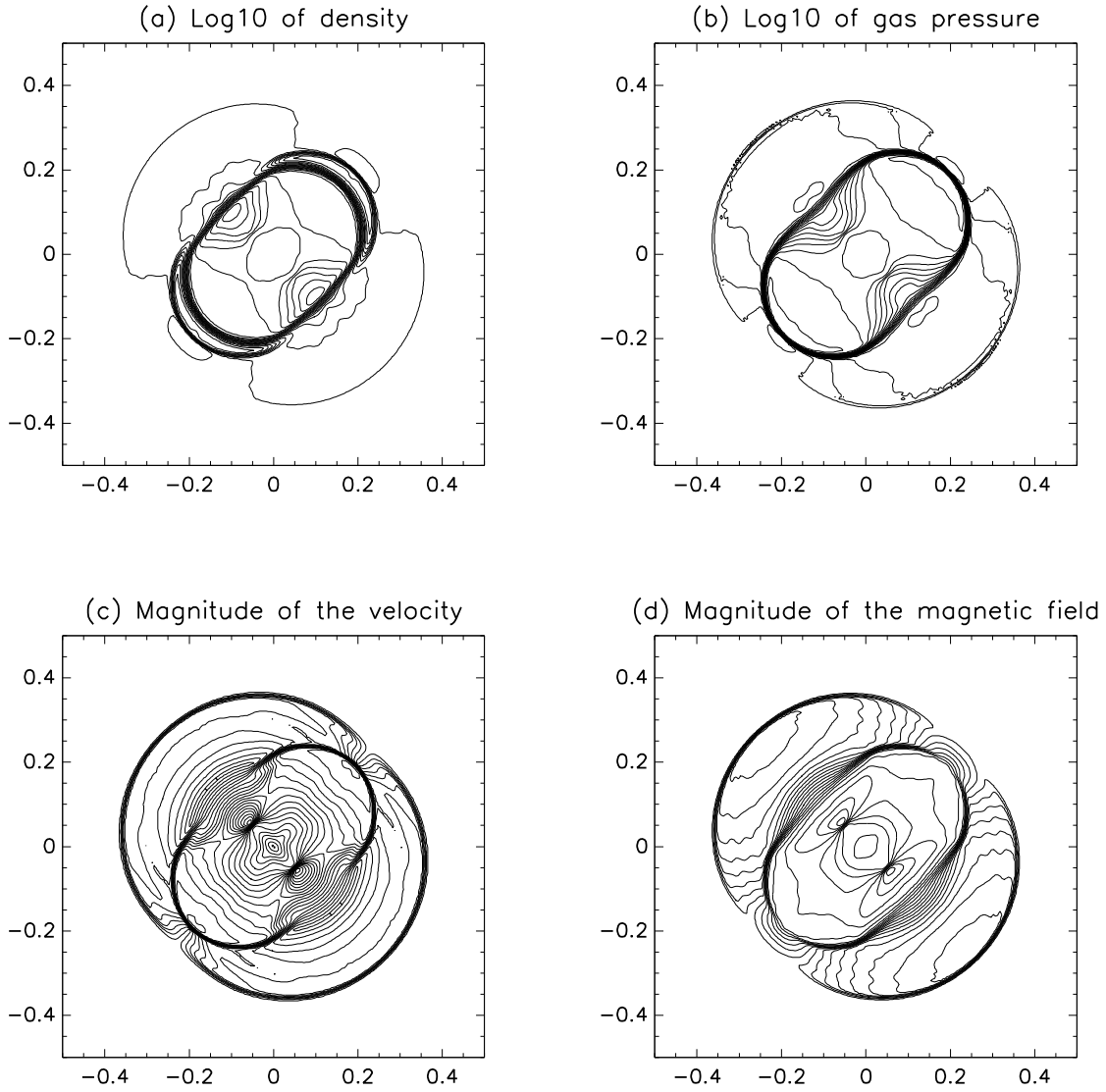

Figure 2.3: (a) The logarithm of the density, (b) the logarithm of the gas pressure, (c) the magnitude of the velocity, and (d) the magnitude of the magnetic field for the blast problem. Twenty equally spaced contours are shown for the ranges between the minimum and the maximum of $-0.716 < \log_{10}\rho < 0.510$, $0.0845 < \log_{10} P < 1.50$, $0.00 < V < 6.28$, and $24.0 < B < 43.7$, respectively. These results are obtained with the WENO-Z5 scheme on a 200×200 mesh.

Chapter 3

Development of radiation magnetohydrodynamic code

3.1 Introduction

The numerical study of the photospheric convection by Nordlund (1982) is one of the most sophisticated modeling in the solar and stellar physics. They found that the granulation in the solar photosphere can be reproduced in excellent accuracy by the hydrodynamic simulation from the upper convection zone to the lower chromosphere with the effect of latent heat by the partial ionization and the energy transfer by the radiation (Stein & Nordlund, 1998). This realistic radiative hydrodynamic model of the solar surface convection has been applied, for example, on excitation process of solar acoustic oscillation (Nordlund & Stein, 2001; Stein & Nordlund, 2001), abundance determination of solar photosphere (Asplund et al., 2009), magneto-convection (Vögler et al., 2005), sunspot (Rempel et al., 2009), and flux emergence (Cheung et al., 2008; Stein et al., 2011).

Bifrost code (Gudiksen et al., 2011) extended the upper boundary of the simulation box to the lower corona for the realistic modeling of the upper solar atmosphere, especially the chromosphere and the lower corona. The code includes the Spitzer-type thermal conduction, approximated chromospheric radiative cooling, and non-equilibrium hydro-

gen ionization in addition to the physical processes in the code by Nordlund (1982). This was the only radiative magnetohydrodynamic (MHD) code for the modeling of the chromosphere and corona, which employed the realistic photospheric convection following the approach of Nordlund (1982). We note that Abbett (2007) and Isobe et al. (2008) also produced the dynamical models of the chromosphere and corona using the simplified radiative cooling without the non-local radiative transfer. Although successful, the Bifrost code still has shortcomings, such as non-guaranteed total energy conservation due to the employment of non-conservative form for the energy equation and the possible wrong convergence on the non-equilibrium calculation (Golding, 2010). Since its uniqueness, no one has been able to independently confirm the results by the Bifrost code so far. It is necessary to develop a independent numerical code with such various physical processes. Because the chromosphere is one of the most interesting targets for the solar physics, the discussion on the plans for the new instrument and satellite are very active. This kind of realistic modeling of solar atmosphere is demanded.

In this study, we develop a new radiative MHD code for the dynamical modeling of solar atmosphere. The code employs the high-resolution conservative MHD code developed in the previous chapter. The numerical algorithm is chosen for the efficiency and compatibility with the massively parallel computation.

3.2 Basic equations

The basic equations solved by our code are the MHD equations with the gravity, local thermodynamic equilibrium (LTE) equation of states, radiative cooling, and thermal conduction along magnetic field lines.

3.2.1 Magnetohydrodynamics

The MHD equations employed in this study are given as follows:

$$\frac{\partial \rho}{\partial t} + \nabla \cdot (\rho \boldsymbol{V}) = 0 \tag{3.1}$$

$$\frac{\partial (\rho \boldsymbol{V})}{\partial t} + \nabla \cdot \left[\rho \boldsymbol{V} \otimes \boldsymbol{V} + \left(P + \frac{B^2}{8\pi} \right) \underline{\mathrm{I}} - \frac{\boldsymbol{B} \otimes \boldsymbol{B}}{4\pi} \right] = \rho \boldsymbol{g} \tag{3.2}$$

$$\begin{aligned} &\frac{\partial e}{\partial t} + \nabla \cdot \left[\left(e + P + \frac{B^2}{8\pi} \right) \boldsymbol{V} - \frac{1}{4\pi} \boldsymbol{B} (\boldsymbol{V} \cdot \boldsymbol{B}) \right] \\ &\quad = \rho (\boldsymbol{g} \cdot \boldsymbol{V}) + Q_{\mathrm{cnd}} + Q_{\mathrm{rad}} + Q_{\mathrm{art}} \end{aligned} \tag{3.3}$$

$$\frac{\partial \boldsymbol{B}}{\partial t} + \nabla \cdot (\boldsymbol{V} \otimes \boldsymbol{B} - \boldsymbol{B} \otimes \boldsymbol{V}) = 0 \tag{3.4}$$

Here, ρ is mass density, $e = e_{\mathrm{int}} + \rho V^2/2 + B^2/(8\pi)$ is total energy density, e_{int} is internal energy density, $\boldsymbol{V}$ is velocity field, $\boldsymbol{B}$ is magnetic flux density, P is gas pressure, and $\boldsymbol{g}$ is gravitational acceleration.

An artificial heating term Q_{art} is included to prevent very low temperatures around the photosphere and the low chromosphere, which is given by

$$Q_{\mathrm{art}} = \frac{3}{2} \left(\frac{P}{T} \right) \max \left(0, \frac{T_{\mathrm{lb}} - T}{\tau_{\mathrm{art}}} \right), \tag{3.5}$$

where $T_{\mathrm{lb}} = 2000$ K and $\tau_{\mathrm{art}} = 1$ s. This artificial heating term is switched on only when the temperature becomes lower than 2000 K and heats the plasma over a timescale of 1 s.

3.2.2 Equation of states

The latent heat production associated with the change of the internal states of atoms and molecules is important in the partial ionized atmosphere near the solar surface. This effect on the equation of states is not negligible from the upper convection zone to the transition

Z	Element	Number fraction $A_{\rm s}$	Mass fraction
1	H	9.21054E-01	7.39300E-01
2	He	7.79620E-02	2.48500E-01
6	C	2.43185E-04	2.32598E-03
7	N	6.10854E-05	6.81356E-04
8	O	5.19921E-04	6.62433E-03
10	Ne	1.59821E-04	2.56832E-03

Table 3.1: Elemental abundance used for the equation of states.

region. In this study, six most abundant elements (H, He, C, N, O, Ne) are considered. We assume the local thermodynamic equilibrium (LTE).

Table 3.1 shows the elemental abundance used in this study. The mass fraction between hydrogen, helium, and other metals are taken from Asplund et al. (2006). The relative abundance among C, N, O, and Ne is same as in Rogers et al. (1996).

The mass density ρ is defined by

$$\rho = \sum_{\rm s} m_{\rm s} n_{\rm s} = m_{\rm a} n_{\rm a}, \tag{3.6}$$

$$m_{\rm a} = \frac{\sum_{\rm s} m_{\rm s} n_{\rm s}}{n_{\rm a}} = \sum_{\rm s} m_{\rm s} A_{\rm s}, \tag{3.7}$$

where $n_{\rm s}$, $m_{\rm s}$, and $A_{\rm s}$ are the number density of atomic nuclei, mass per particle, and abundance for the element s, respectively. $m_{\rm a}$ is the average mass per particle for the neutral gas. $n_{\rm a}$ is the total number density of atomic nuclei.

We consider the four states for the hydrogen; ground and first excited state for neutral atom, ionized atom, and hydrogen molecule. The number density for each states satisfies

$$\sum_{i=1}^{2} n_{{\rm H\,I},\,i} + n_{\rm H\,II} + 2n_{\rm H_2} = n_{\rm H} = A_{\rm H} n_{\rm a}, \tag{3.8}$$

where $n_{{\rm H\,I},\,i}$ is the number density of neutral hydrogen in the i-th energy level, $n_{\rm H\,II}$ is the number density of ionized hydrogen, $n_{\rm H_2}$ is the number density of molecular hydrogen.

The neutral and ionized hydrogen are related by the Saha-Boltzmann equation given

by

$$\frac{n_{\mathrm{H\,I},\,i}}{n_e n_{\mathrm{H\,II}}} = \left(\frac{h^2}{2\pi m_e k_{\mathrm{B}} T}\right)^{2/3} \frac{g_{\mathrm{H\,I},\,i}}{g_e g_{\mathrm{H\,II}}} \exp\left(\frac{\epsilon_{\mathrm{H\,II}} - \epsilon_{\mathrm{H\,I},\,i}}{k_{\mathrm{B}} T}\right), \tag{3.9}$$

where m_e is the electron mass per particle, h is the Planck constant, k_{B} is the Boltzmann constant, $g_e = 2$ is the statistical weight of electron, $g_{\mathrm{H\,I},\,i} = 2i^2$ is the Gaunt factor of neutral hydrogen in the i-th level, $g_{\mathrm{H\,II}} = 1$ is the Gaunt factor of ionized hydrogen, $\epsilon_{\mathrm{H\,I},\,i}$ is the energy level of neutral hydrogen in the i-th level, and $\epsilon_{\mathrm{H\,II}}$ is the energy level of ionized hydrogen.

The molecular hydrogen are treated under the assumption of chemical equilibrium. The equation is given by

$$n_{\mathrm{H_2}} = \left(\sum_{i=1}^{2} n_{\mathrm{H\,I},\,i}\right)^2 K(T), \tag{3.10}$$

where $K(T)$ is the chemical equilibrium constant taken from Kurucz (1970).

The other elements (He, C, N, O, Ne) are modeled by Saha's ionization equilibrium. We consider three states for each element: bound, first ionized, and second ionized states. The number density of the element s satisfies

$$\sum_{j=0}^{2} n_{\mathrm{s},\,j} = n_{\mathrm{s}} = A_{\mathrm{s}} n_{\mathrm{a}}. \tag{3.11}$$

The equation of Saha's ionization equilibrium for the element s is given by

$$\frac{n_{\mathrm{s},\,j}}{n_e n_{\mathrm{s},\,j+1}} = \frac{U_{\mathrm{s},\,j}(T)}{g_e U_{\mathrm{s},\,j+1}(T)} \exp\left(\frac{\epsilon_{\mathrm{s},\,j+1} - \epsilon_{\mathrm{s},\,j}}{k_{\mathrm{B}} T}\right), \tag{3.12}$$

where $n_{\mathrm{s},\,j}$, $U_{\mathrm{s},\,j}(T)$, and $\epsilon_{\mathrm{s},\,j}$ are the number density, partition function, and energy level for the ionization degree of $j = 0, 1, 2$, respectively. The partition function is taken from Irwin (1981).

The charge conservation law between the electron and ions is given by

$$n_{\mathrm{H\,II}} + \sum_{s,j} j n_{\mathrm{s},\,j} = n_e. \tag{3.13}$$

The total (neutral plus ionized) gas pressure and internal energy are defined as

$$P = \left(\sum_{i=1}^{2} n_{\mathrm{H\,I},\,i} + n_{\mathrm{H\,II}} + n_{\mathrm{H_2}} + \sum_{j=0}^{2} n_{\mathrm{s},\,j} + n_e \right) k_{\mathrm{B}} T, \tag{3.14}$$

$$e_{\mathrm{int}} = \frac{3}{2} P + \sum_{i=1}^{2} \epsilon_{\mathrm{H\,I},\,i} n_{\mathrm{H\,I},\,i} + \epsilon_{\mathrm{H\,II}} n_{\mathrm{H\,II}} + \epsilon_{\mathrm{H_2}}(T) n_{\mathrm{H_2}} + \sum_{j=0}^{2} \epsilon_{\mathrm{s},\,j} n_{\mathrm{s},\,j}, \tag{3.15}$$

where $\epsilon_{\mathrm{H_2}}(T)$ is the internal energy of molecular hydrogen calculated from the polynomial approximation in Vardya (1965). The first term and others in Eq. (3.15) represent the contribution from the energy of translational motion and internal (latent) energy, respectively.

3.2.3 Radiation

We model the radiative heating rate Q_{rad} by the combination of two approximations, i.e., the optically thick Q_{thick} and thin Q_{thin}, expressed as

$$Q_{\mathrm{rad}} = \xi(m_c) Q_{\mathrm{thick}} + \left[1 - \xi(m_c)\right] Q_{\mathrm{thin}}, \tag{3.16}$$

$$\xi(m_c) = \max\left[0, \min\left(1, \frac{\log m_1/m_c}{\log m_1/m_0}\right)\right], \tag{3.17}$$

where the column mass density m_c is defined as

$$m_c(x, y, z, t) = \int_{z}^{z_{\mathrm{top}}} \rho(x, y, z', t) dz'. \tag{3.18}$$

We take $\log(m_0\ [\mathrm{g/cm^2}]) = -1.5$ and $\log(m_1\ [\mathrm{g/cm^2}]) = -2$. z_{top} is the height of the top boundary of the numerical domain, typically in the corona. This is the value near the temperature minimum region.

Optically thick radiation

The optically thick radiative heating rate $Q_{\rm thick}$ is calculated by directly solving the frequency averaged radiative transfer equation

$$\boldsymbol{n} \cdot \nabla I = \alpha_{\rm R}(S - I). \tag{3.19}$$

Here, I is the frequency averaged radiative intensity, S is the source function, $\boldsymbol{n}$ is the unit vector of the ray direction, $\alpha_{\rm R} = \rho\kappa_{\rm R}$ is the absorption coefficient, and $\kappa_{\rm R}$ is the Rosseland mean opacity. We employ the OPAL opacity (Iglesias & Rogers, 1996) for $\kappa_{\rm R}(\rho, T)$. We suppress the effect from the transition region and corona, where the gray approximation is not appropriate, by reducing the $\alpha_{\rm R}$ where $\log(m_c\,[{\rm g/cm^2}]) < -2.1$ and setting $\alpha_{\rm R} = 0$ where $\log(m_c\,[{\rm g/cm^2}]) < -2.3$.

The optically thick radiative heating rate $Q_{\rm thick}$ is expressed using the two different (but physically equivalent) forms of

$$Q_{\rm F} = -\nabla \cdot \boldsymbol{F}, \quad \boldsymbol{F} = \int_{4\pi} \boldsymbol{n} I(\boldsymbol{n}) d\boldsymbol{n} \tag{3.20}$$

and

$$Q_{\rm J} = 4\pi\alpha_{\rm R}\left(J - S\right), \quad J = \frac{1}{4\pi}\int_{4\pi} I(\boldsymbol{n}) d\boldsymbol{n}. \tag{3.21}$$

Bruls et al. (1999) pointed out that $Q_{\rm F}$ ($Q_{\rm J}$) is suffered from the numerical errors in the optically thin (thick) region. Following the approach in Bruls et al. (1999), Vögler et al. (2005), and Hayek et al. (2010), we combine the two expressions as:

$$Q_{\rm thick} = {\rm e}^{-(\tau/\tau_0)^2} Q_{\rm J} + \left[1 - {\rm e}^{-(\tau/\tau_0)^2}\right] Q_{\rm F}. \tag{3.22}$$

Here, we set $\tau_0 = 0.1$.

Optically thin radiation

In the chromosphere and corona, we employ the so-called coronal approximation for the radiative cooling rate

$$Q_{\rm thin} = -n_e n_H \Lambda(T), \tag{3.23}$$

where $\Lambda(T)$ is the radiative loss function.

The radiative loss function Λ is calculated as:

$$\Lambda(T) = \zeta \Lambda_{\rm GJ}(T) + (1-\zeta)\,\Lambda_{\rm C}(T) \tag{3.24}$$

$$\zeta = \max\left[0, \min\left(1, \frac{T_1 - T}{T_1 - T_0}\right)\right] \tag{3.25}$$

Here, we employ the loss function $\Lambda_{\rm C}(T)$ from Chianti Atomic Database ver. 7.1 (Landi et al., 2012) in the high temperature region, assuming the coronal abundance. We use the "effectively optically thin" radiative loss function $\Lambda_{\rm GJ}$ by Goodman & Judge (2012) in the low temperature region. We set $T_0 = 10000$ K and $T_1 = 15000$ K.

3.2.4 Thermal conduction

The Spitzer-type thermal conduction is energetically important in the transition region and the corona. The heating rate by the an-isotropic thermal conduction is written as follows:

$$Q_{\rm cnd} = -\nabla \cdot \boldsymbol{F}^{\rm cnd} \tag{3.26}$$

$$\boldsymbol{F}^{\rm cnd} = -\kappa\,(\boldsymbol{b} \otimes \boldsymbol{b}) \cdot \nabla T \tag{3.27}$$

Here, we set $\kappa = \kappa_0 T^{5/2}$ and $\kappa_0 = 10^{-6}$ (in c.g.s.). $\boldsymbol{b} = \boldsymbol{B}/B$ is the unit vector parallel to the magnetic field.

The conductive heating roughly balances with radiative cooling near the chromosphere-corona transition region. We can estimate the thickness of the transition region as several

tens of kilometers assuming this balance. However, the numerical grid size required to resolve such thin structure becomes several km, which is too computationally high. In this study, we artificially increase the thermal conductivity κ near the transition region so that the transition region becomes thick enough.

3.3 Numerical methods

3.3.1 Magnetohydrodynamics

We use the MHD scheme described in the previous chapter. We modify several points for the numerical stability mainly under the strong variation of mass density and temperature near the transition region and the strong shock waves in the very low plasma beta region.

First, the reconstruction variables are changed. In this radiation MHD code, we reconstruct the logarithm of mass density $\log \rho$, the internal energy per unit mass $e_{\rm int}/\rho$, the gas pressure divided by mass density P/ρ, the velocity field $\boldsymbol{V}$, and the magnetic flux density $\boldsymbol{B}$. Here, we reconstruct both P/ρ and $e_{\rm int}/\rho$ to reduce the numerical cost for the interpolation of tabulated equation of states.

We use the combination of the fifth-order WENO-Z scheme (Borges et al., 2008) and piecewise linear method with minmod limiter. The minmod limiter is applied near the shock front, transition region, and region with very low temperature. This is fulfilled by the use of flattener $\tilde{d}_{i,j,k}$ defined as follows:

$$d^{\rm shock}_{i,j,k} = \max\left[0, \min\left(1, -1 - \frac{\Delta V}{M_0 C_{s;min}}\right)\right] \tag{3.28}$$

$$\Delta V = \min\left(\Delta x, \Delta y, \Delta z\right)\left(\nabla \cdot \boldsymbol{V}\right)_{i,j,k} \tag{3.29}$$

$$d^{\rm TR}_{i,j,k} = \frac{1}{2}\left[1 + \tanh\left(\frac{R - R_0}{\Delta R}\right)\right] \tag{3.30}$$

$$R = T_{\rm max}/T_{min} \tag{3.31}$$

$$d^{\rm low}_{i,j,k} = \frac{1}{2}\left[1 + \tanh\left(\frac{T_{\rm min,0} - T_{\rm min}}{\Delta T_{\rm min}}\right)\right] \tag{3.32}$$

$$d_{i,j,k} = \max\left(d^{\rm shock}_{i,j,k}, d^{\rm TR}_{i,j,k}, d^{\rm low}_{i,j,k}\right) \tag{3.33}$$

$$\tilde{d}_{i,j,k} = \max\left(d_{i,j,k}, d_{i-1,j,k}, d_{i+1,j,k}, d_{i,j-1,k}, d_{i,j+1,k}, d_{i,j,k-1}, d_{i,j,k+1}\right) \tag{3.34}$$

Here, we set $M_0 = 0.4$, $R_0 = 10$, $\Delta R = 1$, $T_{\rm min,0} = 2000$ K, and $\Delta T_{\rm min} = 10$ K. $U_{\rm max}$ ($U_{\rm min}$) for variable U represents the maximum (minimum) among the nearby cells (i,j,k), $(i-1,j,k)$, $(i+1,j,k)$ $(i,j-1,k)$, $(i,j+1,k)$, $(i,j,k-1)$, and $(i,j,k+1)$. $(\nabla \cdot \boldsymbol{V})_{i,j,k}$ is evaluated by the second-order central difference. The functional form of flattener for the shock front $d^{\rm shock}_{i,j,k}$ is suggested by Balsara (2012). We use the sound speed C_s instead of the speed of fast-mode so that the flattener becomes sensitive near the slow-mode shock front in the low plasma beta region. We combine the slope from the fifth-order WENO-Z scheme $\Delta^D_{{\rm WZ};s}U$ ($s = x, y, z$、 $D = L, R$) and the piecewise linear slope with minmod limiter $\Delta^D_{{\rm MM};s}U$ as follows:

$$\Delta^D_s U = \tilde{d}_{i,j,k}\Delta^D_{{\rm WZ};s}U + \left(1 - \tilde{d}_{i,j,k}\right)\Delta^D_{{\rm MM};s}U \tag{3.35}$$

Following the strategy in Balsara (2004) to limit the primitive variables, we apply the flattener to the reconstruction of the internal energy, gas pressure, and velocity field because they are strongly related with compressive mode. We do not apply the flattener to the mass density nor magnetic field because they are mainly affected by the entropy mode and Alfvén mode. This approach allows us to achieve the high numerical stability without diffusing the sharp density contrast or the fine structure of magnetic field.

The gas pressure and internal energy can be very small near the strong shock wave in the corona. To maintain the stability under such situation, we also solve the internal energy equation, without the viscous nor Joule heating, in addition to the total energy

equation. The internal energy equation is written as:

$$\left(\frac{\partial e_{\rm int}}{\partial t}\right)_{\rm ad} = -\nabla\cdot(e_{\rm int}\boldsymbol{V}) - P\nabla\cdot\boldsymbol{V} + Q_{\rm cnd} + Q_{\rm rad} + Q_{\rm art} \tag{3.36}$$

The left-hand side in Eq. (3.36) does not include the dissipative heating terms that come from the artificial diffusion of upwind scheme in the momentum and induction equations. Because these heating processes are automatically included in the total energy equation, the inequality

$$\frac{\partial e_{\rm int}}{\partial t} = \left(\frac{\partial e_{\rm int}}{\partial t}\right)_{\rm tot} = \frac{\partial e}{\partial t} - \frac{\partial}{\partial t}\left(\frac{1}{2}\rho V^2 + \frac{1}{8\pi}B^2\right) \geq \left(\frac{\partial e_{\rm int}}{\partial t}\right)_{\rm ad} \tag{3.37}$$

should be satisfied. Based on this inequality, we use $(\partial e_{\rm int}/\partial t)_{\rm ad}$ as the lower bound of $\partial e_{\rm int}/\partial t$ so that the unrealistic low energy is suppressed in low plasma beta regions. In the practical case, this inequality is not strictly satisfied because of the discretization errors. Thus, we force the lower bound using the coefficient $C_{\rm damp} \leq 1$ as:

$$\frac{\partial e_{\rm int}}{\partial t} = \max\left[\left(\frac{\partial e_{\rm int}}{\partial t}\right)_{\rm tot}, C_{\rm damp}\left(\frac{\partial e_{\rm int}}{\partial t}\right)_{\rm ad}\right] \tag{3.38}$$

$C_{\rm damp}$ is defined as:

$$C_{\rm damp} = \min\left[C_{\rm ub}, \max\left(C_{\rm lb}, \frac{\alpha}{C_0+\alpha}\right)\right] \tag{3.39}$$

$$\alpha = p_{\rm mag}/p_{\rm gas},\ \beta = 1/\alpha \tag{3.40}$$

This definition makes $C_{\rm damp} \sim C_{\rm lb}$ when $\beta \gg 1$, and $C_{\rm damp} \sim 1 - C_0\beta$ when $\beta \ll 1$. This choice allows maintaining the positivity of gas pressure in the low plasma beta region without affecting the high beta region. We set $C_{\rm ub} = 1$, $C_{\rm lb} = 0.99$, $C_0 = 0.03$ in this study.

3.3.2 Equation of state

We have to calculate the gas pressure, gas temperature, and electron density from the mass density and internal energy as the equation of states. First, we calculate the internal energy as a function of mass density and temperature assuming that the mass density and temperature is given. We employ the iteration method on the electron density, which is written as follows:

1. Set initial guess of the number density of electron.
2. Calculate the number density of all energy levels, ionization states, and molecules from the Saha-Boltzmann equation (Eq. (3.9)), the chemical equilibrium equation (Eq. (3.10)), and the Saha's equation for ionization equilibrium (Eq. (3.12)) in addition to the conservation of atomic nuclei for each element (Eqs. (3.8) and (3.11)).
3. Update the electron density from the charge conservation law (Eq. (3.13)).
4. Repeat from step 2 to step 3 until the change of electron number density becomes small enough.
5. Calculate the internal energy from Eq. (3.15).

The gas temperature is calculated for the given mass density and internal energy, inverting the internal energy as a function of mass density and temperature, by applying the bisection method on the temperature. Once the number densities and temperature is calculated from the mass density and internal energy, the gas pressure is directly calculated from Eq. (3.14). The equation of states is stored in the numerical table and numerically interpolated during the time integration. The variables are linearly interpolated in the logarithmic space.

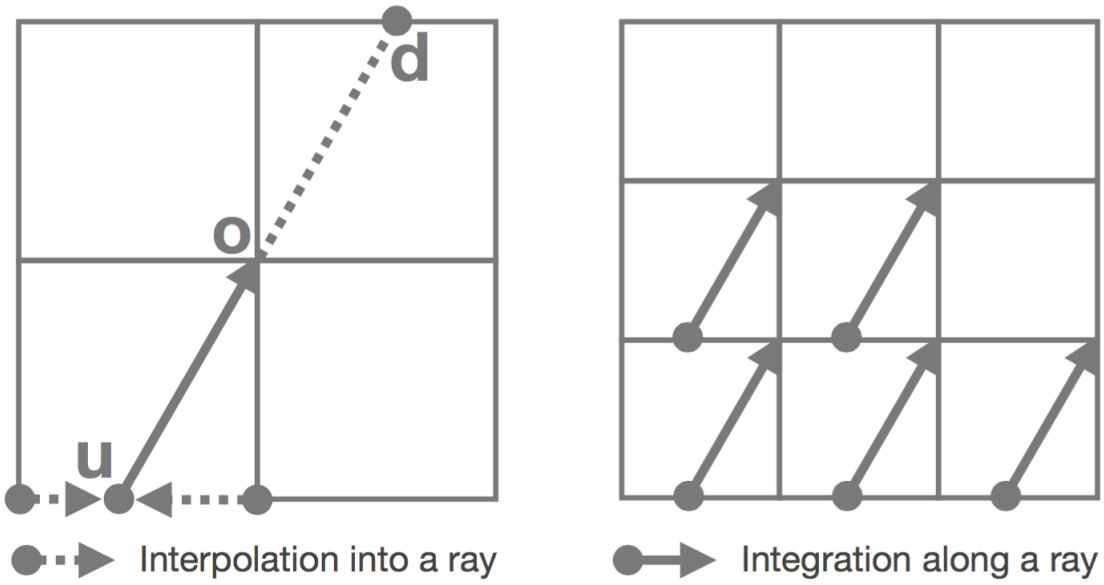

Figure 3.1: Left panel: Schematic illustration of the short-characteristic method for a single computational cell. First, the radiative intensities defined on cell corners are interpolated into the point u on a characteristic ray. Then, it is integrated along a ray uo based on the formal solver of radiative transfer equation. Right panel: Schematic illustration of the short-characteristic method for the multiple computational cells.

3.3.3 Radiation

Optically thick radiation

The radiative transfer equation is integrated by the short characteristic method (Mihalas et al., 1978; Kunasz & Auer, 1988), which has an advantage in the parallelization by the domain decomposition. In this method, we consider short characteristic ray for each numerical cell, and solved by the combination of interpolation into a ray and integration along the ray (Figure 3.1). The equation is integrated along the ray using the formal solution of the radiative transfer equation:

$$I_{\rm o} = I_{\rm u}{\rm e}^{-\Delta\tau_{\rm uo}} + {\rm e}^{-\Delta\tau_{\rm uo}} \int_0^{\Delta\tau_{\rm uo}} S(\tau){\rm e}^{\tau}{\rm d}\tau \tag{3.41}$$

Here, $I_{\rm w}$ is the intensity at the point w (= u, o, d) and $\Delta\tau_{\rm ab}$ is the optical depth of the ray segment ab, which is calculated by the second-order form given by

$$\Delta\tau_{\rm ab} = \frac{1}{2}\left(\alpha_{\rm a} + \alpha_{\rm b}\right)\Delta l_{\rm ab} \tag{3.42}$$

where $\Delta l_{\rm ab}$ is the length of the ray segment ab and $\alpha_{\rm w}$ is the absorption coefficient at the point w. We use the bi-linear interpolation for the interpolation into the ray.

We have to calculate the analytic profile of the source function along the line segment to integrate Eq. (3.41). In this study, we use the second-order Bézier interpolation in the region $\tau \in [0, \Delta\tau_{\rm uo}]$, given by

$$S(\tau) = (1-y)^2 S_{\rm u} + y^2 S_{\rm o} + 2y(1-y)S_{\rm c}, \tag{3.43}$$

where $y = \tau/\Delta\tau_{\rm uo}$. $S_{\rm w}$ is the source function $S(T)$ at the point w (= u, o, d) in Figure 3.1, respectively. The above equation is equivalent to the second-order polynomial interpolation when the control point $S_{\rm c}$ is defined by:

$$S_{\rm c} = S_{\rm o} - \frac{\Delta\tau_{\rm uo}}{2} S'_{\rm o} \tag{3.44}$$

$$S'_{\rm o} = \frac{\Delta\tau_{\rm od} S'_{\rm uo} + \Delta\tau_{\rm uo} S'_{\rm od}}{\Delta\tau_{\rm uo} + \Delta\tau_{\rm od}} \tag{3.45}$$

$$S'_{\rm uo} = \frac{S_{\rm o} - S_{\rm u}}{\Delta\tau_{\rm uo}} \tag{3.46}$$

$$S'_{\rm od} = \frac{S_{\rm d} - S_{\rm o}}{\Delta\tau_{\rm od}} \tag{3.47}$$

We force the monotonicity condition for the segment uo (Auer, 2003)

$$\min\left(S_{\rm u}, S_{\rm o}\right) \leq S_c \leq \max\left(S_{\rm u}, S_{\rm o}\right) \tag{3.48}$$

when $S'_{\rm uo} S'_{\rm od} > 0$ to prevent the numerical oscillation. This condition is satisfied by

taking $S_{\rm c}$ as follows:

$$S_{\rm c} = S_{\rm o} - \frac{\Delta\tau_{\rm uo}}{2} S'_{\rm MM} \tag{3.49}$$

$$S'_{\rm MM} = \mathrm{minmod}\left(\theta S'_{\rm uo}, S'_{\rm o}\right),\ \theta \in [1,2] \tag{3.50}$$

The monotonicity condition is satisfied for arbitrary $\theta \in [1,2]$. When $S_{\rm c} = 0$, $S'_{\rm uo} S'_{\rm od} \leq 0$ and the source functions $S_{\rm u}$, $S_{\rm o}$, and $S_{\rm d}$ have an extremum at the point o, so that the interpolation does not produce the new extremum. Smaller θ produces more numerical stable (but diffuse) interpolation. We set $\theta = 2$ in this study. $\mathrm{minmod}(a,b)$ is the minmod function implemented as:

$$\mathrm{minmod}(a,b) = [\mathrm{sign}(0.5,a) + \mathrm{sign}(0.5,b)] \min\left(|a|, |b|\right) \tag{3.51}$$

Here, $\mathrm{sign}(a,b)$ is the sign function defined in Fortran, which returns the absolute of a with the sign of b. We also set

$$S'_{\rm MM} = 0 \tag{3.52}$$

when $\Delta\tau_{\rm uo}\Delta\tau_{\rm od} < 10^{-10}$ to avoid the division by zero.

Using the above-mentioned monotonic interpolation, the radiative intensity at the point o $I_{\rm o}$ is derived from the formal solution of the radiative transfer equation Eq. (3.41) as follows:

$$I_{\rm o} = I_{\rm u} \mathrm{e}^{-\Delta\tau_{\rm uo}} + \Delta I \tag{3.53}$$

$$\Delta I = (V_0 - 2V_1 + V_2) S_{\rm u} + V_2 S_0 + 2(V_1 - V_2) S_c \tag{3.54}$$

$$V_0 = 1 - \mathrm{e}^{-\Delta\tau_{\rm uo}} \tag{3.55}$$

$$V_1 = 1 - \frac{V_0}{\Delta\tau_{\rm uo}} \tag{3.56}$$

$$V_2 = 1 - \frac{2V_1}{\Delta\tau_{\rm uo}} \tag{3.57}$$

here, V_0, V_1, and V_2 include the division by $\Delta\tau_{\rm uo}$. We use the limit expression for $\Delta\tau_{\rm uo} \to$

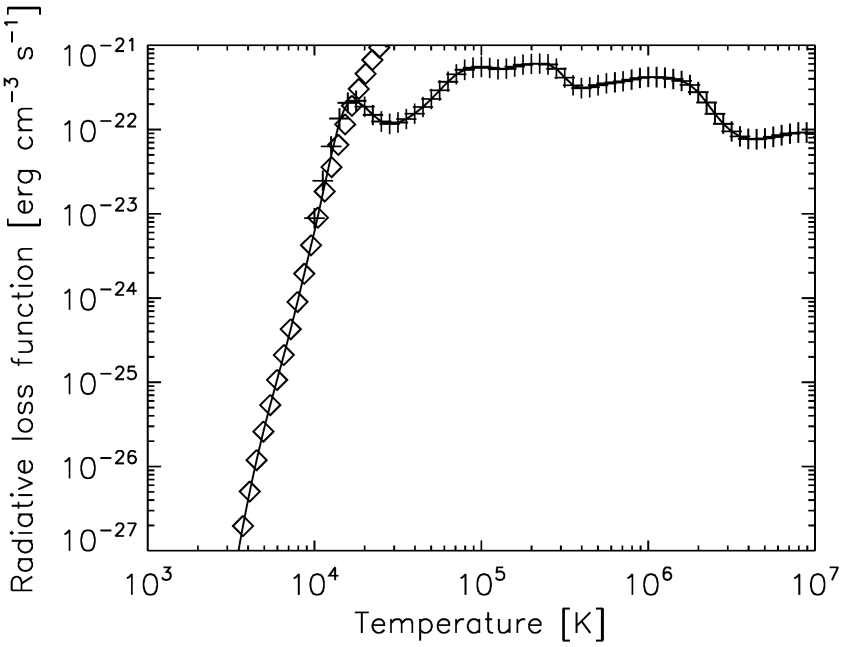

Figure 3.2: Radiative loss functions used in this study. The implemented radiative loss function (solid line), one calculated from Chianti atomic database (crosses), and one from Goodman & Judge (2012) (diamonds) are shown.

0 given by

$$V_0 \to \Delta\tau_{\rm uo}, \tag{3.58}$$

$$V_1 \to \frac{1}{2}\Delta\tau_{\rm uo}, \tag{3.59}$$

$$V_2 \to \frac{1}{3}\Delta\tau_{\rm uo}, \tag{3.60}$$

when $\Delta\tau_{\rm uo} < 10^{-4}$ to prevent the division-by-zero.

In this study, the radiative intensity I is defined at the nodes of the cells for MHD calculation to avoid the odd-even decoupling. The source function and absorption coefficient are linearly interpolated into the nodes. The radiative heating rate at the cell center for the MHD simulation is calculated from the radiative intensity at the nodes, after the integration of the radiative transfer equation.

Optically thin radiation

The radiative loss function taken from Chianti Atomic Database $\Lambda_{\rm C}$ is linearly interpolated from the numerical table in the logarithmic space. The radiative loss function defined in Goodman & Judge (2012) $\Lambda_{\rm GJ}$ is calculated during the time integration. The combined radiative loss function Λ is shown in Figure 3.2.

3.3.4 Thermal conduction

The spatial discretization of the thermal conduction is essentially same as the appendix in Yokoyama & Shibata (2001) or "centered asymmetric scheme" in Sharma & Hammett (2007). As pointed out in Sharma & Hammett (2007), the standard central difference discretization of an-isotropic thermal conductive flux cannot maintain the monotonicity of the temperature where the temperature gradient is very large. Following the suggestion in Sharma & Hammett (2007), we apply the limiter for the an-isotropic terms in the thermal conductive flux. The thermal conductive flux in x-direction $F_x^{\rm cnd}$ at the cell face is written as:

$$\begin{aligned} F^{\rm cnd}_{x;i+1/2,j,k} = &- \overline{\kappa}_{i+1/2,j,k} b^2_{x;i+1/2,j,k} \delta_x T \\ &- \overline{\kappa}_{i+1/2,j,k} b_{x;i+1/2,j,k} b_{y;i+1/2,j,k} \delta_y T \\ &- \overline{\kappa}_{i+1/2,j,k} b_{x;i+1/2,j,k} b_{z;i+1/2,j,k} \delta_z T \end{aligned} \tag{3.61}$$

$$\overline{\kappa}_{i+1/2,j,k} = \left(2\kappa_{i,j,k}\kappa_{i+1,j,k}\right) / \left(\kappa_{i,j,k} + \kappa_{i+1,j,k}\right) \tag{3.62}$$

$$\delta_x T = \frac{1}{\Delta x}\left(T_{i+1,j,k} - T_{i,j,k}\right) \tag{3.63}$$

$$\begin{aligned}\delta_y T = \frac{1}{\Delta y} L_{\rm M4}\,&\left(T_{i,j,k} - T_{i,j-1,k}, T_{i+1,j,k} - T_{i+1,j-1,k},\right.\\ &\left. T_{i,j+1,k} - T_{i,j,k}, T_{i+1,j+1,k} - T_{i+1,j,k}\right)\end{aligned} \tag{3.64}$$

$$\begin{aligned}\delta_z T = \frac{1}{\Delta z} L_{\rm M4}\,&\left(T_{i,j,k} - T_{i,j,k-1}, T_{i+1,j,k} - T_{i+1,j,k-1},\right.\\ &\left. T_{i,j,k+1} - T_{i,j,k}, T_{i+1,j,k+1} - T_{i+1,j,k}\right)\end{aligned} \tag{3.65}$$

Here, $\boldsymbol{b}_{i+1/2,j,k}$ is the unit vector parallel to the magnetic field at the cell surface $(i + 1/2, j, k)$. $L_{\rm M4}(a, b, c, d)$ is the limiter similar to the Monotonized Central (MC) limiter defined as:

$$L_{\rm M4}(a, b, c, d) = \mathrm{minmod5}\left[0.25(a + b + c + d), 2a, 2b, 2c, 2d\right] \tag{3.66}$$

Here, the minmod function for five arguments are implemented as follows:

$$\begin{aligned}\mathrm{minmod5}(a, b, c, d, e) = &\left[\mathrm{sign}(0.5, a) + \mathrm{sign}(0.5, b)\right]\\ &\left|\mathrm{sign}(0.5, b) + \mathrm{sign}(0.5, c)\right| \left|\mathrm{sign}(0.5, c) + \mathrm{sign}(0.5, d)\right|\\ &\left|\mathrm{sign}(0.5, d) + \mathrm{sign}(0.5, e)\right| \min\left(|a|, |b|, |c|, |d|, |e|\right)\end{aligned} \tag{3.67}$$

This limiter is different from the suggestion in Sharma & Hammett (2007), but it has an advantage that it is symmetric for the exchange of coordinate axis. y and z-directed thermal conductive flux is calculated in the same way. The conductive heating rate $Q_{\rm cnd}$ is written as:

$$\begin{aligned}Q_{{\rm cnd};i,j,k} = &-\frac{1}{\Delta x}\left(F^{\rm cnd}_{x;i+1/2,j,k} - F^{\rm cnd}_{x;i-1/2,j,k}\right)\\ &-\frac{1}{\Delta y}\left(F^{\rm cnd}_{y;i,j+1/2,k} - F^{\rm cnd}_{y;i,j-1/2,k}\right)\\ &-\frac{1}{\Delta z}\left(F^{\rm cnd}_{z;i,j,k+1/2} - F^{\rm cnd}_{z;i,j,k-1/2}\right)\end{aligned} \tag{3.68}$$

This discretization is second-order in space.

3.3.5 Time advance

The criterion for the time stepping from the thermal conduction is generally much (about several tens to thousands times) severe than that from the magnetohydrodynamics. In order to avoid too small time step, we use the second-order operator splitting method (Strang, 1968) and solve the magnetohydrodynamics and thermal conduction independently. The algorithm is written as:

1. Determine the time step Δt.
2. Integrate the thermal conduction for $\Delta t/2$.
3. Integrate the magnetohydrodynamics for Δt.
4. Integrate the thermal conduction for $\Delta t/2$.
5. Go back to step 1.

Following this method, we can achieve the second-order accuracy in time if the time integration scheme of the thermal conduction and magnetohydrodynamics is more than second-order.

The radiative heating rate and gravitational force is simultaneously integrated with the MHD equations, by the third-order optimal SSP Runge-Kutta method (Jiang & Shu, 1996). For the evolution equation in the form of

$$\frac{\partial U}{\partial t} = S(U), \tag{3.69}$$

this scheme is written as:

$$\begin{aligned} U^{(1)} &= U^n + \Delta t S\left(U^n\right) \\ U^{(2)} &= \frac{3}{4}U^n + \frac{1}{4}U^{(1)} + \frac{1}{4}\Delta t S\left(U^{(1)}\right) \\ U^{n+1} &= \frac{1}{3}U^n + \frac{2}{3}U^{(1)} + \frac{2}{3}\Delta t S\left(U^{(2)}\right) \end{aligned} \tag{3.70}$$

The time integration scheme for the thermal conduction equation is the second-order Runge-Kutta-Legendre (RKL2) Super Time Stepping (STS) method by Meyer et al. (2012, 2014). In the STS method (Alexiades et al., 1996), the stability criterion for the time stepping is forced for the multiple step in contrast to the ordinary Courant-Friedrichs-Lewy condition (Courant et al., 1967). By carefully choosing the relative widths of the multiple time stepping, the criterion for the time stepping can be much more relaxed. This method is suitable for the stiff problems and massively parallel computation because the equation can be integrated like the explicit method. Moreover, because we employ the nonlinear flux limiter for the thermal conduction, the implicit method like Yokoyama & Shibata (2001) is not suitable. For the number of substep N and the time step τ (e.g., $\Delta t/2$), the RKL2 STS method for the evolution equation Eq. (3.69) is written as follows:

$$\begin{aligned} U_0 =& U^n \\ U_1 =& U_0 + \tilde{\mu}_1 \tau S\left(U_0\right) \\ U_j =& \mu_j U_{j-1} + \nu_j U_{j-2} + \left(1-\mu_j-\nu_j\right) U_0 \\ &+ \tilde{\mu}_j \tau S\left(U_{j-1}\right) + \tilde{\gamma}_j \tau S\left(U_0\right); \quad 2 \le j \le N \\ U^{n+1/2} =& U_N \end{aligned} \tag{3.71}$$

Here, each coefficients are determined as:

$$\begin{aligned} \mu_j =& \frac{(2j-1)(j+2)(j-1)^2}{j(j-2)(j+1)^2} \\ \nu_j =& -\frac{(j-1)^3(j^2-4)}{j^3(j+1)(j-3)} \\ \tilde{\mu}_j =& \frac{(2j-1)(j+2)(j-1)^2}{j(j-2)(j+1)^2}\frac{4}{N^2+N-2}, \quad \tilde{\mu}_1 = \frac{4}{3(N^2+N-2)} \\ \tilde{\nu}_j =& -\frac{(j-1)(j+2)(2j-1)(j^2-j+2)}{2j^2(j-2)(j+1)^2} \end{aligned} \tag{3.72}$$

The stability condition for τ is given by

$$\tau \le \Delta t_{\exp} \frac{N^2+N-2}{4}. \tag{3.73}$$

Here, $\Delta t_{\rm exp}$ is the maximum time step allowed for the single step of the first-order forward Euler method.

The total time step Δt is determined as follows. First, we calculate the maximum time step allowed for the magnetohydrodynamics $\Delta t_{\rm mhd}$ and thermal conduction $\Delta t_{\rm cnd}$. Next, we determine the number of substep N for the STS method from

$$N = \min\left[\mathrm{floor}\left(\frac{1}{2}\sqrt{9+16\frac{\tau}{\Delta t_{\rm cnd}}}-\frac{1}{2}\right), 50\right], \tag{3.74}$$

where we set $\tau = \Delta t_{\rm mhd}/2$. The maximum allowed time step τ' for the STS method is calculated from Eq. (3.73) using N derived above. Finally, we get the time step for the whole scheme as $\Delta t = \min(2\tau', \Delta t_{\rm mhd})$. Here, we set the upper bound of N to be 50. Although the RKL2 STS method shows the second-order convergence, the time discretization error is not small enough when N is very large. This upper bound is set so that the physical characteristics of the thermal conduction are not altered. This upper bound is required only for the situation with very hot corona with small magnetic field. The simulations introduced in this dissertation are not affected by this criterion.

Chapter 4

Two-dimensional simulation of solar chromospheric jets: effect of the coronal condition

4.1 Introduction

Various chromospheric jets are observed in the solar atmosphere. In quiet regions and coronal holes, we observe classical (type I) spicules at the limb, which have maximum lengths of 4–10 Mm, lifetimes of 1–7 min, and maximum upward velocities of 20–100 km/s (Beckers, 1972). Recently, the existence of more violent "type II" spicules is reported (De Pontieu et al., 2007b). The type I and II spicules are considered to have their on-disk counterparts of mottles (Rouppe van der Voort et al., 2007) and the rapid blue-shifted events (RBEs) (De Pontieu et al., 2009; Rouppe van der Voort et al., 2009; McIntosh & De Pontieu, 2009), respectively. The dynamic fibrils observed on the disk in active regions have maximum lengths of several Mm, lifetimes of 2–8 min, and maximum velocities of 10–40 km/s (Hansteen et al., 2006; De Pontieu et al., 2007a). Rouppe van der Voort et al. (2007) reported that the dynamic fibrils are considered to be the active region counterpart of the quiet-sun mottles.

Theoretical studies have suggested various models for these chromospheric jets (see Sterling, 2000, for a review). For the dynamic fibrils, the periodic acoustic wave model is in agreement with observations (Hansteen et al., 2006; De Pontieu et al., 2007a; Heggland et al., 2007), particularly in terms of the correlation between deceleration and maximum velocity. The origin of spicules (types I and II) is still under debate. Many candidates, such as acoustic waves (e.g., Hollweg, 1982; Suematsu et al., 1982), Alfvén waves (e.g., Hollweg et al., 1982; Kudoh & Shibata, 1999), and magnetic reconnection (e.g., Uchida, 1969; Heggland et al., 2009; Takasao et al., 2013) have been suggested. Most of these models include a process by which the transition region is lifted by the shock wave propagating upward into the corona. This process is called the shock-transition region interaction (Hollweg, 1982). Several multi-dimensional simulations with the sophisticated modeling of convective motion have been reported (Hansteen et al., 2006; Martínez-Sykora et al., 2009; Heggland et al., 2011). Although some of these studies is intended to be the representative for quiet regions, the simulated chromospheric jets was significantly shorter than the observed spicules.

Using idealized one-dimensional hydrodynamic simulations, Shibata & Suematsu (1982) explained why the spicules are long in the coronal hole. The key process is the amplification of the strength of the shock wave in the solar chromosphere. Based on their idea, we investigate the effect of the coronal temperature on the scale of the solar chromospheric jets using two-dimensional magnetohydrodynamic simulations with more realistic physical processes, to provide a unified perspective on the quiet region spicules, the coronal hole spicules, and the active region dynamic fibrils.

4.2 Simulation setup

The basic equations and numerical methods are described in the previous chapters. We do not repeat them here.

The two-dimensional numerical domain in the XZ-plane extends from 2 Mm below

the surface to 14 Mm above. The horizontal extent is 18 Mm. The uniform grid size is 42 km in the horizontal direction and 32 km in the vertical direction.

The bottom boundary condition is the "open" boundary. The total (gas plus magnetic) pressure equilibrium is assumed. The entropy of the upward plasma is fixed. The upward velocity field is slowly damped to the horizontally uniform up flow that complements the mass flux by the downward flow (e.g., Bercik, 2002). This weak damping is not important in the present results but able to suppress the unrealistic instability that appears after the long time integration. The downward plasma evolves adiabatically and freely. The top boundary has a free-slip condition and is open for vertical flow. The density is extrapolated exponentially by the scale height at the boundary. Our two-dimensional simulation with a top boundary at the lower corona cannot maintain the 1 MK coronal temperature (e.g., Leenaarts et al., 2011; Heggland et al., 2011). To prevent the corona from being cooled by radiation and thermal conduction, the conductive flux is introduced through the top boundary to heat the corona. In this study, the conductive flux is adjusted to preserve the different coronal temperature at the top boundary, $T_{\rm c}$. The magnetic field is assumed to be vertical at the top and bottom boundaries. The periodic boundary condition is employed horizontally.

The initial condition is the plane-parallel atmosphere with a uniform vertical magnetic field of 3 G. The sufficiently relaxed convection is obtained after the integration of 5 solar hours (5 hours in the internal time of the simulation) with a temperature at the top boundary, $T_{\rm c}$, of 1 MK. We impose the uniform vertical magnetic field of 30 G on the relaxed atmosphere and integrate another 3 solar hours with the same $T_{\rm c}$. Next, we change the temperature at the top boundary, $T_{\rm c}$, to 2, 1, and 0.4 MK to imitate the conditions of the active region, the quiet region, and the coronal hole, respectively. The simulations are integrated for another 1 solar hour after the change of $T_{\rm c}$. We find that the coronal density and temperature reach statistical equilibrium within 20 min. The data analyzed below is the last 30 min of each simulation.

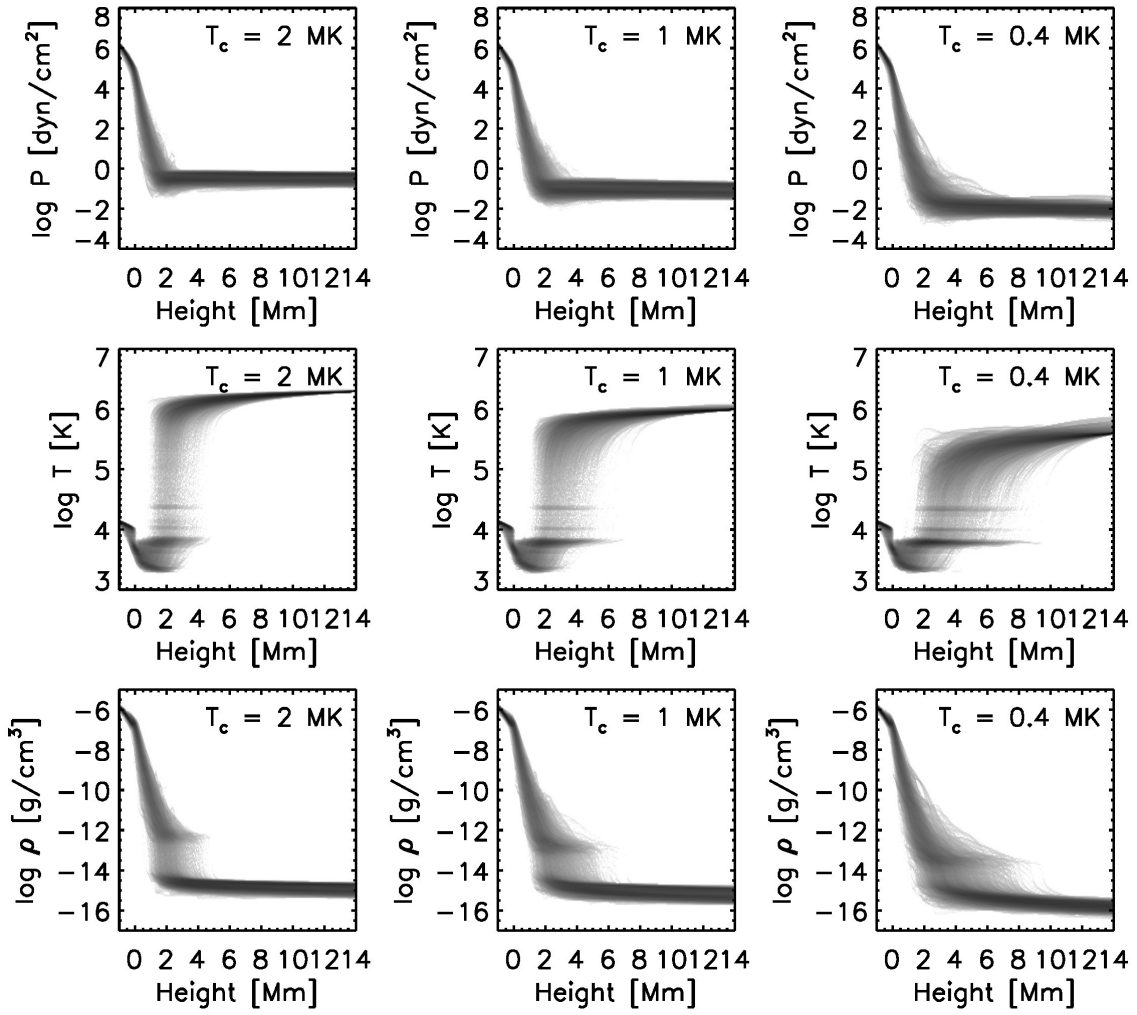

Figure 4.1: Vertical structure of the three simulations with the different temperatures at the top boundary, $T_{\rm c} = 2$ MK (left column), 1 MK (middle column), and 0.4 MK (right column). The probability density functions (PDFs) of gas pressure (top row), temperature (middle row), and mass density (bottom row) are shown.

4.3 Structure of atmosphere

Figure 4.1 presents the vertical structure of the three simulated atmospheres. The higher temperature at the top boundary $T_{\rm c}$ leads higher gas pressure and mass density. Because the optically thin radiative cooling, which is proportional to the square of density, roughly balances to the conductive heating from the corona, the higher density is required. We also observe that the chromospheric material is extended to the higher altitude with the lower coronal temperature. These results indicate the dependence of chromospheric jets

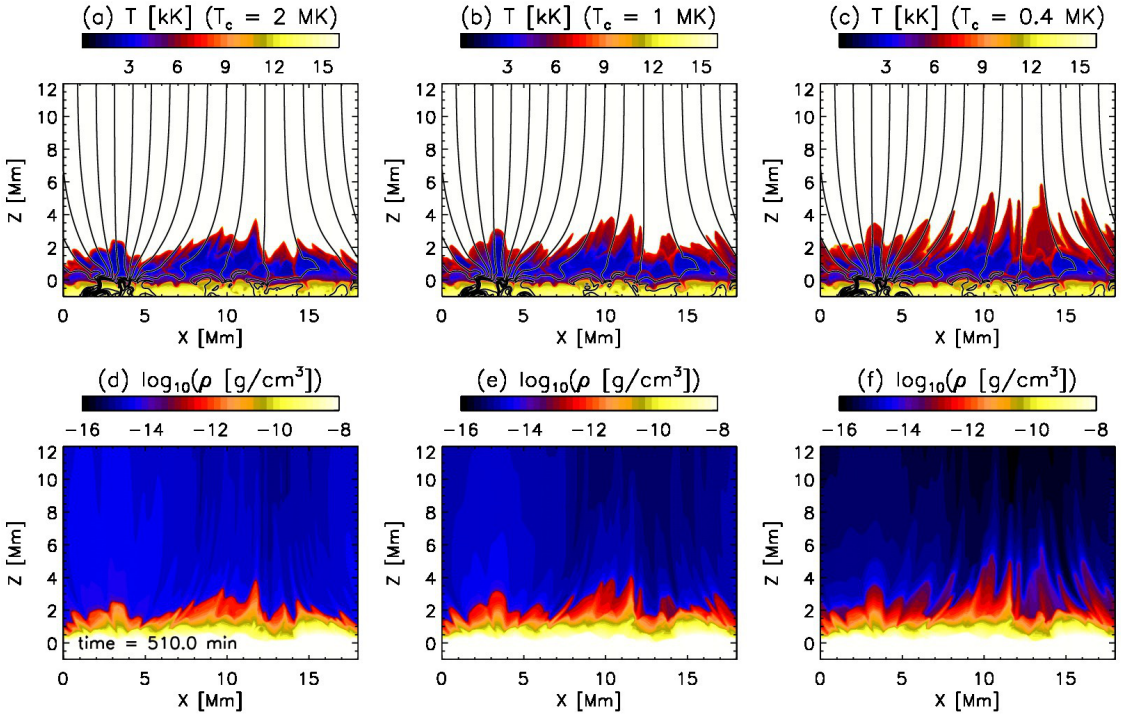

Figure 4.2: Snapshots from the three simulations with the different temperatures at the top boundary, $T_{\rm c}$. Panels (a)–(c) show the temperature, and panels (d)–(f) represent the logarithm of mass density. The solid lines in panels (a)–(c) indicate the magnetic field lines. Panels (a) and (d) correspond to the simulation with $T_{\rm c} = 2$ MK, panels (b) and (e) correspond to the simulation with $T_{\rm c} = 1$ MK, and panels (c) and (f) correspond to the simulation with $T_{\rm c} = 0.4$ MK.

on the coronal temperature.

Figure 4.2 shows snapshots from three simulations with the temperature at the top boundary, $T_{\rm c}$, set to 2, 1, and 0.4 MK. We find the strong magnetic field concentration near $X = 8$ Mm. Because the magnetic field structure is essentially the same among these three simulations, we can concentrate on the effect of the coronal temperature. The jet-like structures with various scales are formed in the chromosphere. These structures are basically driven by the shock waves, arising from convective motion, which pass through the transition region. This process is consistent with both the one-dimensional simulations (Hollweg et al., 1982; Suematsu et al., 1982) and multi-dimensional simulations (Heggland et al., 2011). We clearly find that the simulation with a lower coronal temperature produces higher chromospheric jets. The density near the top of each jet and

over the entire corona is smaller when $T_{\rm c}$ is lower. The widths of the produced jets in these simulations are approximately independent of $T_{\rm c}$ if measured at a specific height like $Z = 3$ Mm, but the jets become sharper near their tops in the lower $T_{\rm c}$ simulations.

4.4 Time evolution of chromospheric jets

We automatically detect the chromospheric jets in the simulations for the purpose of quantitative comparison. We assume that each jet is approximately vertical. The top of each jet is detected as the local maximum of the height of the transition region over the temporal and horizontal directions. The height of the transition region is defined where the temperature is 40,000 K following Heggland et al. (2011). From the top of each jet, the time variation of the height of the transition region along the magnetic field line is calculated. The appearance and disappearance times of each jet are defined as the nearby local minimum of this time variation of the transition region height. The resulting motion of the transition region is fitted by a parabola, and the maximum height from $Z = 0$ Mm, maximum length from the initial height of the transition region, lifetime, maximum upward velocity, and deceleration for each jet is calculated from the fitting. The jets with large deviation from the parabola or large asymmetry of the rising and falling period are removed from the analysis below, because such types of jets suffer from serious fitting errors and/or difficulty in being distinguished from overlapping jets. We find that this procedure does not alter the qualitative picture shown below.

An example of the time-distance plots for short chromospheric jets in the $T_{\rm c} = 2$ MK case is shown in Figure 4.3. The automatic detection algorithm provides the maximum height of 4.3 Mm, maximum length of 2.7 Mm, lifetime of 255 s, maximum upward velocity of 45 km/s, and deceleration of 350 m/s^2. The top of the jet is located at $X = 12.8$ Mm, which is outside of the strong magnetic field concentration at $X = 4$ Mm. The trajectories of shock fronts are identified by the divergence of velocity field. The shock front hits the transition region at the time of 532 min and propagates into the corona.

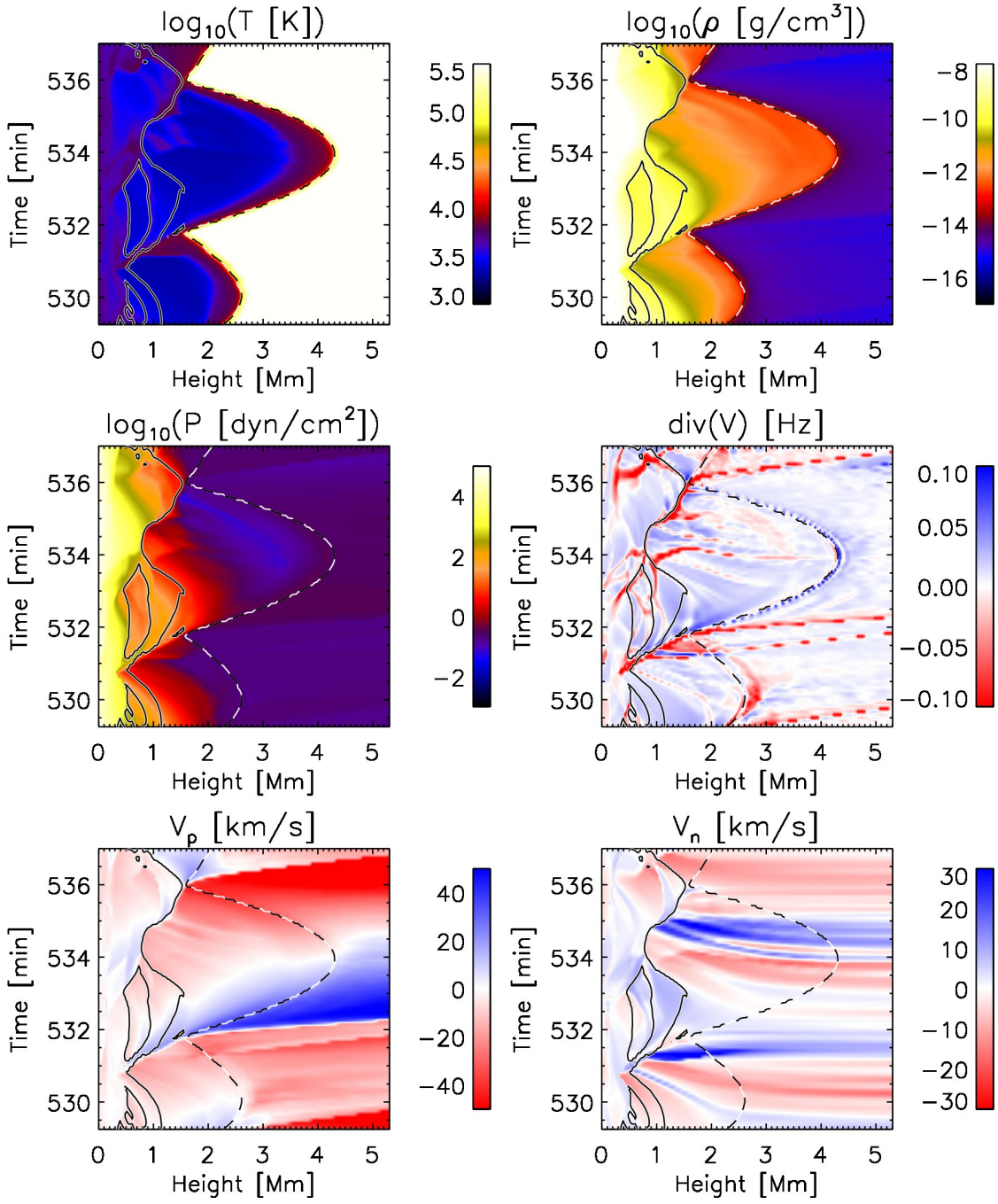

Figure 4.3: Time-distance plots showing the temperature T, mass density ρ, gas pressure P, divergence of velocity field $\mathrm{div}(V)$, and velocity parallel (normal) to the magnetic field V_{p} (V_{n}) along a magnetic field line through the top of a chromospheric jet in the simulation of $T_{\mathrm{c}} = 2$ MK. The solid line indicates the location of plasma beta unity ($\beta = 1$). The dashed line represents the transition region ($T = 40$ kK).

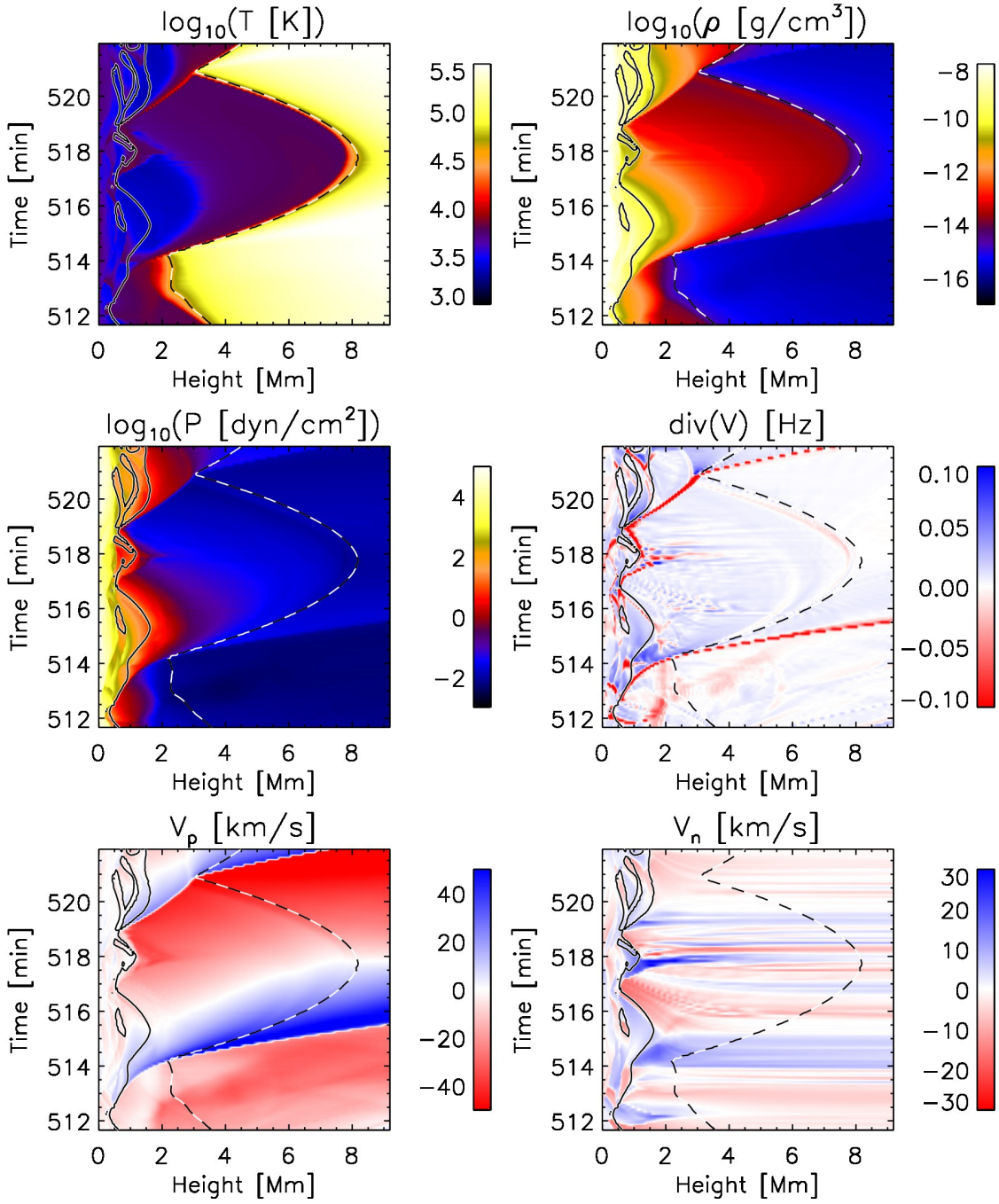

Figure 4.4: Same as Figure 4.3, but showing the case of a tall chromospheric jet in the simulation of $T_c = 0.4$ MK.

The transition region is lifted up by the shock wave (e.g., Hollweg, 1982) and follows parabolic trajectory. This process is essentially same as the previous one-dimensional numerical studies assuming the acoustic perturbations (e.g., Suematsu et al., 1982; Sterling et al., 1993). The chromospheric jet has a region with the small gas pressure than the surroundings near the transition region around the time of 533–536 min. The lack of the gas pressure is one of the reasons why the deceleration of this jets exceeds the gravitational acceleration of 274 m/s^2 at the solar surface (see also Section 4.6).

Another example of tall chromospheric jets in the $T_{\rm c} = 0.4$ MK case is shown in Figure 4.4. The parameters on the vertical motion of this jet are calculated as the maximum height of 8.2 Mm, maximum length of 6.0 Mm, lifetime of 405 s, maximum upward velocity of 59 km/s, and deceleration of 276 m/s^2. The jet is located at $X = 13.8$ Mm. The temporal evolution of the transition region through the shock-transition region interaction is essentially same as the previous example. We cannot find the significant decrease of the gas pressure as opposed to the previous one, which is consistent with the deceleration very close to the gravitational acceleration.

4.5 Statistical properties of chromospheric jets

The distribution of the parameters on the vertical motion of chromospheric jets is shown in Figure 4.5. The dependence of the scale of chromospheric jets on the coronal temperature are clearly identified. The lower coronal temperature produces taller, faster, longer living chromospheric jets. The deceleration for $T_{\rm c} = 2$ MK (blue solid line) and 1 MK (green dashed line) is distributed over a relatively broad range, exceeding the gravitational deceleration on the solar surface. The deceleration for $T_{\rm c} = 0.4$ MK (red dotted line) is concentrated below the gravitational deceleration.

The correlation among the derived parameters are shown in Figure 4.6. We find a clear correlation between maximum length and maximum upward velocity for all three simulations (panels (a)–(c)). The lifetime roughly correlates with the maximum velocity

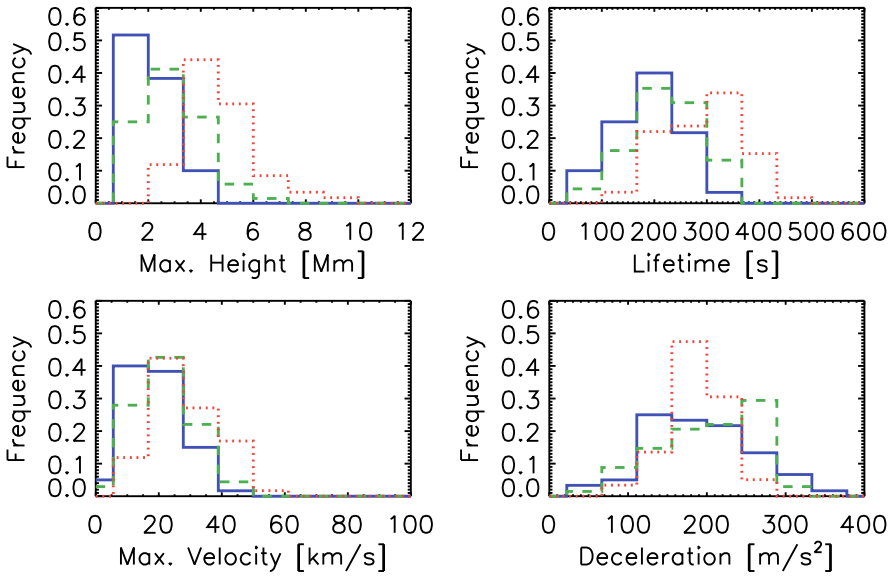

Figure 4.5: Histograms showing the maximum height (top left), lifetime(top right), maximum upward velocity (bottom left), and deceleration (bottom right) of chromospheric jets in the simulations of $T_{\rm c} = 2$ MK (blue solid lines), 1 MK (green dashed lines), and 0.4 MK (red dotted lines).

for each simulation (panels (d)–(f)). The lifetime becomes longer and the correlation between lifetime and maximum velocity becomes stronger when the coronal temperature is lower. The correlation between deceleration and maximum velocity is relatively weak (panels (g)–(i)).

The abovementioned dependence on the temperature at the top boundary, $T_{\rm c}$, can be explained as follows. When $T_{\rm c}$ is high (i.e., 2 MK) and the chromospheric jets are small, as in panels (a), (d), and (g) in Figure 4.6, the obtained correlations are consistent with the "shock deceleration hypothesis" suggested by Heggland et al. (2007). According to this hypothesis, the deceleration is determined by the periodicity of the slow-mode shock wave and can exceed the gravitational deceleration (see Eq. (1) in Heggland et al., 2007). The lifetime of the jet is determined by the period of the driving shock wave. The dotted lines in panels (a), (d), and (g) are the theoretical lines of parabolic motion with lifetimes of 2, 3, and 5 min. These lines are well consistent with the results from the simulation with $T_{\rm c} = 2$ MK. Because the lifetime of chromospheric jet is equal to the period of driving acoustic wave in the "shock deceleration hypothesis", the long lifetime in $T_{\rm c} =$

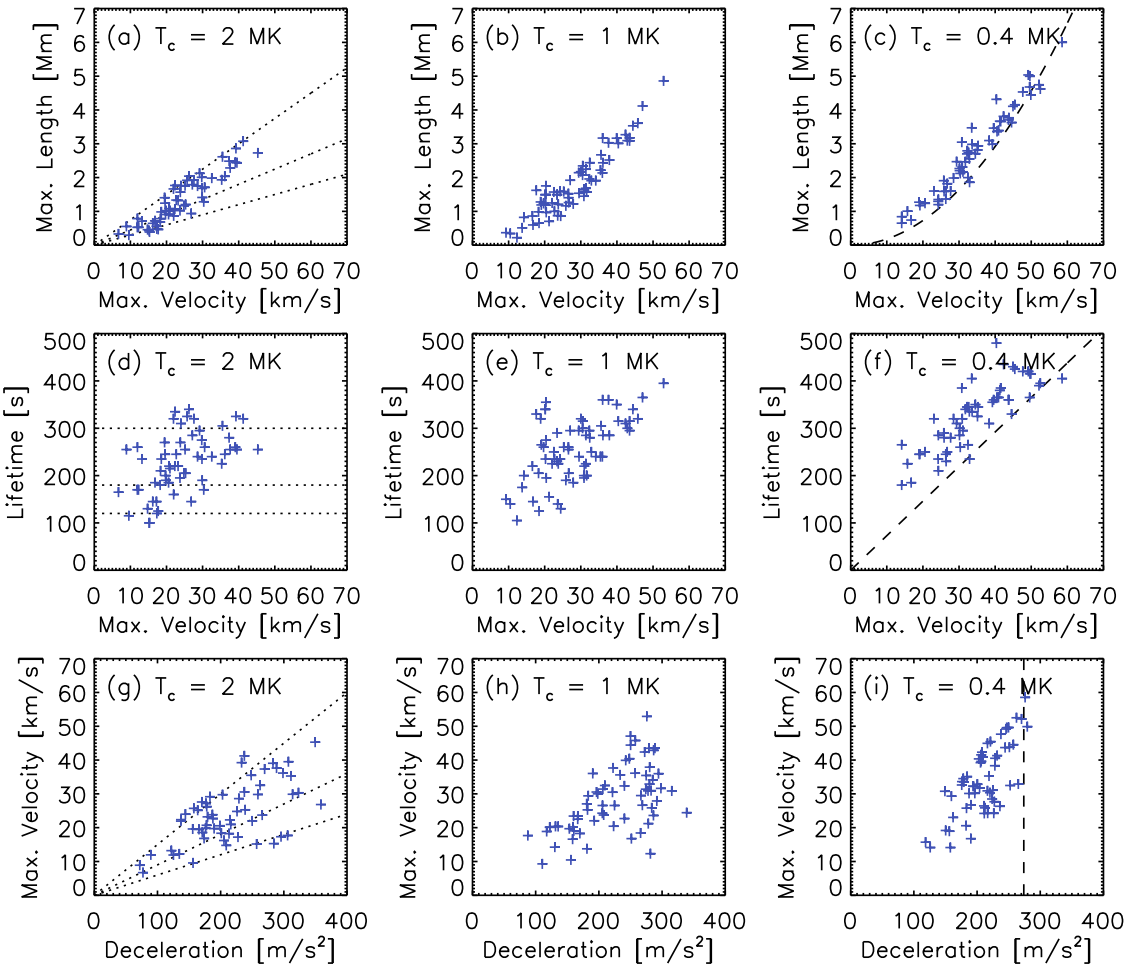

Figure 4.6: Statistical properties of the produced chromospheric jets in the three simulations with different temperatures at the top boundary, $T_{\rm c}$. Each cross sign corresponds to a chromospheric jet detected. See Section 4.5 for the description on the procedure for chromospheric jet detection. Panels (a), (d), and (g) correspond to $T_{\rm c} = 2$ MK, panels (b), (e), and (h) correspond to $T_{\rm c} = 1$ MK, and panels (c), (f), and (i) correspond to $T_{\rm c} = 0.4$ MK. The three dotted lines in panels (a), (d), and (g) represent the theoretical lines of parabolic motion with lifetimes of 2, 3, and 5 min. The dashed lines in panels (c), (f), and (i) indicate the theoretical lines of ballistic motion.

0.4 MK case (panels (f)) requires long period of driving waves, which is not expected under the short acoustic cutoff period in the lower solar atmosphere (e.g. Michalitsanos, 1973). The deceleration by the gravity becomes more important in this case. The resulting motion of taller chromospheric jets approaches free-fall. The dashed lines in panels (c), (f), and (i) indicate the theoretical lines of ballistic motion, which approximately explain the properties of simulated jets. Since the simulated jets in the case of $T_c = 0.4$ MK do not exactly follow ballistic paths, both of the gravitational and gas pressure gradient forces play a role in addition to the inclination of the magnetic field line. The case of $T_{\rm c} = 1$ MK, shown in panels (b), (e), and (h), exhibits intermediate properties between these two extremes.

4.6 Deceleration of chromospheric jets

To consider the abovementioned view on the determination of deceleration, we investigate the vertical force near the top of the chromospheric jets. The vertical component of the equation of motion can be written as follows.

$$
\begin{aligned}
-\frac{DV_z}{Dt} &= D_{\parallel}^G + D_{\parallel}^P + D_{\perp}^G + D_{\perp}^P + D_{\perp}^L \\
D_{\parallel}^G &= g_0 b_z^2 \\
D_{\parallel}^P &= \boldsymbol{b} \cdot \left(\frac{1}{\rho} \nabla P \right) b_z \\
D_{\perp}^G &= g_0 - D_{\parallel}^G = g_0 b_x^2 \\
D_{\perp}^P &= \frac{1}{\rho} \frac{\partial P}{\partial z} - D_{\parallel}^P \\
D_{\perp}^L &= -\frac{1}{\rho} \left(\boldsymbol{J} \times \boldsymbol{B} \right)_z
\end{aligned}
\tag{4.1}
$$

Here, g_0 is the gravitational acceleration at the solar surface, P is the gas pressure, $\boldsymbol{B}$ is the magnetic flux density, $\boldsymbol{J}$ is the current density, $D/Dt = \partial/\partial t + \boldsymbol{V} \cdot \nabla$ is the Lagrangian derivative, and $\boldsymbol{b} = \boldsymbol{B}/|\boldsymbol{B}|$ is a unit vector parallel to the magnetic field. If

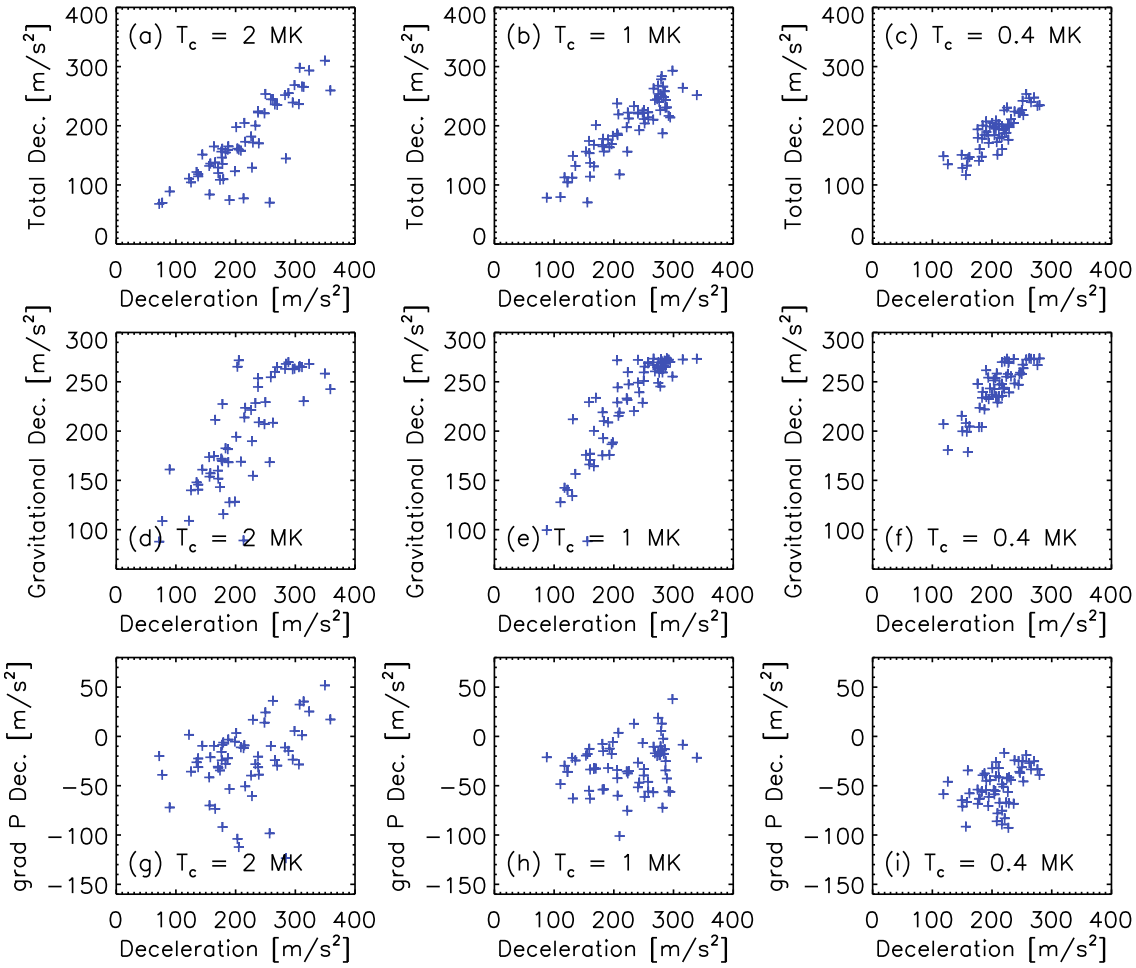

Figure 4.7: Contribution of gas pressure gradient and gravitational forces on the deceleration of the produced chromospheric jets in the three simulations with different temperatures at the top boundary, $T_{\rm c}$. Each cross sign corresponds to a chromospheric jet detected. Panels (a), (d), and (g) correspond to $T_{\rm c} = 2$ MK, panels (b), (e), and (h) correspond to $T_{\rm c} = 1$ MK, and panels (c), (f), and (i) correspond to $T_{\rm c} = 0.4$ MK. See Section 4.6 for the description on the definition of each variables.

we assume that the transition region at the top of the chromospheric jets is the contact discontinuity, the deceleration of the jets can be approximated by $-DV_z/Dt$ near the transition region. The result is shown in Figure 4.7. Panels (a)–(c) show the deceleration produced by the total force parallel to the magnetic field $D_{\parallel}^{P} + D_{\parallel}^{G}$ versus the deceleration calculated by the motion of the chromospheric jets. Although there is some level of dispersion, the motion of the transition region is roughly explained by the forces parallel to the magnetic field. The possible candidates of the discrepancy are the effect of the forces perpendicular to the magnetic field ($D_{\perp}^{G}$, $D_{\perp}^{P}$, and $D_{\perp}^{L}$), the deviation of the transition region from the contact discontinuity by the thermal conduction and waves, and the fitting and discretization errors. Panels (d)–(f) show the deceleration produced by the gravity parallel to the magnetic field $D_{\parallel}^{G}$. $D_{\parallel}^{G}$ is more concentrated near the value of gravitational acceleration in the lower coronal temperature. Because the structure of the magnetic field is nearly independent of the coronal temperature, the temperature dependence in these panels is caused by the difference of the height of produced jets. When the coronal temperature is higher, the maximum length of jets becomes small and the transition region moves near the root of the magnetic field where the magnetic field is more inclined. Panels (g)–(i) show the deceleration produced by the gas pressure gradient force parallel to the magnetic field $D_{\parallel}^{P}$. In $T_c = 0.4$ MK case, the pressure gradient force always decreases the deceleration of the jets. However, in $T_c = 2$ and 1 MK cases, a part of the jets is decelerated by the pressure gradient force. This is consistent with the "shock deceleration hypothesis" where the deceleration is determined by the periodic shock wave.

4.7 Amplification of shock waves in the chromosphere

To understand why the scale of the chromospheric jets depends on the coronal temperature, we investigate the relationship between the coronal gas pressure and the maximum velocity of the produced jets as shown in Figure 4.8. The scale height of the gas pressure in the corona is sufficiently long and the gas pressure is almost constant across the

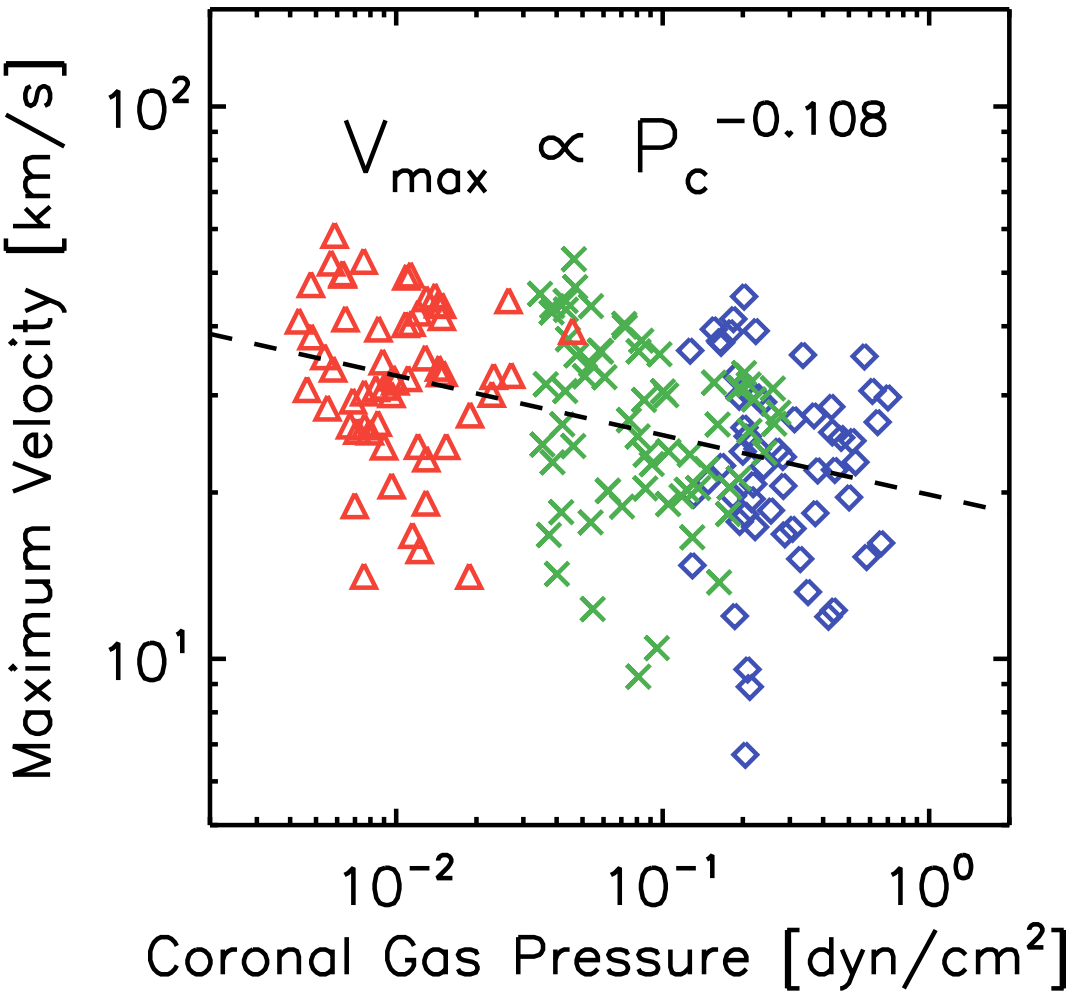

Figure 4.8: Dependence of the maximum upward velocity $V_{\rm max}$, of the chromospheric jets on the coronal gas pressure from the simulation of $T_{\rm c} = 2$ MK (shown as blue diamonds), $T_{\rm c} = 1$ MK (shown as green crosses), and $T_{\rm c} = 0.4$ MK (shown as red triangle). The coronal gas pressure, $P_{\rm c}$, is measured at the initial time of each chromospheric jet and averaged over the height range of 1–3 Mm above the transition region. The dashed line is the result of the least-square fitting, $V_{\rm max} \propto P_{\rm c}^{-0.108}$, assuming a power-law relation.

transition region. Thus, we can use the coronal gas pressure, $P_{\rm c}$, as the representative value of the gas pressure near the transition region. Shibata & Suematsu (1982) suggest that the density difference at the transition region causes the differences in the amplitude of the chromospheric shock wave and in the size of the chromospheric jets. For a linear wave, the energy flux of the slow magneto-acoustic wave is conserved during the propagation as $S\rho V^2 C_s = \text{constant}$. Here S is the cross-section of the magnetic flux tube, C_s is the speed of the slow magneto-acoustic wave, and V is the velocity parallel to the magnetic field. This relation is reduced to $V \propto (S\rho C_s)^{-1/2} \sim (SP_{\rm c})^{-1/2}$. The dependence on S does not appear in our current results because the magnetic field structure is almost the same in each of our three simulations. In fact, the shock wave is strong in the upper chromosphere, and the energy dissipation near the shock front violates the energy flux conservation. Ôno et al. (1960) analytically derived the relation of $V \propto P_{\rm c}^{-0.236}$ for a strong shock wave with the constant chromospheric temperature and an adiabatic heat ratio of $5/3$. Shibata & Suematsu (1982) reported the relation of $V \propto P_{\rm c}^{-0.23}$ in their one-dimensional adiabatic hydrodynamic simulation, which is very close to the analytic estimate for strong shock wave. We obtain the relation of $V \propto P_{\rm c}^{-0.108}$ from the three simulations with different coronal temperatures. This result indicates that another energy-loss process contributes to the formation of chromospheric jets in our simulations, like the radiative energy loss. We note that the amplitude of the maximum upward velocity depends only on the nonlinear propagation of acoustic waves in the photosphere and chromosphere and does not depend on the deceleration models discussed in the preceding section.

Figure 4.9 shows the relation between the coronal gas pressure and other parameters of the vertical motion of chromospheric jets. As can be seen from panel (c), the dependence of the deceleration is weak. We can only observe that the dispersion of the deceleration is larger when the coronal gas pressure is high. If we assume that the average deceleration does not depend on the coronal gas pressure, the power law indices of the maximum length (panel (a)) and lifetime (panel (b)) can be explained from the index of the maximum

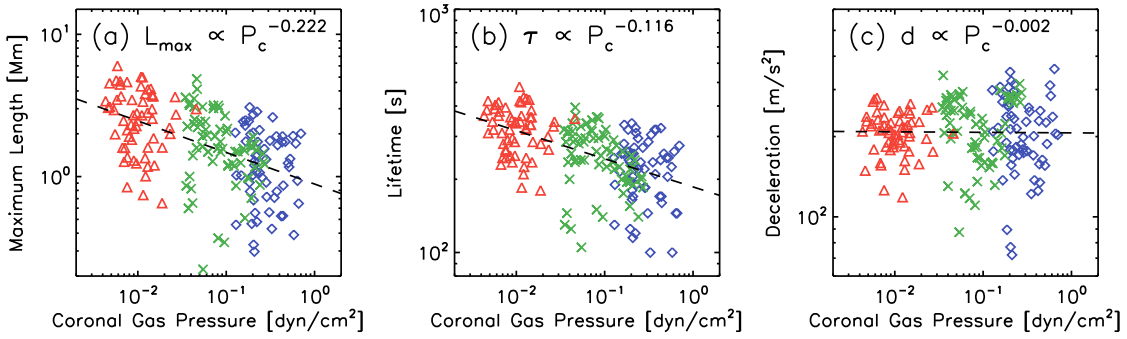

Figure 4.9: Dependence of (a) maximum length $L_{\rm max}$, (b) lifetime τ, and (c) deceleration d of the chromospheric jets on the coronal gas pressure from the simulation of $T_{\rm c} = 2$ MK (shown as blue diamonds), $T_{\rm c} = 1$ MK (shown as green crosses), and $T_{\rm c} = 0.4$ MK (shown as red triangle). The coronal gas pressure, $P_{\rm c}$, is measured at the initial time of each chromospheric jet and averaged over the height range of 1–3 Mm above the transition region. The dashed lines are the least-square fittings assuming a power-law relation.

velocity using the relations $L_{\rm max} = V_{\rm max}^2/(2d)$ and $\tau = 2V_{\rm max}/d$.

The power law index of around -0.1 of the maximum velocity (Figure 4.8) is also observed in the propagation of longitudinal waves in the chromosphere as shown in Figure 4.10. The velocity parallel to the magnetic field line seems to follow the relation of $V_{\rm p} \propto \rho^{-0.1}$ over the mass density of 10^{-13}–10^{-10} g/cm^3. The joint probability density functions between the field-aligned velocity and the mass density in the three different simulations share almost the same profiles below the transition region. The only difference appears on the density of the transition region (around 10^{-14} g/cm^3 in Figure 4.10). This result is consistent with the dependence of the maximum velocity of chromospheric jets on the coronal gas pressure in Figure 4.8. We note that the plasma beta is low in the region with this density range. Because the dispersion of slow-mode shock waves should be small in the low-beta plasma, the deviation from the power law index of -0.236 (Ôno et al., 1960) in Figures 4.8 and 4.10 seems to be not associated with the multidimensional effect. The possible candidates of the energy-loss process for chromospheric shock waves are the radiative energy loss, the thermal conduction, and the latent heat of ionization. The dynamic variation of the chromospheric temperature will also affect the result.

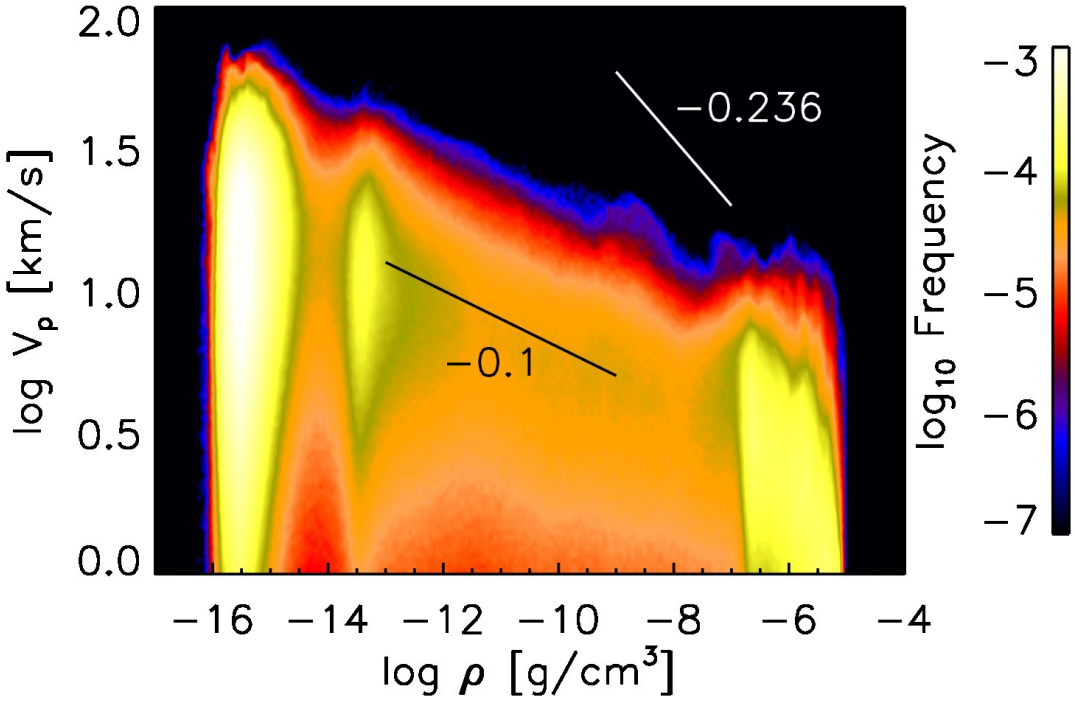

Figure 4.10: Joint probability density function of the velocity parallel to the magnetic field $V_{\rm p}$ against the mass density ρ in the simulation of $T_{\rm c} = 0.4$ MK. The color-coding indicates the logarithm of the frequency. The black and white lines represent the power law relation of $V_{\rm p} \propto \rho^{-0.1}$ and $V_{\rm p} \propto \rho^{-0.236}$, respectively. Note that the power law index of -0.1 is shown only for the comparison with the index in Figure 4.8 and not derived from the fitting.

4.8 Discussion

We can compare our three simulations with different temperatures at the top boundary ($T_{\rm c} = 2, 1$, and 0.4 MK) to the observations of the active region dynamic fibrils, the quiet region spicules, and the coronal hole spicules, respectively. Panels (a), (d), and (g) in Figure 4.6 show behavior similar to the observation of the active region dynamic fibrils by De Pontieu et al. (2007a). The properties of the spicules in quiet regions and coronal holes were investigated by Zhang et al. (2012) and Pereira et al. (2012). Both studies reported that the spicules became longer in the coronal hole and shorter in the quiet region, which was consistent with our results. We note that the parabolic trajectory of jets in our study are consistent with the type I spicules but inconsistent with the type II spicules, which exhibit linear trajectory. Because the top of the spicule was considerably affected by the observed wavelength (Pereira et al., 2014; Skogsrud et al., 2015), further studies are required for the more quantitative comparison. We also note that $T_c = 0.4$ MK is too low for coronal holes and $T_c = 2$ MK is also too low for active regions. The regional difference of density and the spatial inhomogeneity of temperature and density will explain at least a part of this discrepancy. The magnetic field strength is also not the typical value for these regions. However, if the chromospheric jets are driven by the acoustic waves from the lower atmosphere, we expect that the magnetic field does not affect the scale of the jets strongly.

The numerical setting of the two-dimensional simulation by Heggland et al. (2011) was very similar to that in our study. The simulation with $T_{\rm c} = 1$ MK is consistent with Case B in their study. Their simulation employed the Bifrost code (Gudiksen et al., 2011) with more sophisticated treatment of radiation. This agreement supports the validity of our simulations. Martínez-Sykora et al. (2009) investigated the chromospheric jets in three-dimensional domain with the emerging magnetic flux. The typical length of their jets was approximately 1 Mm. The high coronal temperature produced by the energy release of the flux emergence, in addition to the rapid expansion of the magnetic field

lines in the corona, is a possible explanation for why these jets were small.

We note that a part of the transverse waves are reflected from the corona (Figures 4.3 and 4.4). The top boundary condition of the vertical magnetic field is the main reason of this reflection. We confirm that the vertical motion of the chromospheric jets is not sensitive to the top boundary condition for the magnetic field. More delicate treatment of boundary conditions is necessary for the analysis on the transverse motion of chromospheric jets. The dependence on the grid size is also investigated by doubling the numerical resolution, and we find the similar dependence on the coronal temperature of the chromospheric jet motion. We find that the widths of the simulated jets are strongly affected by the numerical resolution. Further research should be undertaken to investigate on the horizontal structure of jets.

Chapter 5

Two-dimensional simulation of solar chromospheric jets: role of the magnetic field

5.1 Introduction

In the solar chromosphere, the average strength of the magnetic field varies significantly depending on the region observed. The magnetic field in active regions is usually several times stronger than in quiet regions and coronal holes. Heggland et al. (2011) investigated the effect of magnetic field strength and inclination on the chromospheric jets using the two-dimensional simulations with the sophisticated modeling of convective motion, but they did not provides the statistical comparison with different magnetic field strengths.

The chromospheric jets in quiet regions like mottles (Suematsu et al., 1995), Rapid Blue-shifted Excursions (Langangen et al., 2008b), and network jets (Tian et al., 2014) are observed mainly along the magnetic network. On the other hand, in the previous chapter (Iijima & Yokoyama, 2015), chromospheric jets tend to be elongated in the region with weak magnetic field. Heggland et al. (2011) also reported the similar results in their two-dimensional simulations. Two possible candidates were suggested to explain

this behavior. The first was that the multidimensional interaction of acoustic waves is more frequent in the weakly magnetized regions. The second was that the magnetic field expansion from the photosphere to the corona reduces the amplitude of acoustic waves. As pointed out by Shibata & Suematsu (1982) and previous chapter (Iijima & Yokoyama, 2015), the temperature and density of corona is also important for the scale of chromospheric jets. The effect of the magnetic field should be distinguished from the contribution of the coronal condition to clarify the dependence on the local magnetic field structure. In this study, the effects of the magnetic field on chromospheric jets, especially the dependence on the average magnetic field strength and local magnetic field structure, are investigated.

5.2 Simulation setup

The basic equations, numerical methods, grid and domain size, and initial and boundary conditions are essentially same as in the previous chapter. We analyze two new simulations with the different magnetic field strengths in Section 5.3 and one simulation from the previous chapter in Section 5.4. The two simulations in Section 5.3 has the temperature at the top boundary of $T_{\rm c} = 1$ MK and the average vertical magnetic field strength of $B_0 = 10$ and 100 G. The simulation described in Section 5.4 has the temperature at the top boundary of $T_{\rm c} = 0.4$ MK and the average vertical magnetic field strength of $B_0 =$ 30 G. This parameter is chosen because chromospheric jets in this simulation are tall so that the dependence on the local magnetic field structure can be easily identified.

5.3 Dependence on the average magnetic field strength

In this section, we focus on the effect of the initial magnetic field strength B_0 on the properties of chromospheric jets using the two simulations with the strong ($B_0 = 100$ G) and moderate ($B_0 = 10$ G) field strength. We fix the coronal temperature of $T_{\rm c} = 1$ MK

to focus on the effect of the magnetic field strength.

5.3.1 Morphology

Figure 5.1 presents the snapshot of the temperature and mass density of the two simulations with the coronal temperature of $T_{\rm c} = 1$ MK and average magnetic field strength of $B_0 = 100$ and 10 G. The $B_0 = 100$ G case has several strong magnetic field concentrations near $X = 3$, 5, and 15 Mm. On the other hand, the $B_0 = 10$ G case has the complicated magnetic field structure in the photosphere and does not have any kilogauss magnetic field concentrations. The chromospheric jets in the $B_0 = 100$ G case is more inclined than in the $B_0 = 10$ G case. The height of the transition region tend to be low near the center of the magnetic field concentrations in the $B_0 = 100$ G case, which is consistent with the simulations in the previous chapter and Heggland et al. (2011).

5.3.2 Statistical properties of chromospheric jets

Figure 5.2 shows the statistical properties of simulated jets in the two simulations. The distributions of the maximum height, lifetime, and maximum upward velocity are very similar in both cases. The difference appears in the deceleration of jets. The $B_0 = 100$ G case has a broader distribution of the deceleration. The deceleration of the $B_0 = 10$ G case is more concentrated near the solar gravity at 274 m/s^2. This difference is interpreted as the result of the inclined magnetic field in the $B_0 = 100$ G case. The deceleration in both cases sometimes exceeds the solar gravitational acceleration, which suggests the existence of the "shock deceleration" process (Heggland et al., 2007; Iijima & Yokoyama, 2015).

Figure 5.3 compares the correlation between the two of the maximum length, lifetime, maximum velocity, and deceleration of simulated jets. No significant difference is found in the correlation between the maximum length and maximum velocity (panels (a) and (b)). The lifetime in the $B_0 = 100$ G case is slightly larger than in the $B_0 = 10$ G case

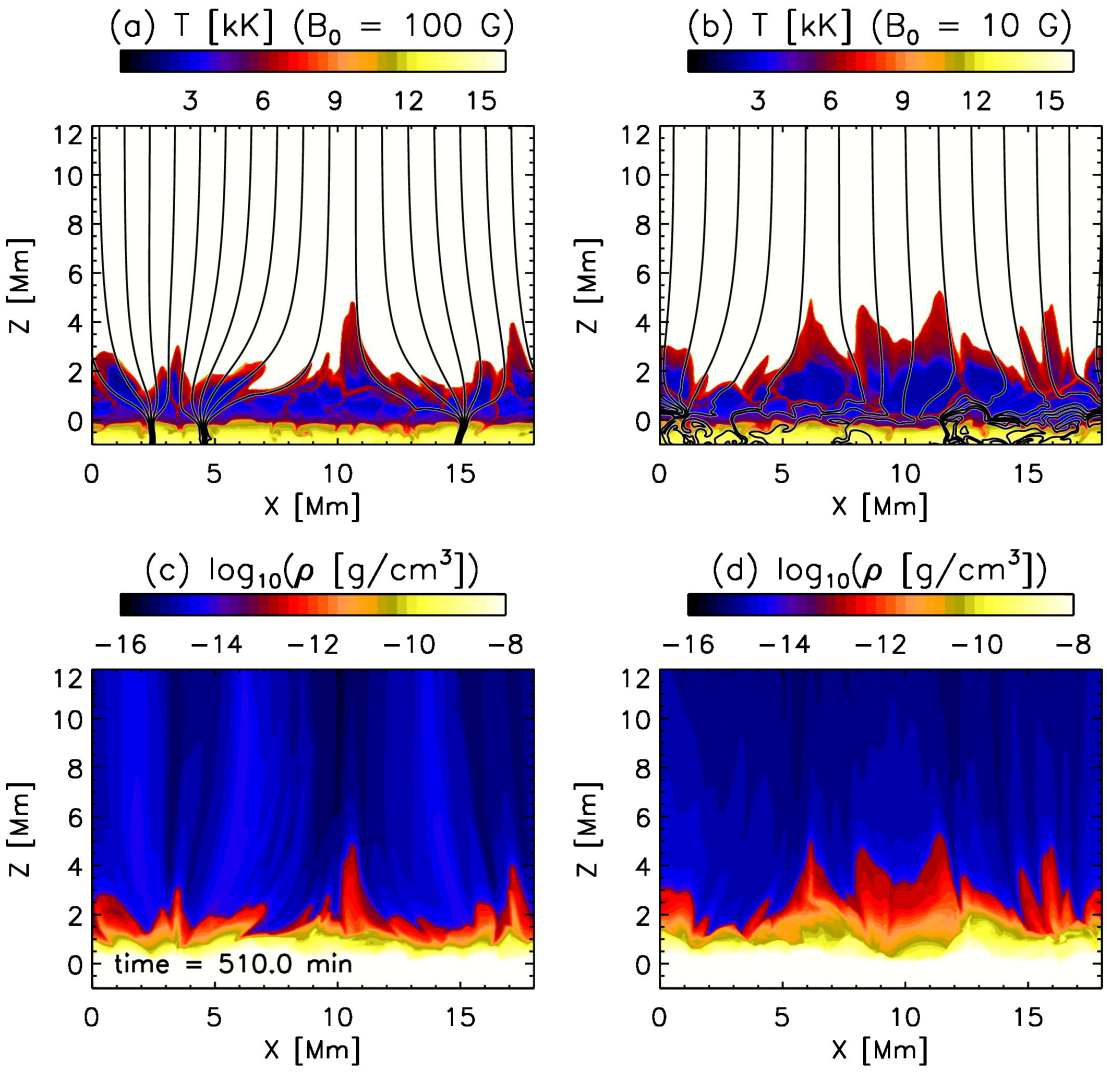

Figure 5.1: Snapshots from the two simulations with the different initial magnetic field strength, B_0. Panels (a) and (b) show the temperature, and panels (c) and (d) represent the logarithm of mass density. The solid lines in panels (a) and (c) indicate the magnetic field lines. Panels (a) and (c) correspond to the simulation with $B_0 = 100$ G and panels (b) and (d) correspond to the simulation with $B_0 = 10$ G.

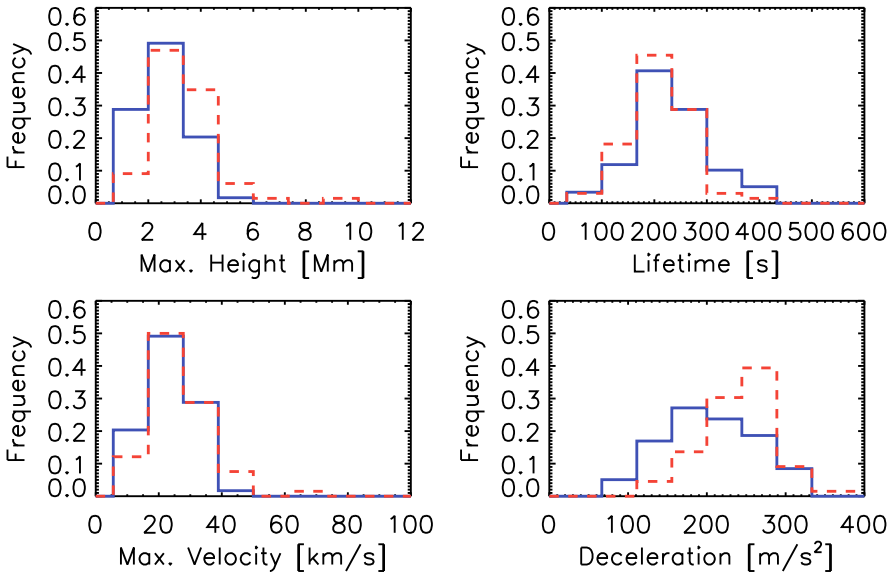

Figure 5.2: Histograms showing the maximum height (top left), lifetime(top right), maximum upward velocity (bottom left), and deceleration (bottom right) of chromospheric jets in the simulations of $B_0 = 100$ G (blue solid lines) and 10 G (red dashed lines).

comparing for the same maximum velocity in panels (c) and (d). The broader distribution of the deceleration in the $B_0 = 100$ G case causes the longer lifetime in the same velocity than the $B_0 = 10$ G case (panels (e) and (f)).

5.3.3 Deceleration of chromospheric jets

Figure 5.4 shows the contribution of the gas pressure gradient and gravitational forces on the deceleration of simulated jets. The distribution of the gravitational force indicates that the inclination of the magnetic field effectively reduces the deceleration in the $B_0 = 100$ G case, which is consistent with the results in Figures 5.2 and 5.3. The gas pressure gradient force sometimes decelerate the jets in both cases, which is similar to the $T_c = 2$ and 1 MK cases with $B_0 = 30$ G in the previous chapter (Iijima & Yokoyama, 2015). The results suggest that the "shock deceleration" process affects the deceleration of a part of simulated jets.

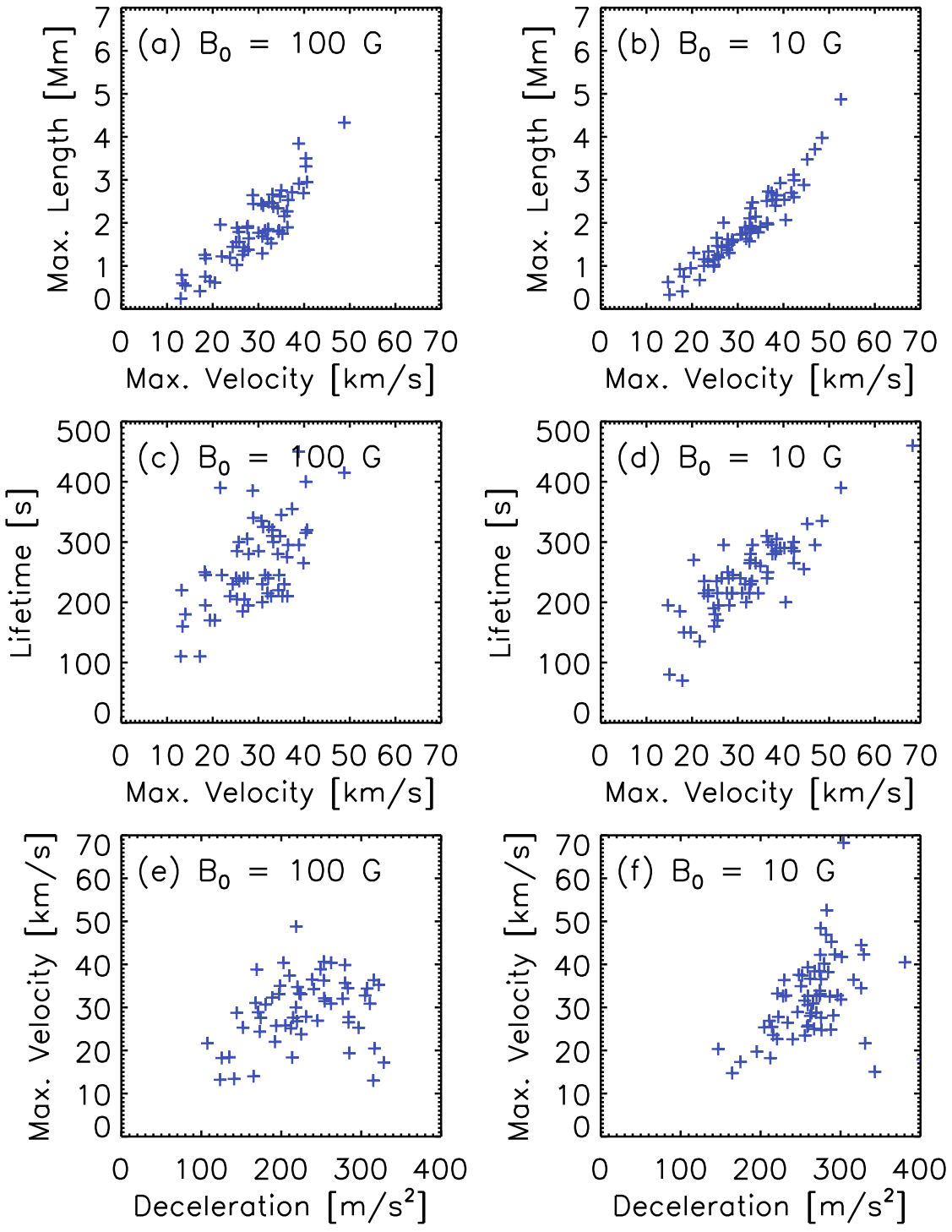

Figure 5.3: Statistical properties of the produced chromospheric jets in the three simulations with different temperatures at the top boundary, T_c. Each cross sign corresponds to a chromospheric jet detected. Panels (a), (c), and (e) correspond to $B_0 = 100$ G and panels (b), (d), and (f) correspond to $B_0 = 10$ G.

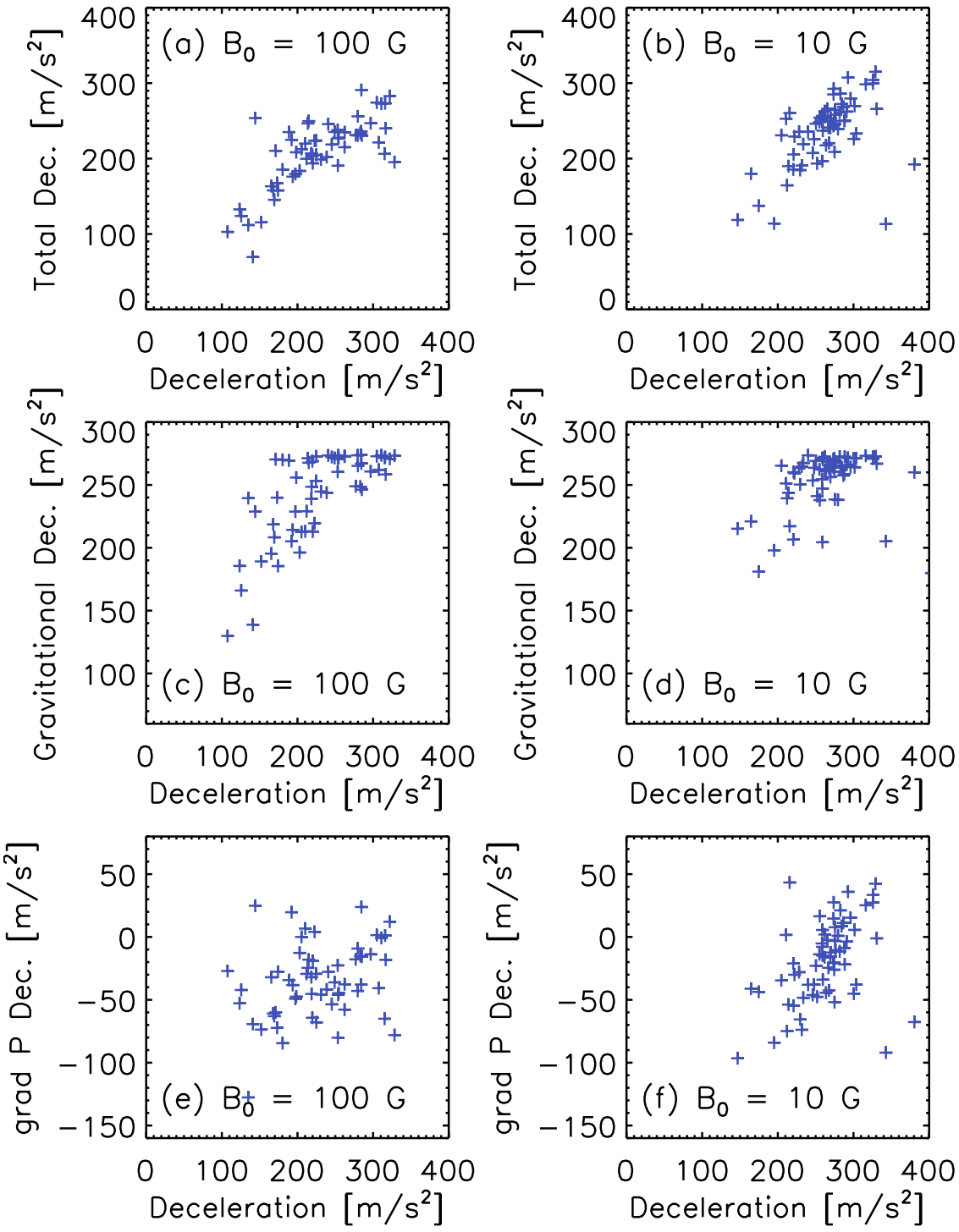

Figure 5.4: Contribution of gas pressure gradient and gravitational forces on the deceleration of the produced chromospheric jets in the two simulations with different initial magnetic field strength B_0. Panels (a), (c), and (e) correspond to $B_0 = 100$ G and panels (b), (d), and (f) correspond to $B_0 = 10$ G.

5.4 Dependence on the local magnetic field structure

In this section, we investigate the dependence on the local structure of the magnetic field, especially the strength of the photospheric magnetic field, on chromospheric jets using the simulation with the initial magnetic field strength of $B_0 = 30$ G and coronal temperature of $T_c = 0.4$ MK. These parameters are chosen because of the variety of both the structure of the magnetic field and scale of simulated jets in this simulation.

5.4.1 Structure of atmosphere

Figure 5.5 shows the time-distance plots at the height of transition region, defined as the tallest position with $T = 40$ kK. The strong vertical component of the magnetic field at the transition region (panel (d)) roughly indicates that the magnetic field line is connected to the kilogauss magnetic field concentration near $X = 3$ Mm in the photospheric level. The height of the transition region (panel (a)) clearly anti-correlates with the magnetic field strength, which indicates that the transition region tends to be low inside the magnetic flux tube (the strong concentration of the magnetic field). We note that the strong elevation of the transition region around the time of 530 min. As described in the following section, this is caused by the collision of two nearby magnetic flux tubes at the time of about 525 min near $X = 3$ Mm in the photosphere. The gas pressure shown in panel (b) shows the correlation with the vertical magnetic field strength. This correlation affects to enhance the anti-correlation between the transition region height and magnetic field strength in Figure 5.5(a).

The correlation between the field-aligned velocity (Figure 5.5(c)) and magnetic field strength (Figure 5.5(d)) is shown in Figure 5.6. The positive field-aligned velocity corresponds to the upward motion. The absolute velocity is clearly larger when the magnetic field is weaker. This result indicates that the velocity is weaker above the stronger photospheric magnetic field. This is consistent with the anti-correlation between the transition region height and magnetic field strength in Figure 5.5(a) since the height is naturally

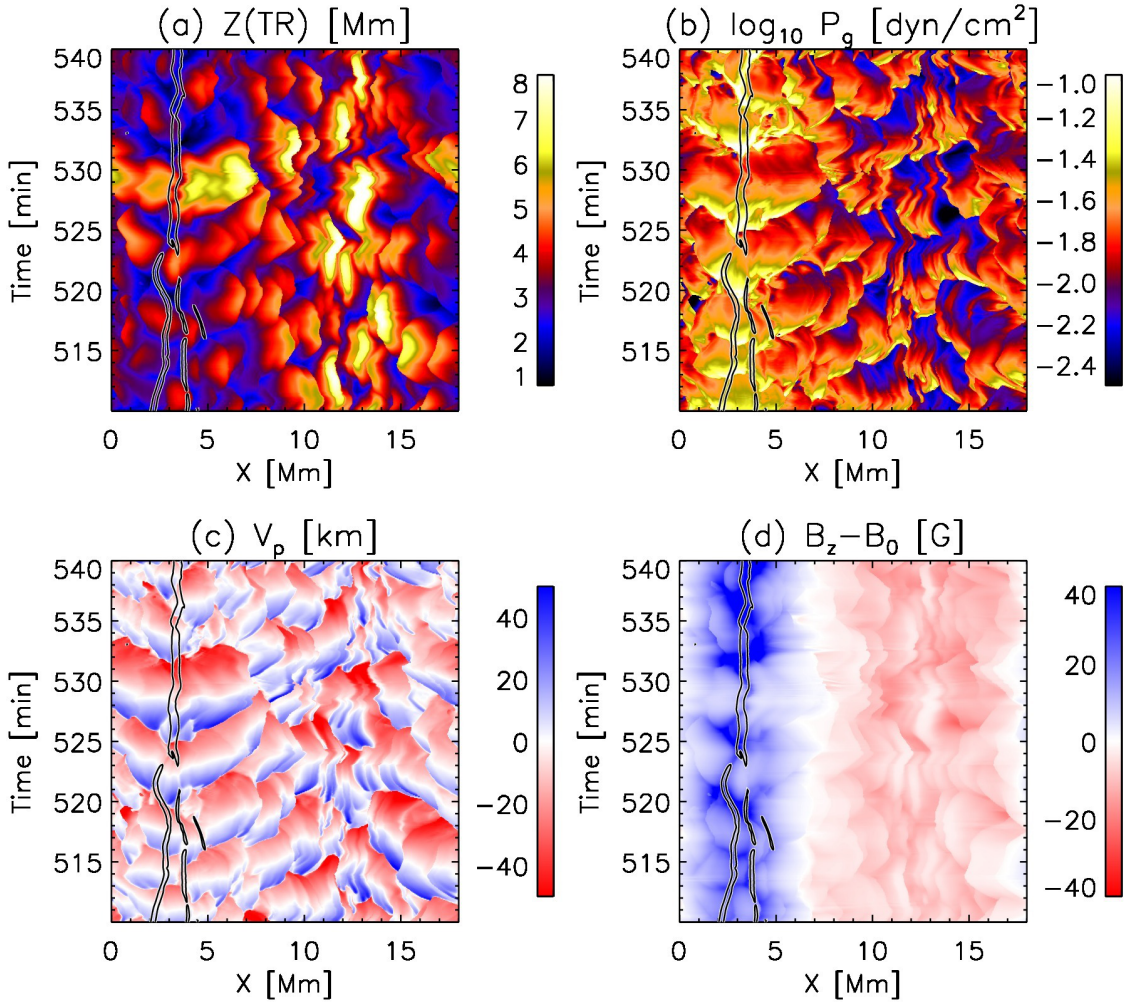

Figure 5.5: Time-distance plots at the height of transition region showing (a) the height of the transition region $Z(\mathrm{TR})$, (b) logarithm of gas pressure P_g, (c) velocity parallel to the magnetic field V_p, and (d) vertical magnetic field B_z subtracted by the initial magnetic field strength B_0 G. The solid line indicates the contour of the vertical magnetic field strength of 500 G at the surface ($Z = 0$ Mm). The results for the simulation with $B_0 = 30$ G and $T_c = 0.4$ MK are shown.

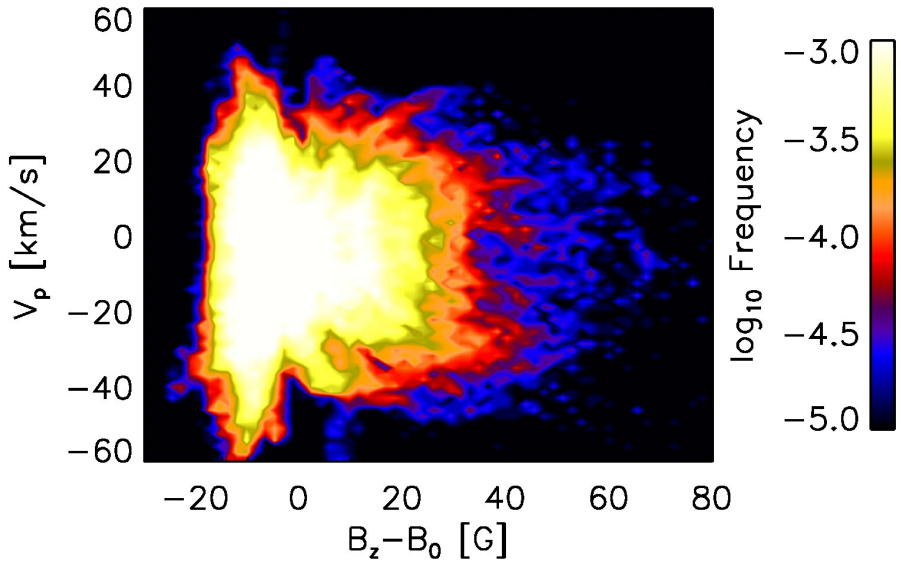

Figure 5.6: Joint probability density function of the velocity parallel to the magnetic field $V_{\rm p}$ against the vertical component of the magnetic field strength B_z subtracting the initial magnetic field strength B_0 in Figure 5.5(c). The results for the simulation with $B_0 = 30$ G and $T_{\rm c} = 0.4$ MK are shown.

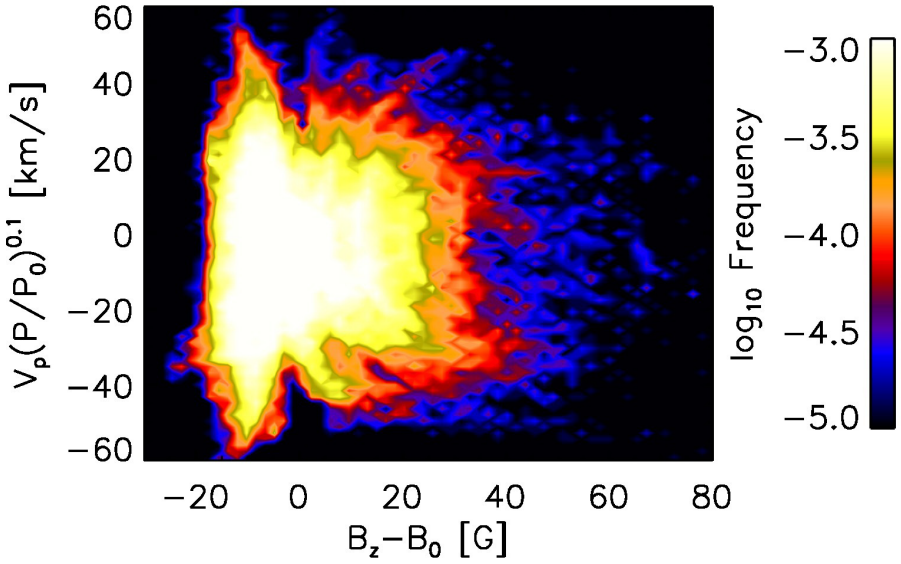

Figure 5.7: Same as Figure 5.6, but showing the velocity parallel to the magnetic field corrected for the contribution of the gas pressure $V_{\rm p}(P/P_0)^{0.1}$. The reference coronal gas pressure P_0 is taken to be 0.01 dyn/cm^2.

larger with a larger velocity. This dependence of the velocity field is also affected by the dependence of gas pressure. We remove the contribution from the distribution of gas pressure by assuming that the shock wave propagates the stratified chromosphere satisfying the relation $V_p \propto P^{-0.1}$ as shown in Figure 5.7. This relation is taken from the previous chapter (Iijima & Yokoyama, 2015). The longitudinal component of the velocity field shows the anti-correlation with the magnetic field strength even when the contribution from the coronal gas pressure is removed. The result indicates that the shock waves driven in the photosphere and lower chromosphere is weak inside the strong magnetic flux tube.

Figure 5.8 shows the time-distance plots at the isodensity height of $\rho = 10^{-12}$ g/cm^3. The height of the isodensity tends to be lower in the magnetic flux tube than in the surroundings as in Figure 5.8(a). In other words, the mass density is lower inside the flux tube when it is compared at the same height. This is a natural consequence if the horizontal total (gas plus magnetic) pressure balance is accounted. No significant difference of the temperature between inside and outside of the flux tube is found (Figure 5.8(b)).

Figure 5.9 presents the dependence of the field-aligned velocity field on the magnetic field strength at the isodensity height of $\rho = 10^{-12}$ g/cm^3. The velocity parallel to the magnetic field shows anti-correlation with the magnetic field strength. The result again indicates that the acoustic perturbation inside the flux tube is weaker than in the surroundings.

5.4.2 Relation between chromospheric jets and the magnetic field at the photosphere

Figure 5.10 shows the dependence of the properties of chromospheric jets on the photospheric magnetic field strength. If we focus on the jets not produced in the time range of 525–535 min (shown as blue diamonds), the chromospheric jets tend to be taller with the weaker photospheric magnetic field. A part (not all) of jets in the time range of 525–535

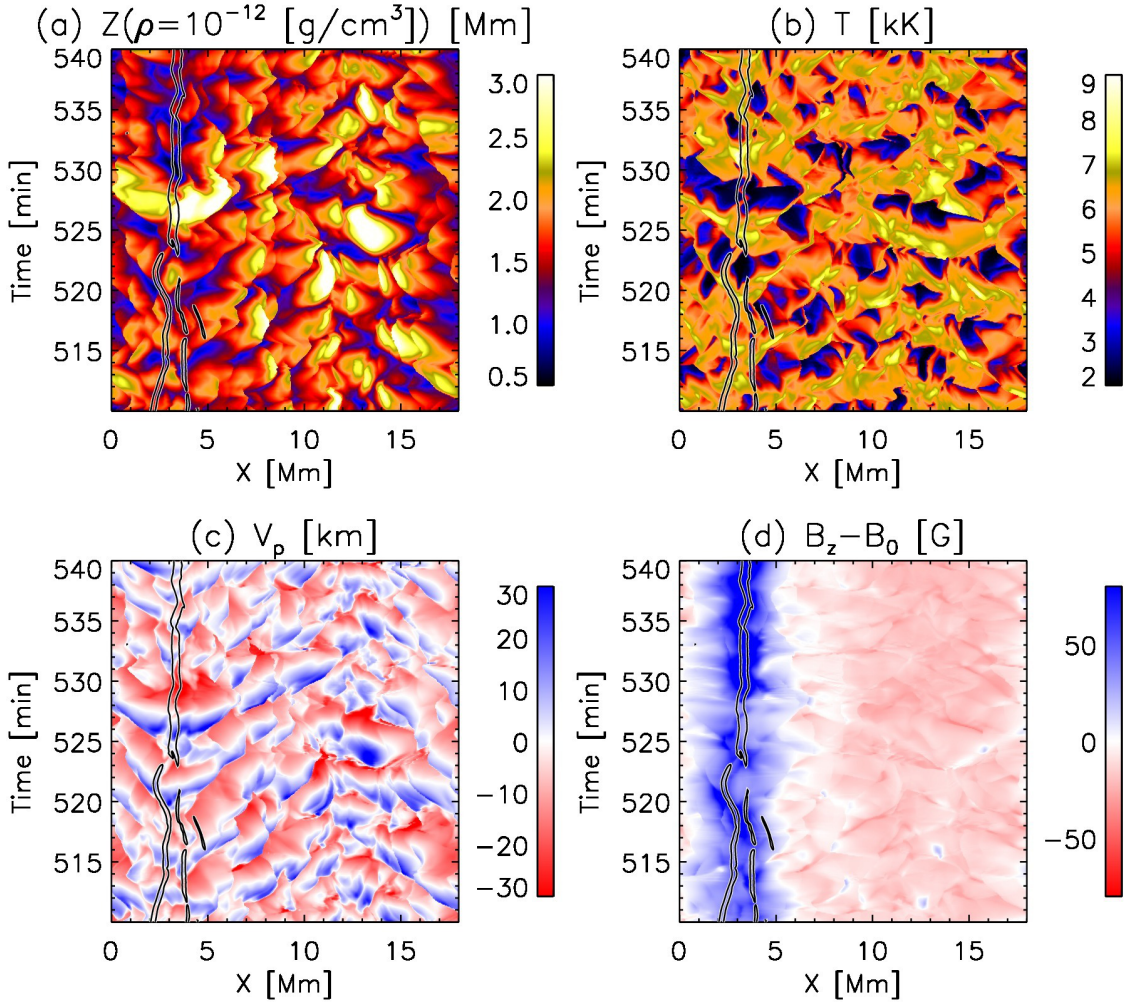

Figure 5.8: Time-distance plots at the height where the mass density equals to 10^{-12} g/cm^3. Shown are (a) the height of isodensity $Z(\rho = 10^{-12}$ [g/cm^3]), (b) gas temperature T, (c) velocity parallel to the magnetic field V_p, and (d) difference of the vertical component of the magnetic field B_z and initial magnetic field strength B_0. The solid line indicates the contour of the vertical magnetic field strength of 500 G at the surface ($Z = 0$ Mm). The results for the simulation with $B_0 = 30$ G and $T_c = 0.4$ MK are shown.

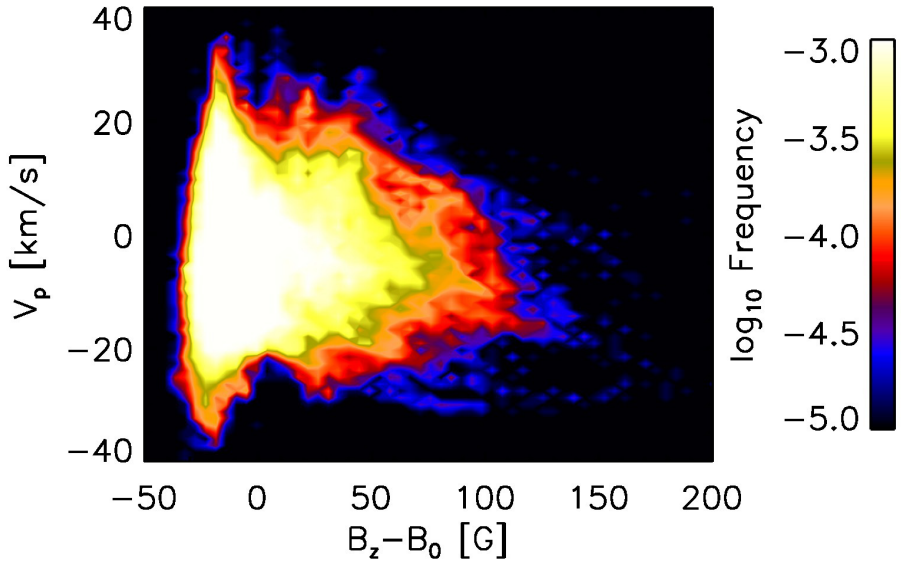

Figure 5.9: Joint probability density function of the velocity parallel to the magnetic field $V_{\rm p}$ against the vertical component of the magnetic field strength B_z subtracting the initial magnetic field strength B_0 in Figure 5.8(c). The results for the simulation with $B_0 = 30$ G and $T_{\rm c} = 0.4$ MK are shown.

min (shown as red crosses) are produced by the collision of nearby magnetic flux tubes at the time of 525 min. This process is described in Section 5.4.3.

The difference of coronal gas pressure $P_{\rm c}$ contributes to the scale of chromospheric jets (Shibata & Suematsu, 1982; Iijima & Yokoyama, 2015). By using the power law relations of $V_{\rm max} \propto P_{\rm c}^{-0.1}$, $L_{\rm max} \propto P_{\rm c}^{-0.2}$, and $\tau \propto P_{\rm c}^{-0.1}$ obtained in the previous chapter (Iijima & Yokoyama, 2015), the contribution from the distribution of coronal gas pressure is removed. The result is shown in Figure 5.11. The dependence on the photospheric magnetic field strength becomes weaker but still remains. The strength of acoustic waves as the driver of chromospheric jets is weaker inside the magnetic flux tube even if the contribution of the coronal gas pressure is accounted.

5.4.3 Generation and propagation of acoustic waves: typical cases

We introduce four examples of the excitation and propagation of acoustic waves in the photosphere to understand the mechanisms in the magnetic flux tube and the surrounding

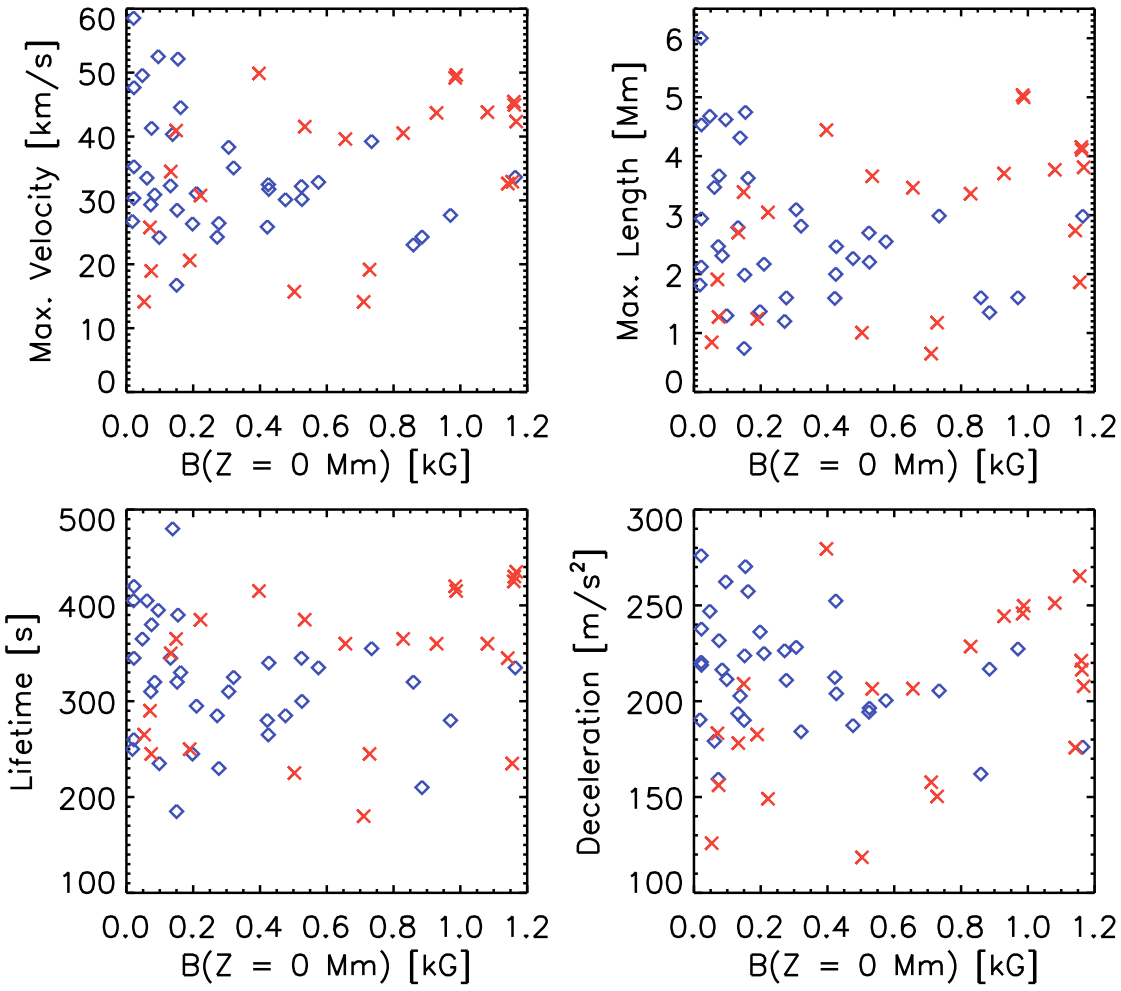

Figure 5.10: Dependence of the maximum upward velocity (top left), maximum length (top right), lifetime (bottom left), and deceleration (bottom right) of simulated chromospheric jets on the magnetic field strength observed at the height of $Z = 0$ Mm. The red crosses represent the jets in the time range of 525–535 min. The blue diamonds indicate other jets. The results for the simulation with $B_0 = 30$ G and $T_c = 0.4$ MK are shown.

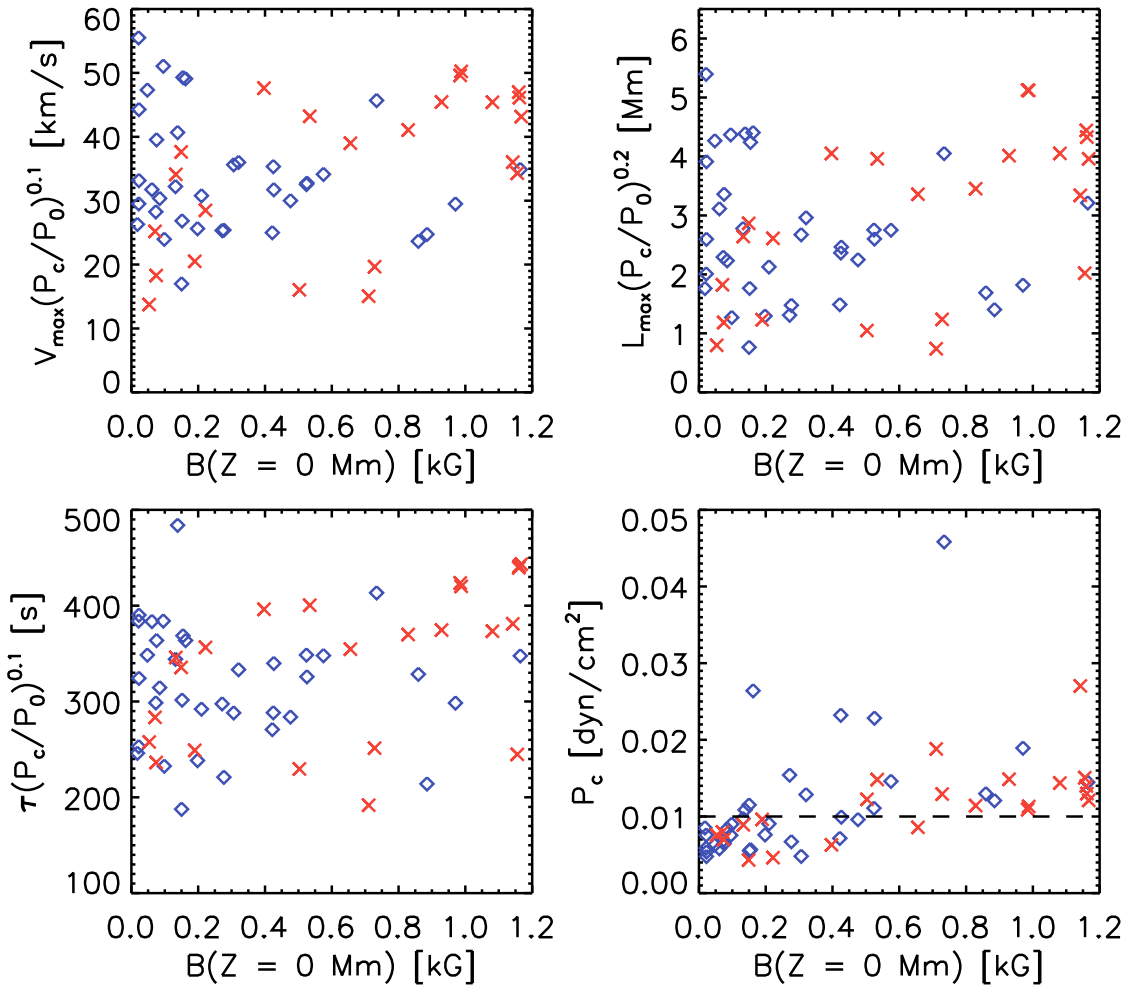

Figure 5.11: Dependence of the maximum upward velocity $V_{\rm max}$ (top left), maximum length $L_{\rm max}$ (top right), lifetime τ (bottom left), and coronal gas pressure $P_{\rm c}$ (bottom right) of simulated chromospheric jets on the magnetic field strength observed at the height of $Z = 0$ Mm. The maximum velocity, maximum length, and lifetime is corrected to the reference coronal gas pressure $P_0 = 0.01$ dyn/cm^2 using the relations $V_{\rm max} \propto P_{\rm c}^{-0.1}$, $L_{\rm max} \propto P_{\rm c}^{-0.2}$, and $\tau \propto P_{\rm c}^{-0.1}$. The red crosses represent the jets in the time range of 525–535 min. The blue diamonds indicate other jets. The results for the simulation with $B_0 = 30$ G and $T_{\rm c} = 0.4$ MK are shown.

region.

Figure 5.12 shows the excitation of acoustic waves by the collision of two nearby magnetic flux concentrations at the time of 525 min. The negative divergence of the velocity field is a good indicator of the shock front. The two nearby magnetic flux concentrations located at $X = 2$ and 4 at time $= 522.0$ min (top left panel) produce the compression between the flux tubes at $X = 3$ Mm (top right panel). The compression produces the fan-shaped shock wave propagating upward inside the collided flux tube (bottom left panel). The shock wave hits the transition region at time $= 525.0$ min in bottom right panel. The strong elevation of the transition region in the flux tube at the time of 530 min in Figure 5.5(a) and a part of chromospheric jets shown as the red crosses in Figure 5.10 is caused by this process. This process is the possible candidate to produce tall jets inside the strong flux tube at least in the two-dimensional simulations.

Figure 5.13 shows the excitation process of acoustic waves in the independent magnetic flux tube. The acoustic waves are generated in the magnetic flux concentration at $X = 3.5$ Mm by the surrounding photospheric convection motion (top panels). The fan-shaped shock wave propagates upward (bottom left panel) and hits the transition region at time $= 537.0$ min (bottom right panel). The acoustic waves excited inside the flux tube spread over by the expansion of flux tube and reduce their amplitude. We also note that the low density inside the magnetic flux tube produces the small density contrast between the chromosphere and transition region. This also contributes to reduce the amplification of shock waves and produce shorter chromospheric jets in the flux tube.

Figure 5.14 presents the interaction of the high-beta shock waves and low-beta magnetic flux tube. The acoustic waves are first generated by the convective motion around $X =$ 4–6 Mm outside the magnetic flux concentration located at $X = 3.5$ Mm (top left panel). The high-beta acoustic waves propagate upward hit the edge of the magnetic flux tube around the height of 1 Mm, elevating the plasma-beta unity line (thick solid line) at time $= 526.0$ min (top right panel). The high-beta fast magneto-acoustic wave is converted into the low-beta slow magneto-acoustic wave located at $(X, Z) = (6.3, 1.0)$ Mm

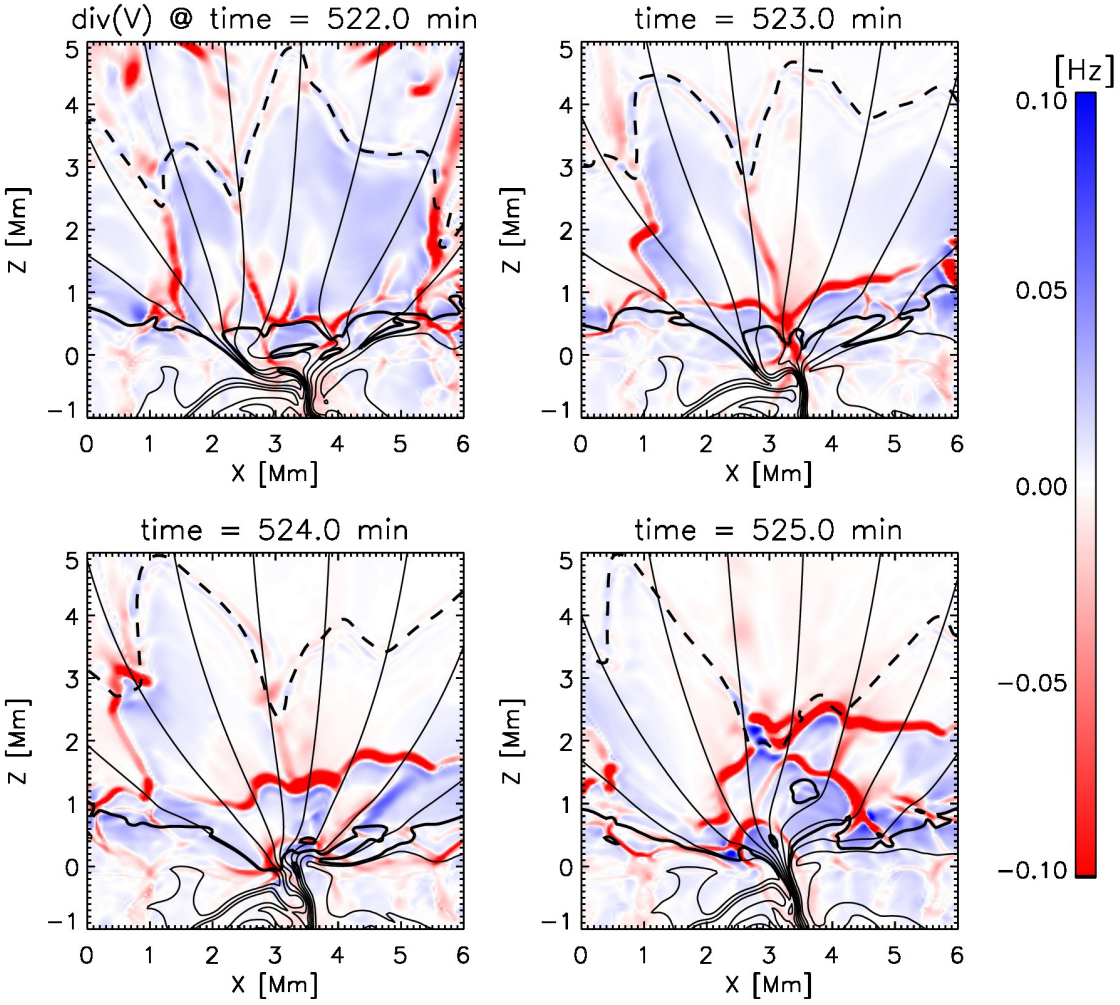

Figure 5.12: Four series of snapshots of the velocity divergence showing the excitation of acoustic waves by the collision of two nearby magnetic flux concentrations. The thin solid lines indicate the magnetic field lines. The thick solid lines represent the plasma beta unity $\beta = 1$. The dashed lines show the height of transition region ($T = 40$ kK). The results for the simulation with $B_0 = 30$ G and $T_c = 0.4$ MK are shown.

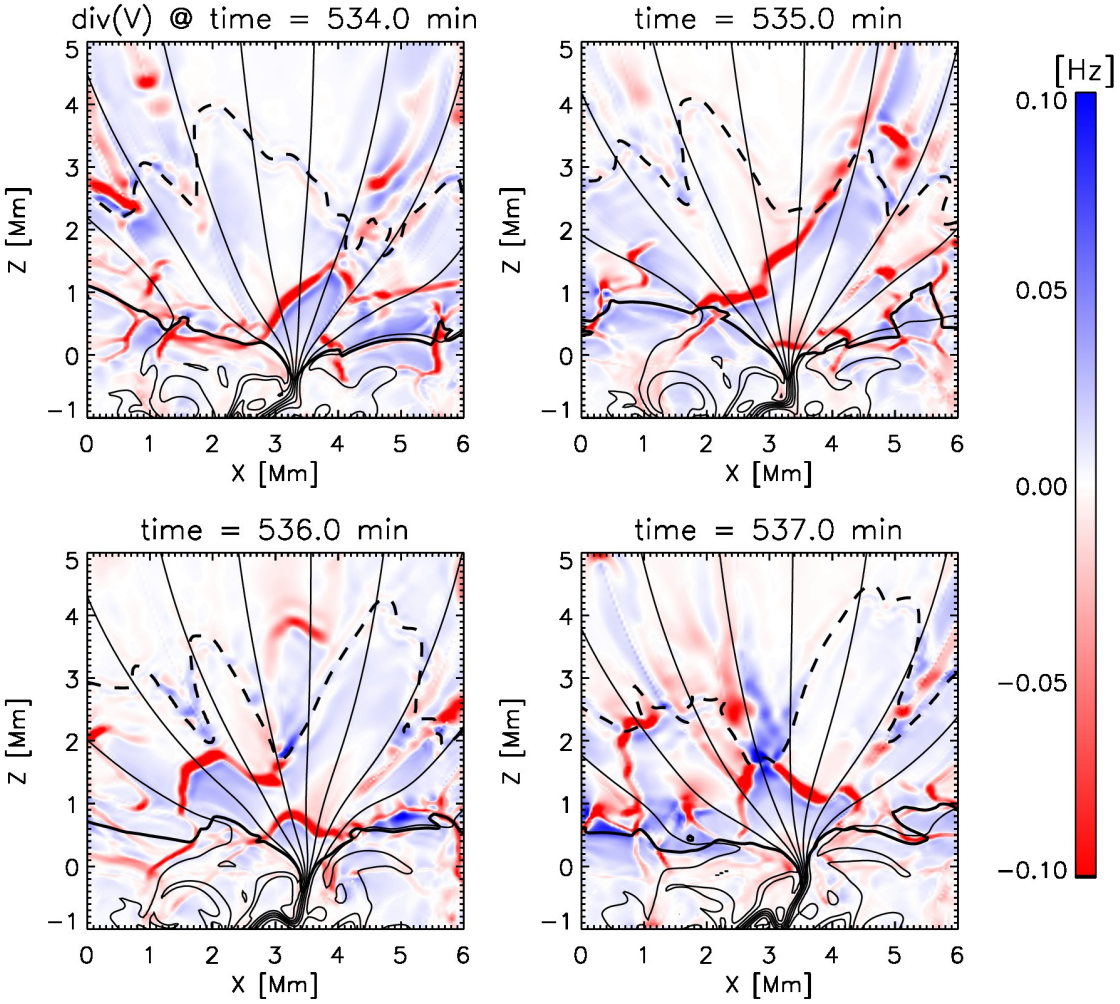

Figure 5.13: Same as Figure 5.12 but showing the persistent excitation of acoustic waves in the independent strong magnetic flux concentration.

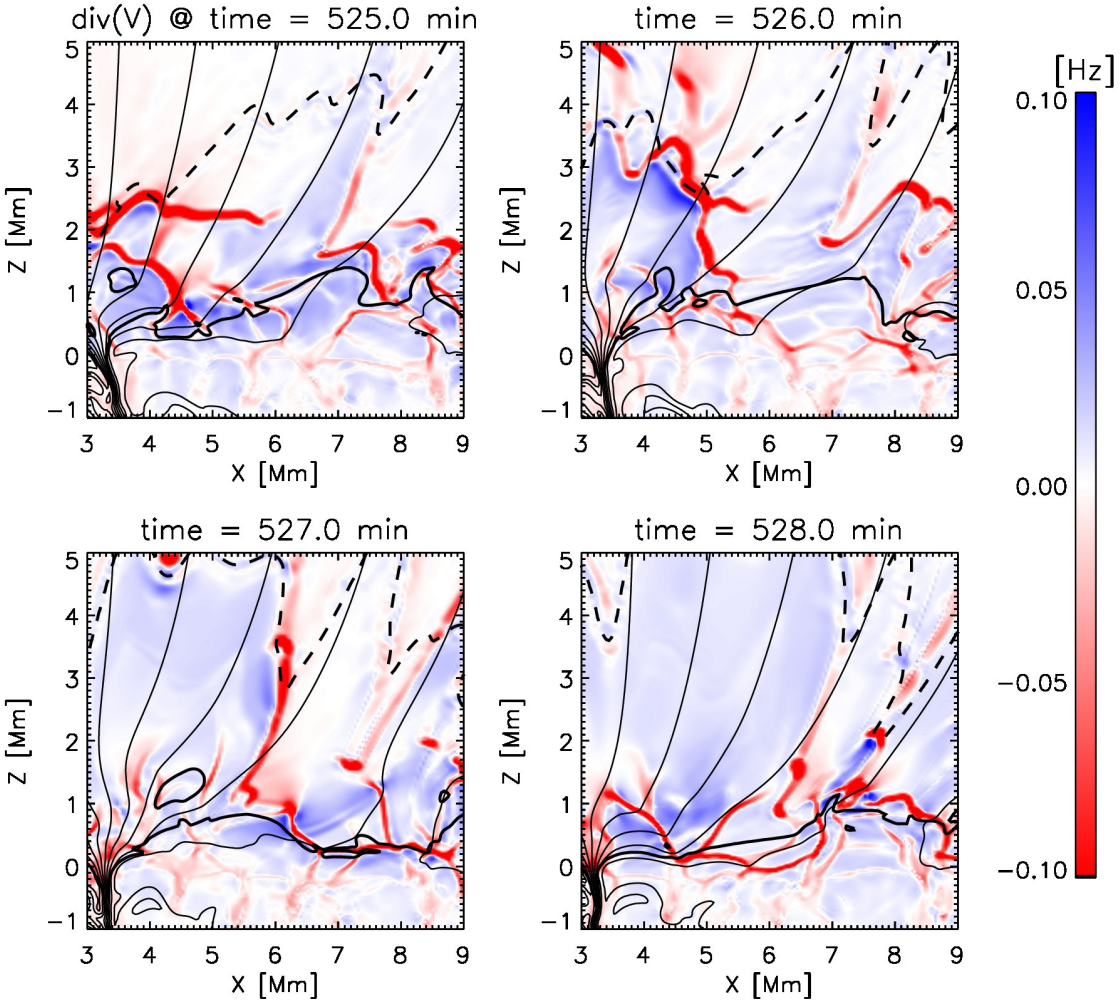

Figure 5.14: Same as Figure 5.12 but showing the interaction of acoustic waves and magnetic flux tube.

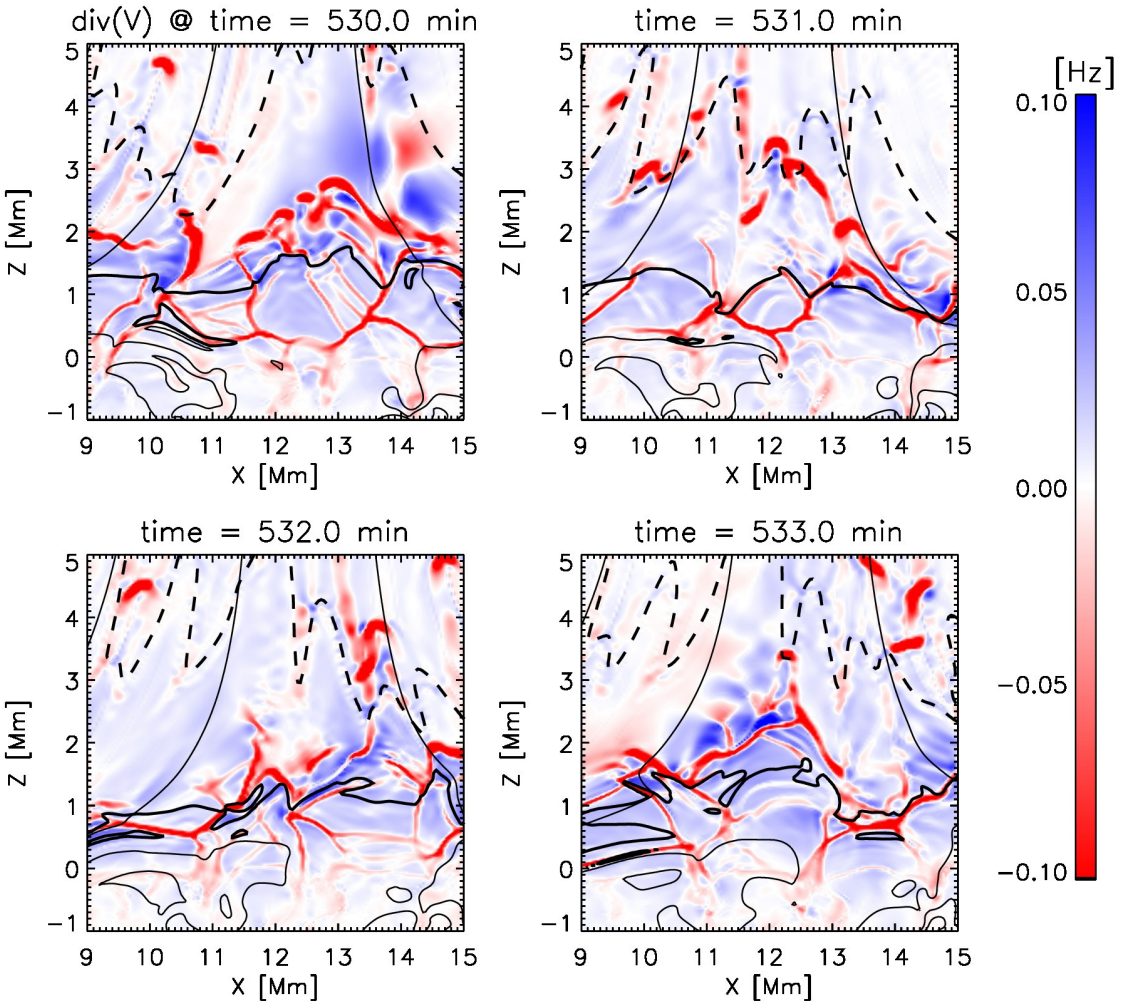

Figure 5.15: Same as Figure 5.12 but showing the interaction of acoustic waves outside the magnetic flux tube.

at time $= 527.0$ min (bottom left panel). The generated slow-mode shock wave hits the transition region located around $(X, Z) = (7.7, 2.1)$ Mm at the time of 528 min (bottom right panel). This process produces the locally concentrated acoustic perturbation near the edge of the flux tube, which is supposed to be one possible mechanism to generate the small width of chromospheric jets. We also note that the acoustic perturbation in the flux tube generated through this process does not suffer from the reduction of amplitude by the strong expansion of flux tube, because the magnetic flux tube has already expanded around the height of 1 Mm.

Figure 5.15 shows the interaction of acoustic waves outside the magnetic flux tube.

The convective motion ubiquitously produces acoustic perturbations in the photosphere ($Z \sim 0$ Mm), around the region of $X = 11$–13 Mm (top left panel). The acoustic waves interact with each other and assemble into the region of $X = 11.5$–12.5 Mm at the height of around 0.5 Mm and the time of 531 min (top right panel). The acoustic waves experience further assembling and propagate through the plasma-beta unity line located around $(X, Z) = (12, 1)$ Mm (bottom left panel). The resulting slow-mode shock waves hit the transition region at $(X, Z) = (12.3, 3.3)$ Mm (bottom right panel). This transition region is falling down earlier than the neighboring area before it collides with the shock wave. Because the shock waves are assembled and intensified through this process, the strong acoustic waves tend to be generated outside the magnetic flux tube.

5.5 Discussion

We investigate the effect of the average magnetic field on chromospheric jets. The average magnetic field strength only weakly affects the scale of chromospheric jets. The existence of the inclined magnetic field lines contributes to reduce the deceleration and produce longer-living chromospheric jets. The effect of the coronal condition investigated in the previous chapter (Iijima & Yokoyama, 2015) affects the scale of chromospheric jets more significantly. On the real sun, the coronal temperature and density will be affected by the global structure (e.g., open field or closed loop) of the magnetic field through the heating process of corona. Therefore, the difference of the average photospheric magnetic field strength will indirectly affect the regional difference of chromospheric jets through the difference of the coronal condition.

Various processes for the generation processes of acoustic waves inside the intense magnetic flux tube (Parker, 1978; Spruit, 1979; Schüssler, 1990) are suggested, such as the swaying motion (e.g., Steiner et al., 1998), granular buffeting (Hasan & Kalkofen, 1999), and pumping effect (Kato et al., 2011). The acoustic waves generated inside the flux tube propagate upward in the fan-shaped structure due to the expansion of the flux tube (Figure

5.13). This is one of the reason why the chromospheric jets are short inside the flux tube as suggested by Heggland et al. (2011). We suggest that the low density inside the flux tube also reduces the density difference between the photosphere and transition region and produces weaker amplification of shock waves by the smaller density contrast. We also find that the collision of two nearby magnetic flux tubes generates the strong acoustic perturbation (Figure 5.12), which produces tall jets inside the flux tube.

We find that the acoustic waves experience various interaction and mode conversion processes during the propagation in the photosphere and chromosphere (e.g., Rosenthal et al., 2002; Bogdan et al., 2003). The acoustic waves generated by the turbulent motions have been investigated (e.g., Goldreich et al., 1994; Nordlund & Stein, 2001; Stein & Nordlund, 2001). The collapse of granule cells also generates relatively high-frequency localized acoustic perturbations (Skartlien et al., 2000). The acoustic waves generated through these mechanisms are assembled and intensified in the weak field region between the strong magnetic flux concentrations (Figure 5.15). The intensification of acoustic waves similar to this processes is suggested in Heggland et al. (2011) as the possible candidate of the tall chromospheric jets outside the magnetic flux tube in their simulations. We also find that the high-beta acoustic waves hits the wall of the low-beta magnetic flux tube and produces the localized acoustic perturbations inside the flux tube (Figure 5.14). This interaction between the magnetic flux tube and shock wave is similar to the idealized two-dimensional simulations in Hasan & van Ballegooijen (2008) with much weaker perturbation. We suggest that this process is the possible candidate to produce thin and tall chromospheric jets inside the magnetic flux tube.

We find that the produced jets tend to be shorter in the magnetic flux tube than in the surrounding weakly magnetized regions. The coronal gas pressure tends to be high above the flux tube. Both the amplification of shock waves under the different coronal gas pressure and the difference of the driving acoustic perturbation inside and outside the flux tube contribute to produce shorter jets in the magnetic flux tube. The chromospheric jets in the real solar chromosphere are observed along the network magnetic field. This

is in contrast to our results and Heggland et al. (2011). One possible explanation of this difference is that the other driving mechanism of strong acoustic waves in the magnetic flux tube is missing in the simulations, such as the magnetic reconnection (Pikel'ner, 1969; Uchida, 1969). Another possible explanation is that the density of chromospheric jets inside the magnetic flux tube is larger than in the surroundings. Because the high coronal temperature and density is expected above the magnetic flux tube by the magnetic energy release, the density at the transition region (at the top of jets) can be higher than the non-magnetized regions.

The coronal gas pressure is higher above the magnetic flux tubes in our simulations. We do not give clear answer on this dependence, partially because of the simplified treatment of the top boundary condition that reflects a part of the wave energy. On the real sun, the strength and connectivity of the magnetic field will affect the coronal heating rate and formation of dense corona. We note that the high density in the corona over the strong magnetic flux concentration requires stronger acoustic waves to produce tall chromospheric jets (Shibata & Suematsu, 1982; Iijima & Yokoyama, 2015).

Chapter 6

Three-dimensional simulation of solar chromospheric jets

6.1 Introduction

The two-dimensionality is one of the strongest constraints of the studies presented in the previous chapters. In Chapter 4, we succeeded to reproduce the tall (> 6 Mm) chromospheric jets under the cool corona with low density using two-dimensional simulations. On the other hand, the three-dimensional simulations by Martínez-Sykora et al. (2009) produce much smaller chromospheric jets. It is not guaranteed that the tall chromospheric jets will be produced even in the three-dimensional domain. It is also interesting to address whether we can achieve tall chromospheric jets with moderately hot corona as in the quiet regions.

In Chapter 5, we pointed out that the size of jets is smaller above the magnetic flux tube than in the region with weak magnetic field. We showed that the driving process of acoustic waves is not effective near the strong magnetic field concentrations. Such dependence of the scale of chromospheric jets on the local structure of the magnetic field is also found in the two-dimensional study by Heggland et al. (2011). On the other hand, according to the observational studies, chromospheric jets appear near the network mag-

netic field (Suematsu et al., 1995; Langangen et al., 2008b; Tian et al., 2014), where the magnetic field is stronger than the surrounding inter-network region.

In this study, we conduct a three-dimensional simulation of chromospheric jets. We especially focus on the effect of the three-dimensionality on (1) the scale of chromospheric jets and (2) the distribution of jets on the structure of magnetic field.

6.2 Simulation setup

The basic equations and numerical methods are described in Chapters 2 and 3. We conduct a simulation with three-dimensional numerical domain spanning $9 \times 9 \times 16$ Mm^3, including the upper convection zone of 2 Mm. The uniform grid spacing of 41.7 km in horizontal (X and Y) direction and 29.6 km in vertical direction is employed. The boundary condition is same as described in Chapter 4. First, we impose a uniform vertical magnetic field of 10 G on the sufficiently relaxed three-dimensional atmosphere with the doubled horizontal grid spacing of 83.4 km. We integrate this low-resolution simulation for 3 solar hours (3 hours in the internal time of the simulation). Next, we redefine the horizontal grid spacing to be 41.7 km and integrate the simulation for 1 solar hour. We analyze the last 30 min of the simulation. The thermal conductive flux from the top boundary is imposed to maintain the coronal temperature to be higher than 1 MK as in Chapters 4 and 5.

6.3 Structure of atmosphere

Figure 6.1 shows the vertical structure of simulated atmosphere. Because of the thermal conductive flux imposed at the top boundary, the coronal temperature is maintained to be almost 1 MK. The gas pressure and mass density is also uniform in the corona. We also observe that the cool chromospheric plasma with the density of 10^{-12}–10^{-14} g/cm^3 covers the height range between 2–10 Mm. This result implies the existence of tall chro-

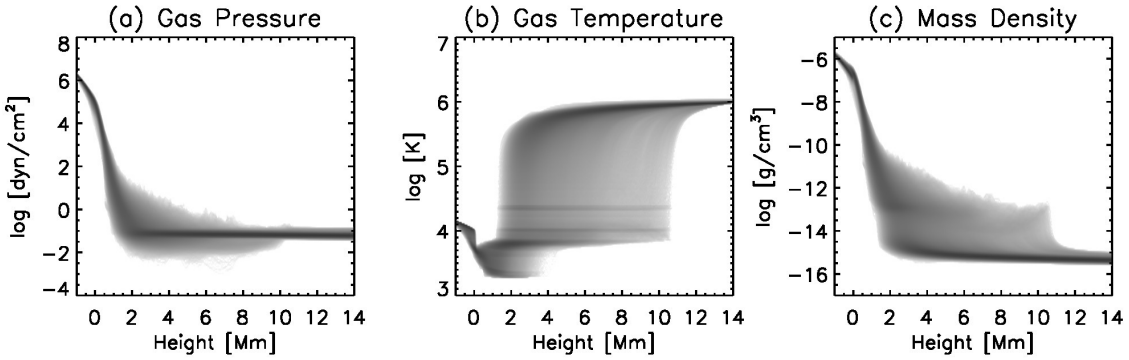

Figure 6.1: Vertical structure of the simulated atmosphere. The probability density functions (PDFs) of (a) gas pressure, (b) gas temperature, and (c) mass density are shown.

mospheric jets in the simulation as shown in the following sections.

Figure 6.2 presents the horizontal structure of the simulated atmosphere at the surface ($Z = 0$ Mm). The granulation pattern with the typical diameter of about 1 Mm is identified in the map of vertical velocity. The vertical vorticity of order 0.1 Hz is reproduced near the boundary of the granulation. The convective motion advects the vertical magnetic field to form kilogauss magnetic field concentrations around the edge of the granulation.

Figure 6.3 shows the correlation between the field-aligned velocity and mass density over the whole spatial and temporal domain. As we have investigated in Chapter 4, chromospheric shock waves are amplified under the density stratification. We find that the amplitude of the velocity is slightly smaller than the two-dimensional studies in the previous chapters (see Fig. 4.10). The index of the power law relation between the field-aligned velocity and mass density is almost same as or slightly larger than the index of 0.1 derived in Chapter 4 (Iijima & Yokoyama, 2015) and smaller than the semi-analytic estimate of 0.236 by Ôno et al. (1960). The difference from the two-dimensional simulations in Chapter 4 is probably caused by the reduction of radiative damping with the weaker strength of shock waves in addition to the three-dimensional dispersion of waves. Considering the uniform distribution of coronal gas pressure in Figure 6.1(a), the difference of the scale of chromospheric jets in this simulation comes from the difference of the strength of the driving mechanism.

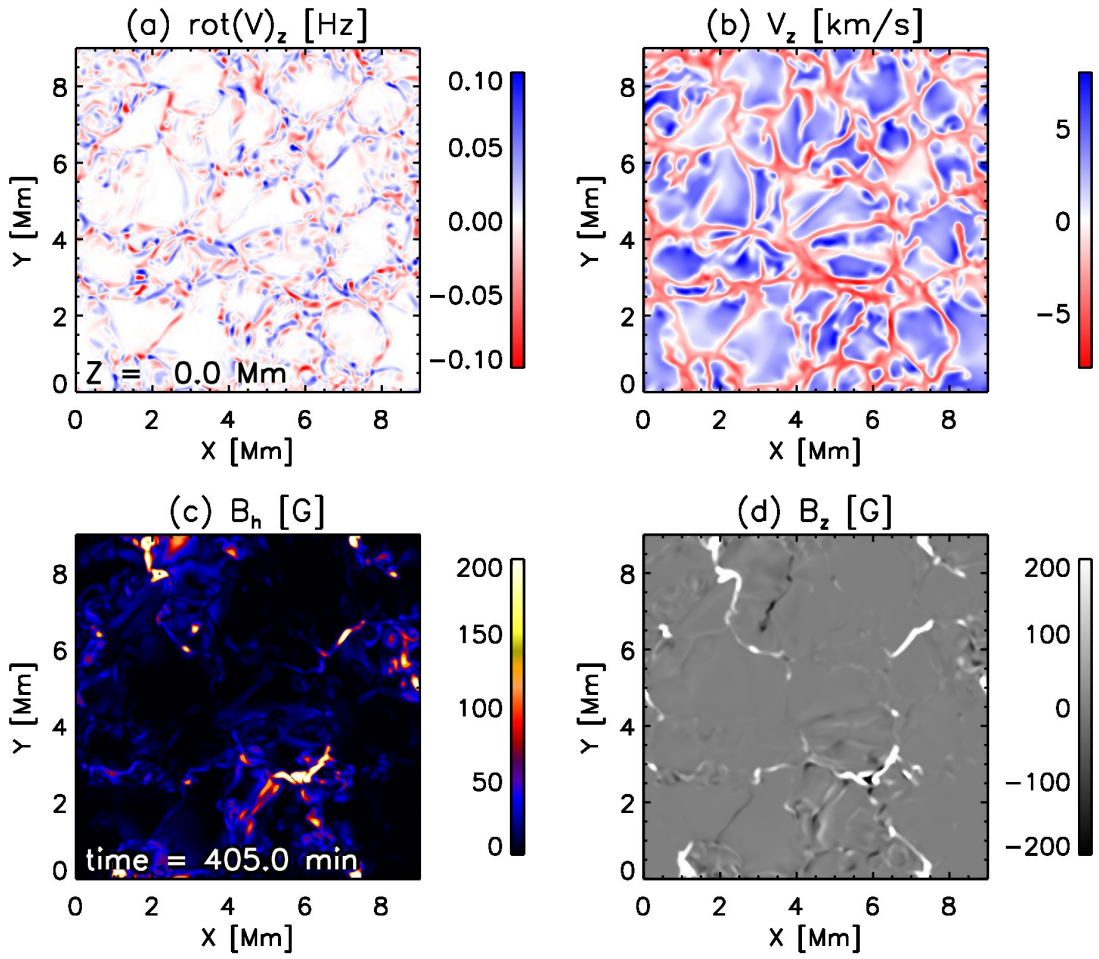

Figure 6.2: (a) Vertical component of vorticity, (b) vertical velocity, (c) horizontal magnetic field strength, and (d) vertical magnetic field on the horizontal plane at $Z = 0$ Mm.

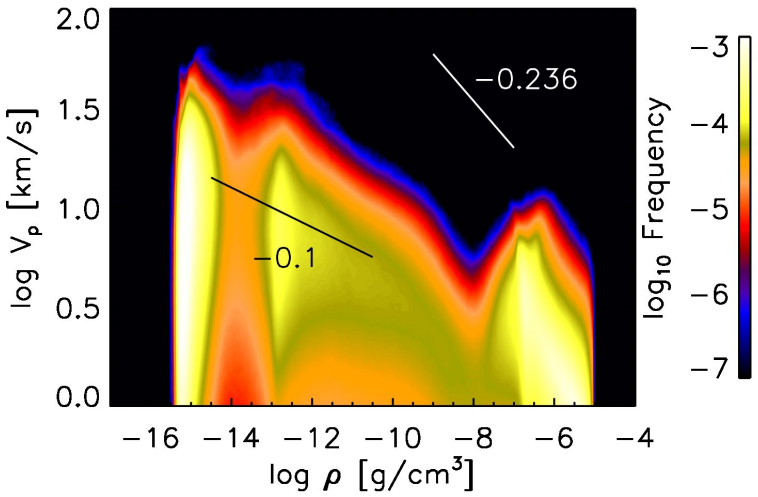

Figure 6.3: Joint probability density function of the field-aligned velocity against the mass density over the whole spatial and temporal domain. The black and white lines represent the slope for the power law relations of $V_\mathrm{p} \propto \rho^{-0.1}$ (Iijima & Yokoyama (2015) and Chapter 4) and $V_\mathrm{p} \propto \rho^{-0.236}$ (Ôno et al., 1960), respectively.

6.4 Statistical analysis of chromospheric jets

Following the method used in the previous chapters, we detect the simulated chromospheric jets automatically from the motion of the height of the transition region. Figure 6.4 shows the histograms of the properties of chromospheric jets. We can compare this result with the two-dimensional simulation (Figure 5.2, blue solid lines). The distribution in the three-dimensional simulation is very similar to the result in the two-dimensional simulation. We note that this frequency should not be compared with the observation directly, because we derive these properties only from the motion of the transition region. The effect of superposition will produce lower frequency of small-scale jets.

The properties of taller chromospheric jets are clearly shown in the scatter plot in Figure 6.5. The result can be compared with the two-dimensional simulation (Figure 5.3). Although the majority of jets are similar to the two-dimensional case, the tall chromospheric jets with the maximum length of 5–7 Mm appear in the three-dimensional case. The tallest jets have the maximum velocity of about 70 km/s, which implies the existence

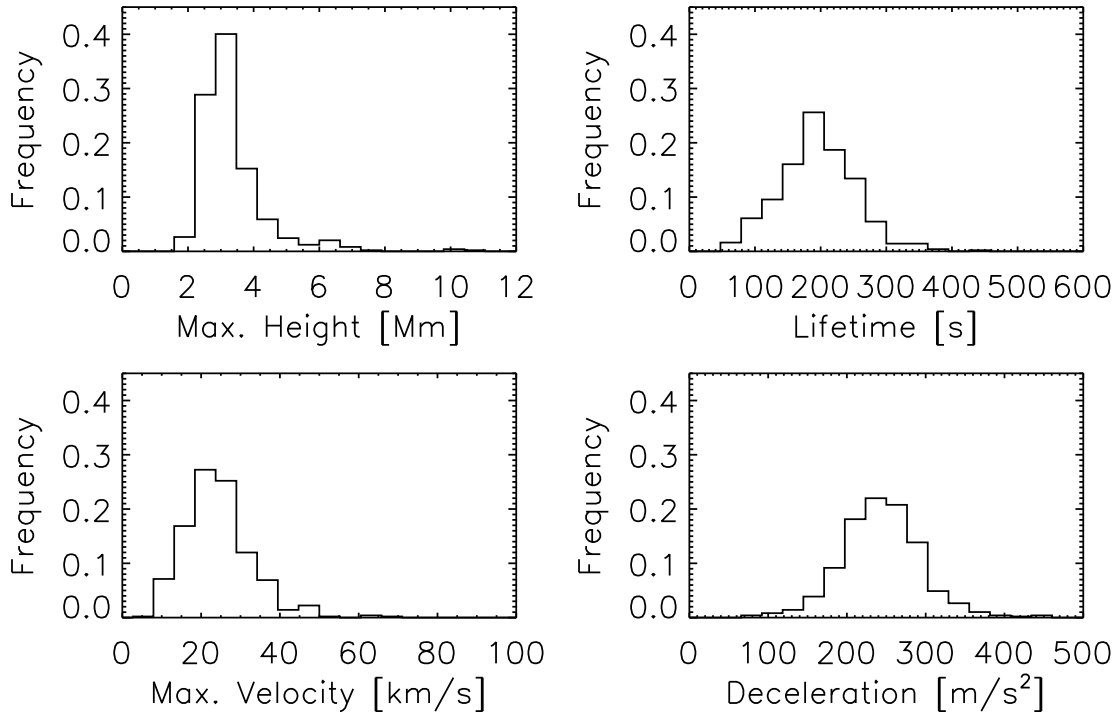

Figure 6.4: Histograms showing the maximum height (top left), lifetime(top right), maximum upward velocity (bottom left), and deceleration (bottom right) of chromospheric jets.

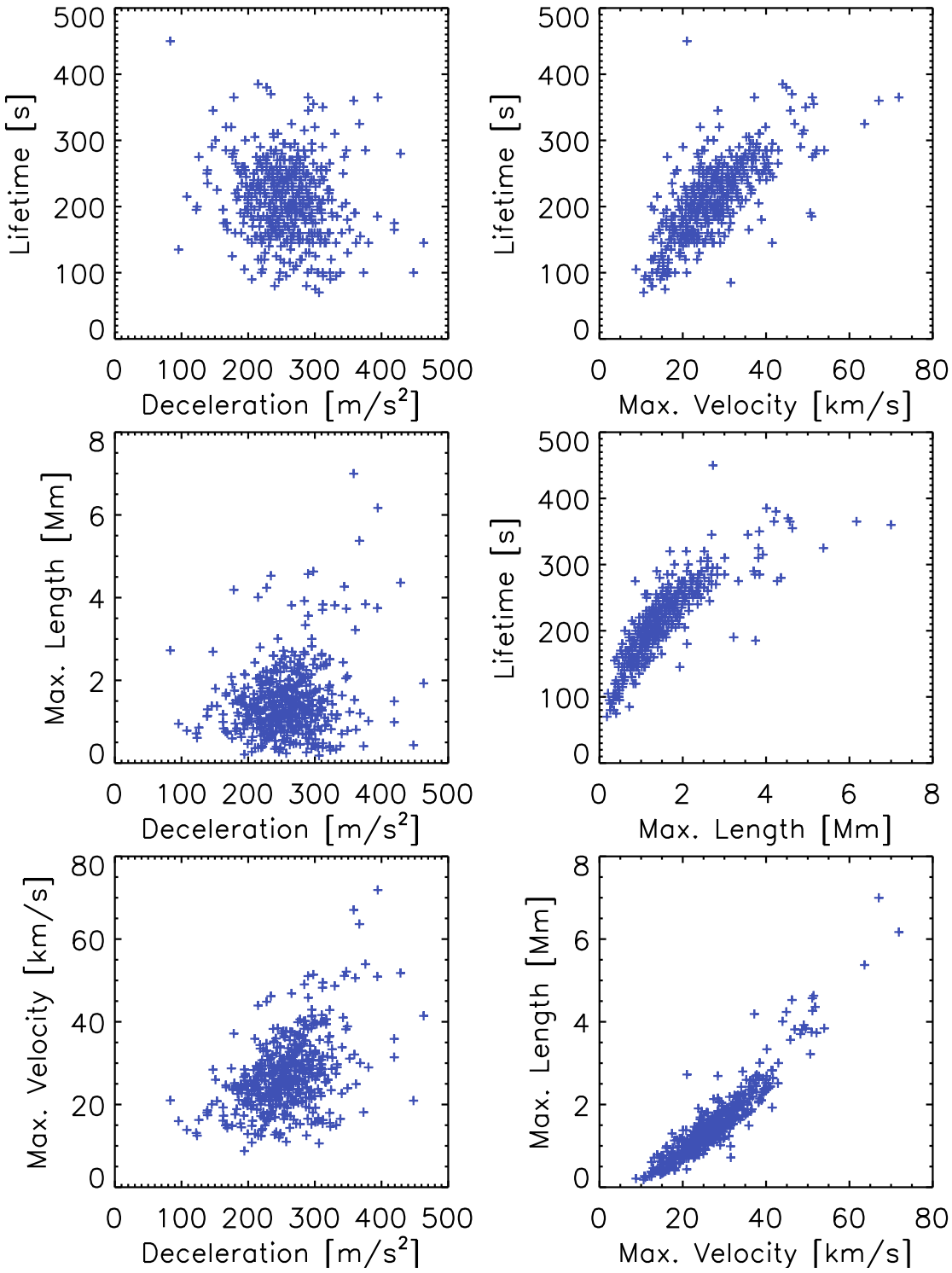

Figure 6.5: Statistical properties of the produced chromospheric jets. Each cross sign corresponds to a chromospheric jet detected.

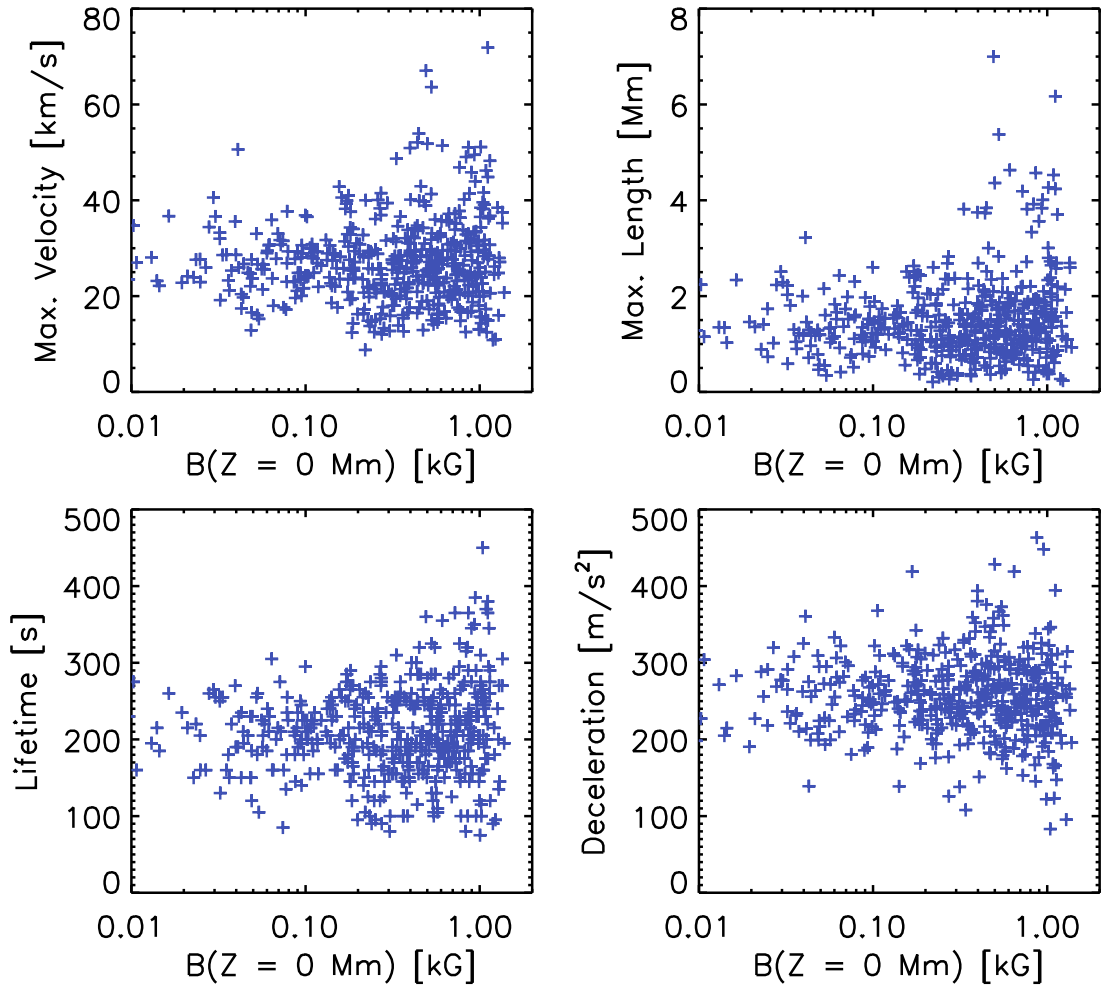

Figure 6.6: Dependence of the maximum upward velocity (top left), maximum length (top right), lifetime (bottom left), and deceleration (bottom right) of simulated chromospheric jets on the magnetic field strength observed at the height of $Z = 0$ Mm. Each cross sign corresponds to a chromospheric jet detected.

of the strong driver of chromospheric jets.

Figure 6.6 shows the dependence of chromospheric jets on the photospheric magnetic field. The magnetic field strength at the surface for each jet is measured at the time when the transition region height reaches the maximum. The tall chromospheric jets with the maximum length greater than 4 Mm only appear above the strong photospheric magnetic field (the magnetic field strength $>$ 300 G). The results indicate that the magnetic field plays an important role for the formation of tall chromospheric jets in this simulation.

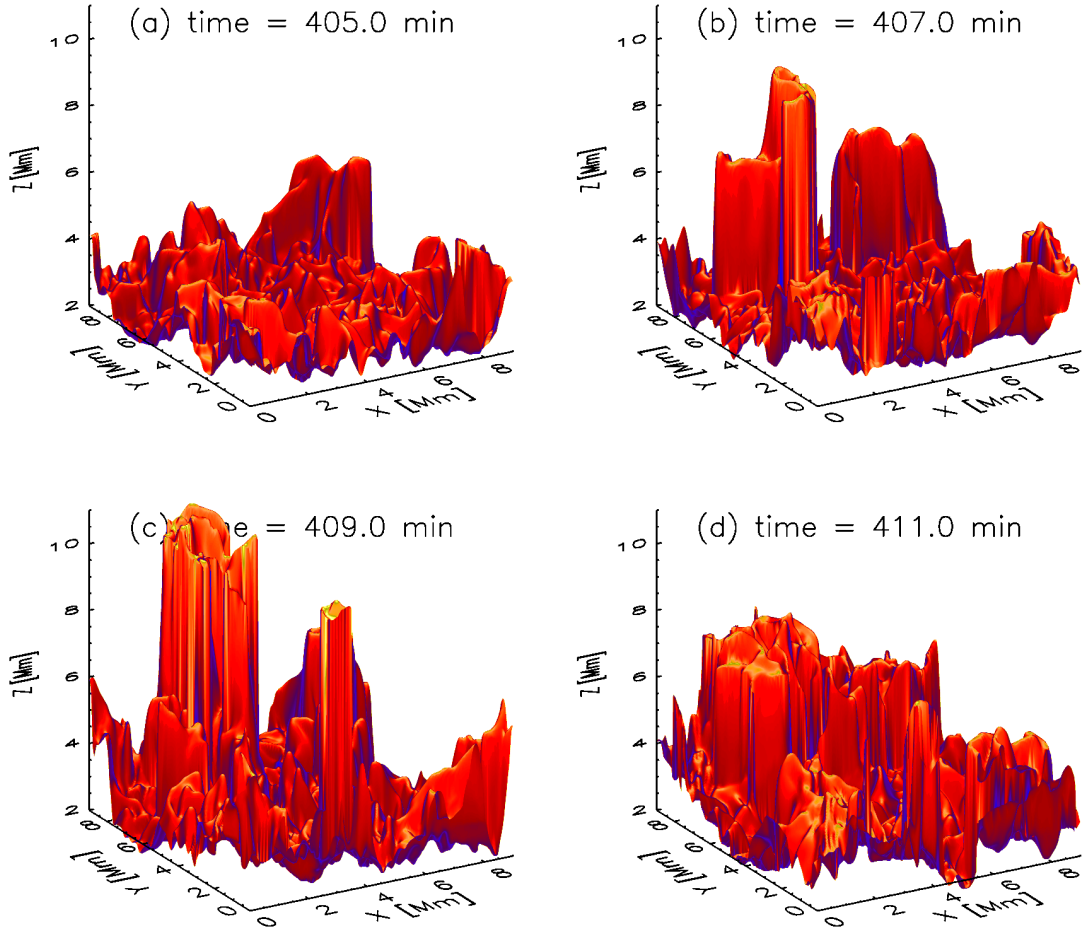

Figure 6.7: Four snapshots of the height of the chromosphere-corona transition region. The transition region is defined as the height where the gas temperature becomes 40000 K.

6.5 Properties of typical chromospheric jets

Figure 6.7 presents the three-dimensional structure of the transition region. The transition region is defined as the height where the temperature equals 40000 K in this study. The transition region is elevated up to about 11 Mm near $(X, Y) \sim (2, 8)$ Mm, where the strong magnetic field concentrations in the photosphere are found (see Figure 6.2). The chromospheric jets form a cluster with the diameter of 2–3 Mm on the horizontal plane. The cluster seems to have the fine structure with the horizontal size ranging from several hundreds to one thousand kilometers. In the following of this study, we focus on the

properties and formation of this cluster of tall chromospheric jets.

For the visualization of this cluster of chromospheric jets, we use the pseudo-emission ϵ in the optically thin approximation defined as

$$\epsilon = \int n_{\rm e} n_{\rm H} G(T) {\rm d}l, \tag{6.1}$$

where $n_{\rm e}$ is the number density of electrons and $n_{\rm H}$ is the number density of hydrogen nuclei. The line integral is taken along the line-of-sight of the pseudo-observation. We assume a Gaussian function for the contribution function $G(T)$ as

$$G(T) = C_0 \exp\left[-\left(\frac{\log_{10} T/T_c}{\Delta \log_{10} T} \right)^2 \right], \tag{6.2}$$

where we set $\log_{10} T_c[K] = 4.2$ and $\Delta \log_{10} T = 0.15$. The normalization constant $C_0 = 10^{-28}$ [cm^{-7}] is taken so that the pseudo-emission in Eq. (6.1) becomes unity (dimensionless) for the plasma with the number density of $n_{\rm e} = n_{\rm H} = 10^{10}$ [cm^{-3}] and the line-of-sight thickness of 1 Mm. This contribution function is sensitive to the temperature range of the upper chromosphere.

Figure 6.8 shows the pseudo-emission observed from the negative Y-direction. The line integral in Eq. (6.1) is taken over the whole Y-direction for each (X, Z). The cluster of the chromospheric jets found in Figure 6.7 is located around X = 2–4 Mm. The height range and time evolution are consistent with the motion of the transition region in Figure 6.7. This proves that this pseudo-emission can be used as the good indicator of chromospheric jets.

Figure 6.9 shows the time evolution of the chromospheric jets. Because the chromospheric jets are deformed by swaying and torsional motions, the slit position is not always at the center of the jets. We roughly estimate the scale of this jets by eye and get the maximum length of the elevation of about 7 Mm and lifetime of about 9 min. We estimate the maximum upward velocity of about 52 km/s and deceleration of about 192 m/s^2 assuming

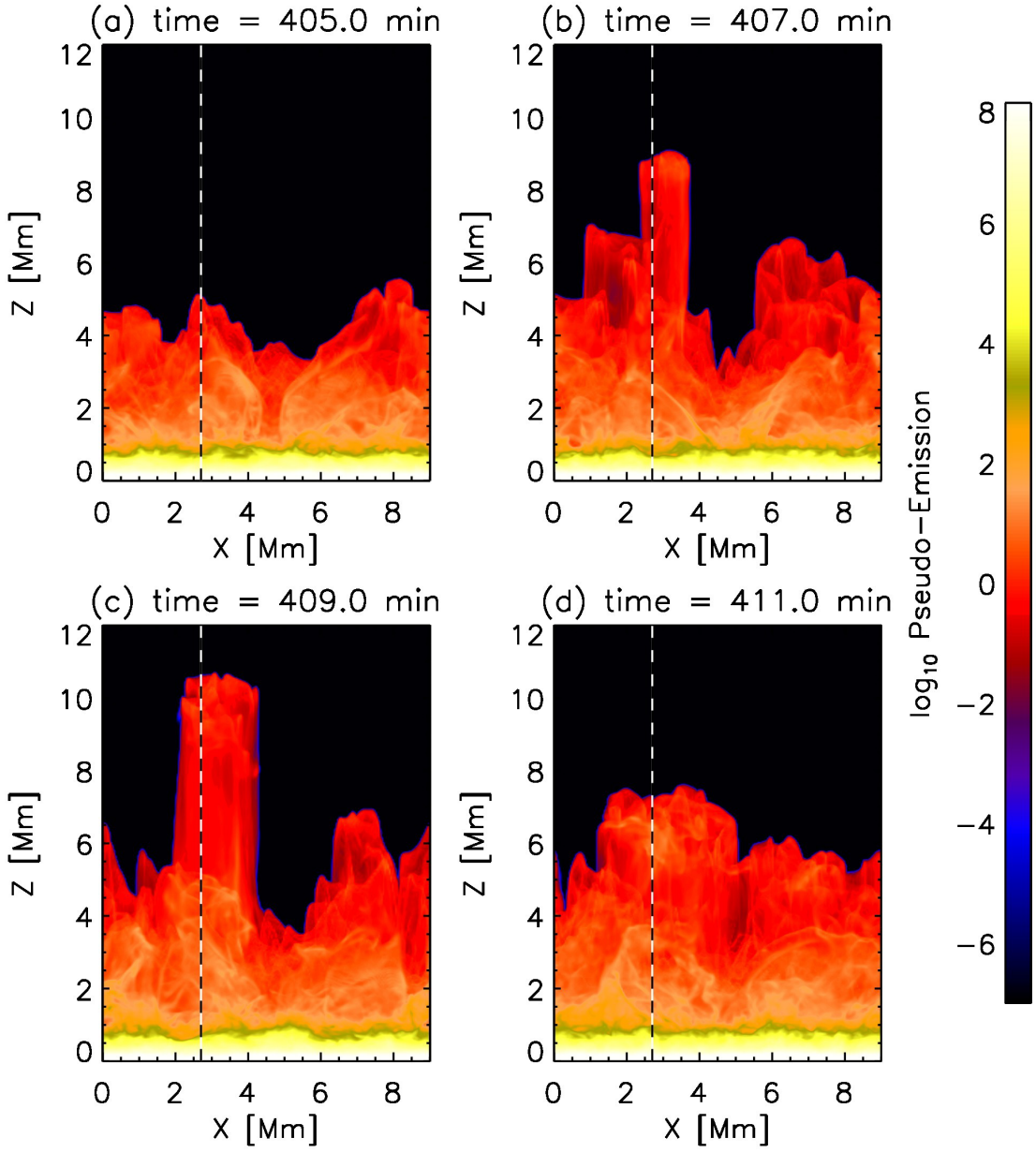

Figure 6.8: Four snapshots of the logarithm of the pseudo-emission defined in Eq. (6.1) observed from the negative Y-direction. The dashed lines represent the position of the slit plotted in Figure 6.9.

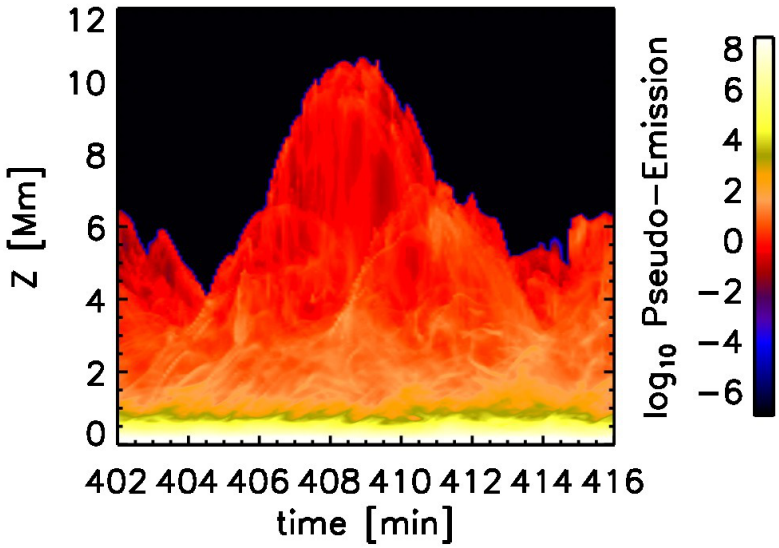

Figure 6.9: Time evolution of the logarithm of the pseudo-emission at the slit of $X = 2.7$ Mm in Figure 6.8.

the parabolic trajectory.

6.6 Formation of typical chromospheric jets

Figure 6.10 shows the topology of the magnetic field lines and streamlines above the strong magnetic field concentration at $(X, Y, Z) \sim (2, 8, 0)$ Mm. The streamlines presents strong vortex extending from the photosphere to the upper chromosphere and corona, which looks like the higher layer extension of the "magnetic tornadoes" reported by Wedemeyer-Böhm et al. (2012). In our simulation, not only the streamlines but also the magnetic field lines are also twisted and strongly entangled in the chromosphere. We also note that the axis of this vortex is slightly inclined toward the positive X-direction.

Figure 6.11 shows the horizontal cut at $Z = 1$ Mm near the root of the "tornado". The small-scale swirl is found at $(X, Y) \sim (2, 8)$ Mm. The lifetime of this swirl event is longer than 5 min. The swirl has a hot center with downward flow and a cool edge with upward flow. The vertical vorticity have the sign opposite to the vertical rotation of the magnetic field, which is consistent with the upward-propagating torsional Alfvén wave.

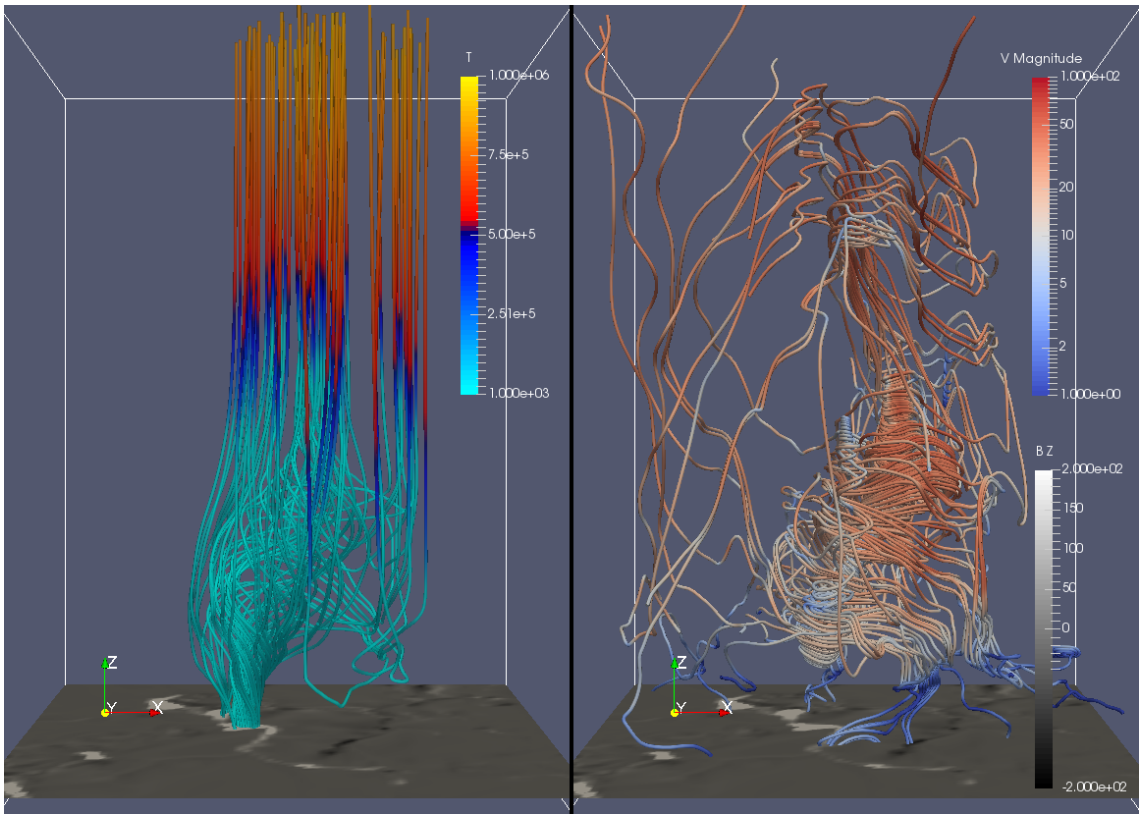

Figure 6.10: Topology of the magnetic field lines (left panel) and streamlines (right panel) in the small box of $6 \times 6 \times 8.5$ Mm (including 0.5 Mm below $Z = 0$ Mm) near the photospheric magnetic field concentration at $(X, Y) \sim (2, 8)$ Mm. A snapshot at the time of 405 min is shown. The color along the magnetic field lines indicates the gas temperature [K]. The color along the streamlines represents the magnitude of the velocity [km/s]. The horizontal slice of the vertical magnetic field at $Z = 0$ Mm is also shown in gray scale.

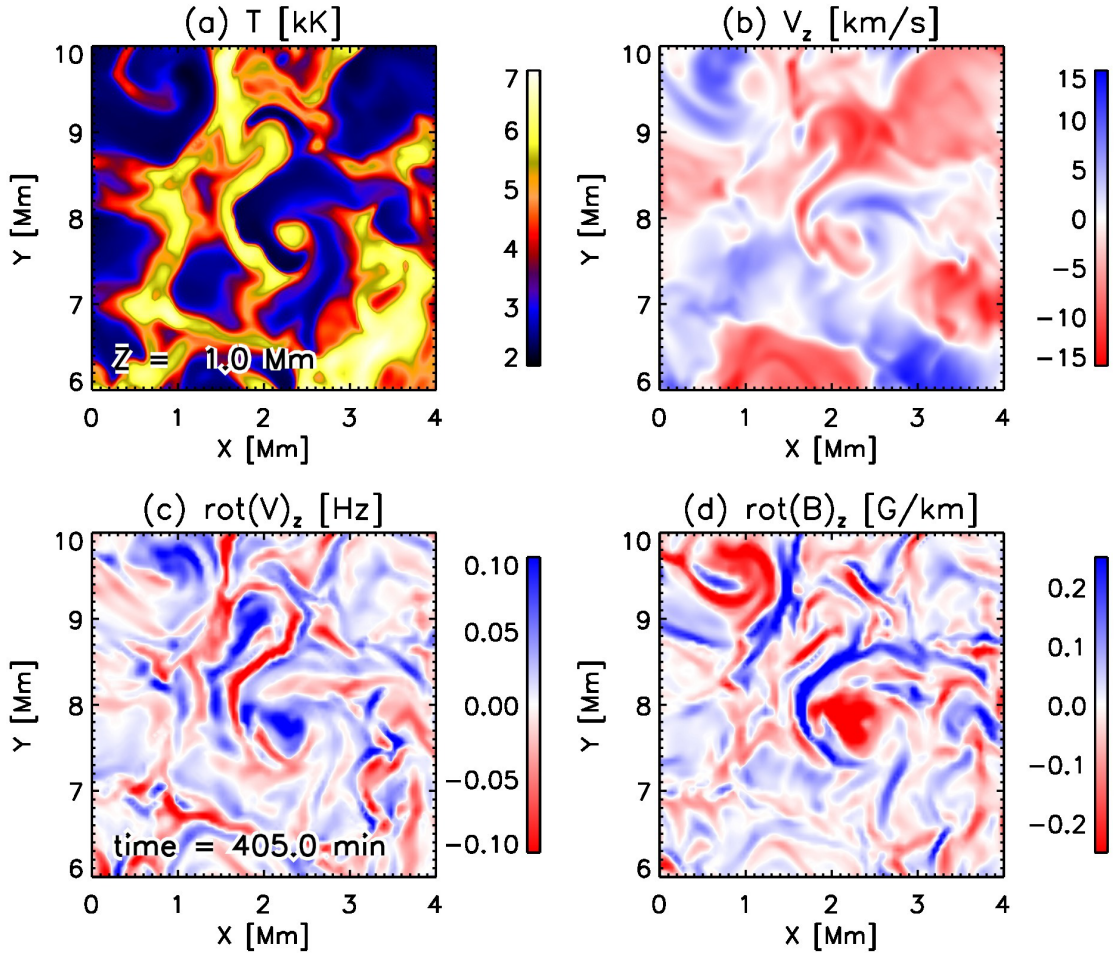

Figure 6.11: (a) Temperature, (b) vertical component of the velocity field, (c) vertical component of the vorticity, and (d) vertical component of the rotation of the magnetic field on the horizontal plane at $Z = 1$ Mm and time $= 405.0$ min. The variables of $Y > 9$ Mm are calculated assuming the periodic horizontal boundary condition.

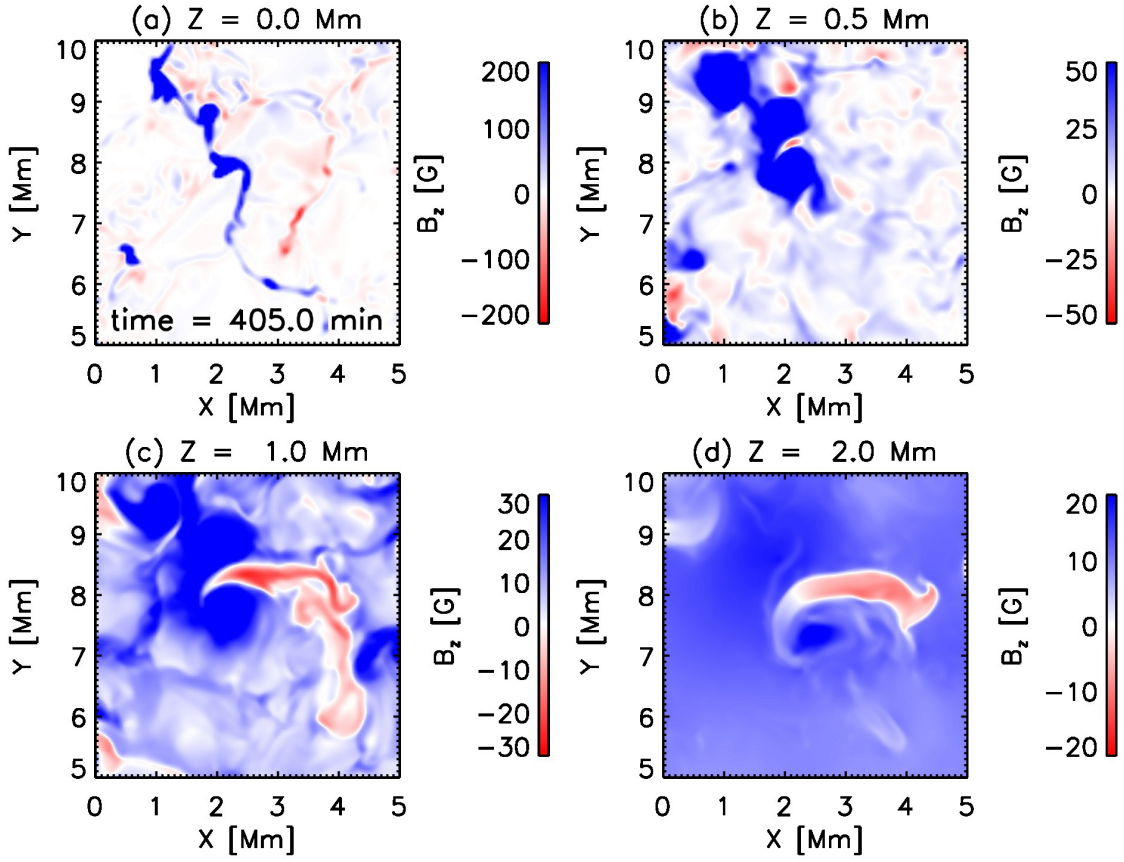

Figure 6.12: Vertical magnetic field at the four different layers of $Z =$ (a) 0.0, (b) 0.5, (c) 1.0, and (d) 2.0 Mm at time = 405.0 min.

This long-living swirl is the cause of the twisted structure of the magnetic field lines and streamlines in Figure 6.10.

Figure 6.12 presents the vertical magnetic field at various heights. We find the vertical magnetic field with the opposite polarity at X = 2–4 Mm and Y = 8 Mm, which is beside the axis of the swirling motion in Figure 6.11. This opposite-polarity patch in the chromosphere ($Z =$ 1.0 and 2.0 Mm) does not exist near the temperature minimum ($Z =$ 0.5 Mm) or the surface ($Z =$ 0.0 Mm).

Figure 6.13 shows the three-dimensional topology of the magnetic field lines with the slice at Z = 1 Mm. The negative-polarity magnetic patch found in Figure 6.12 is a part of the positive magnetic patch at $(X, Y, Z) \sim (2, 8, 0)$ Mm. The rotational motion of the "tornado" that inclined to the positive X-direction can help to produce this structure. The swirling magnetic field lines drag the heavy and cool plasma upward in

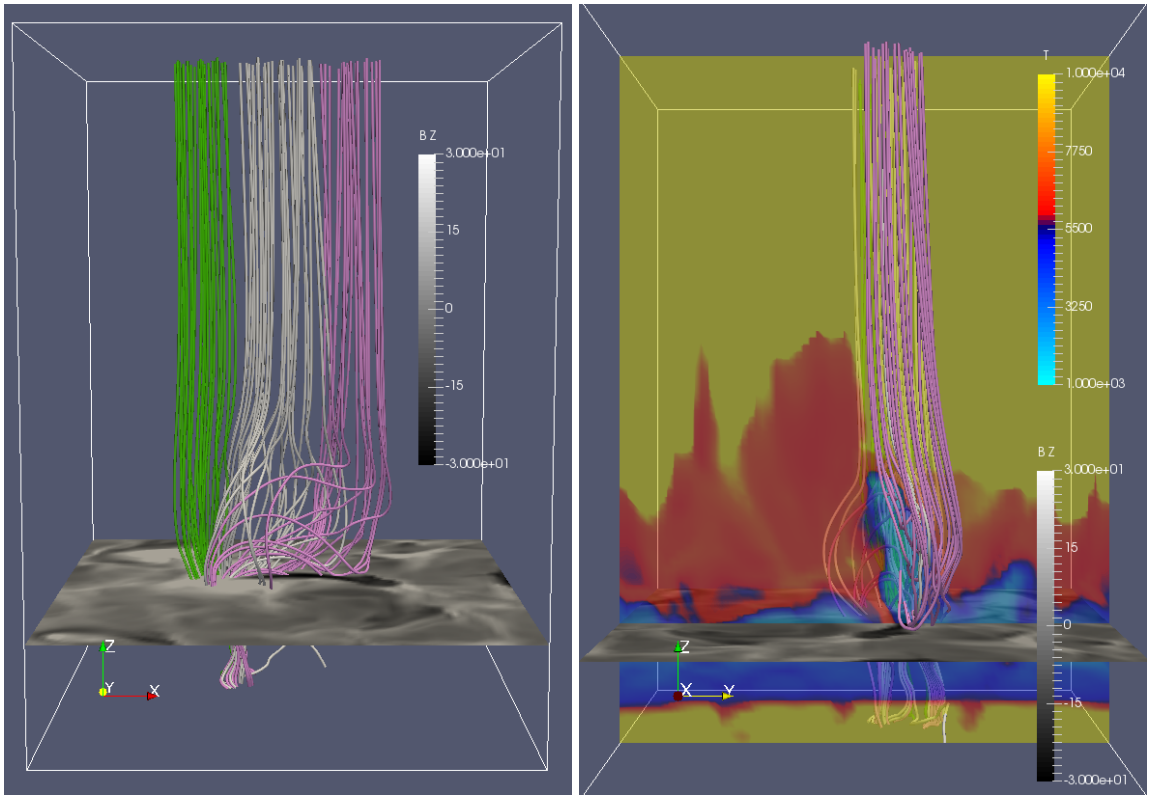

Figure 6.13: Topology of the magnetic field lines in the small box of $6 \times 6 \times 8.5$ Mm near the photospheric magnetic field concentration at $(X, Y) \sim (2, 8)$ Mm and time $=$ 404.0 min. The horizontal slice of the vertical magnetic field [G] at $Z = 1$ Mm is shown in gray scale. Left panel: Topology of the magnetic field lines viewed from the negative Y-direction. Right panel: Topology of the magnetic field lines viewed from the positive X-direction. Gas temperature [K] on the (Y, Z)-plane of $X = 3$ Mm is also shown.

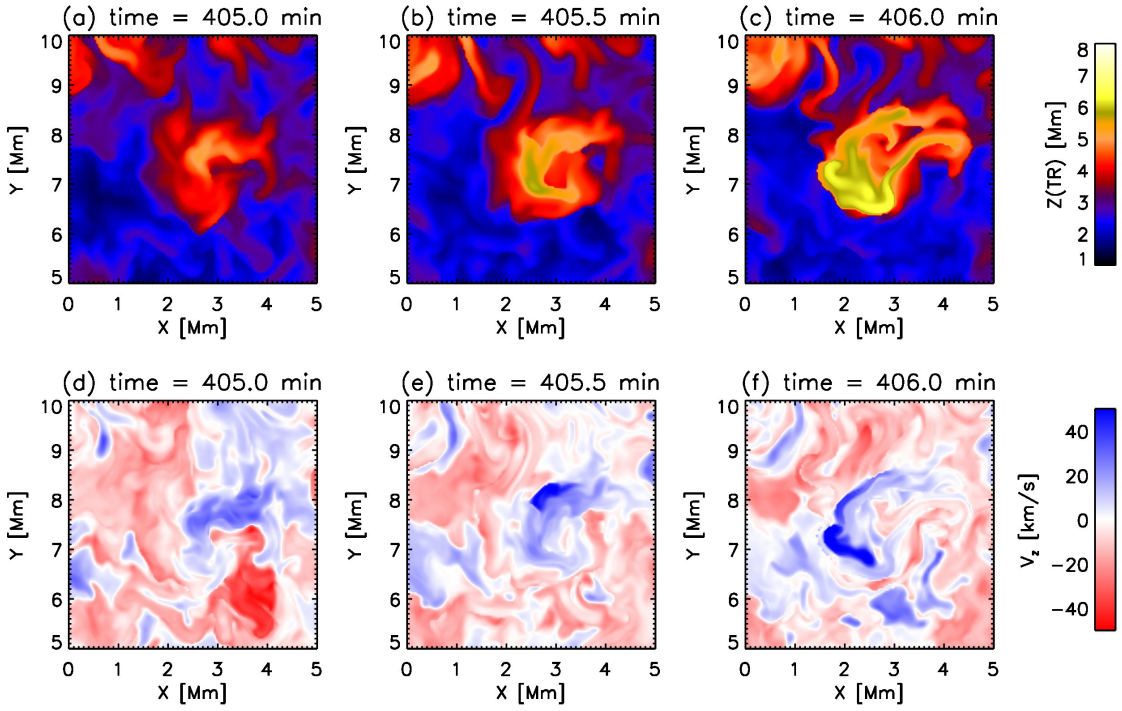

Figure 6.14: Time evolution of the transition region height (top row) and vertical velocity at the transition region (bottom row). Shown are the snapshots at time = 405.0 (left column), 405.5 (middle column), and 406.0 min (right column).

the chromosphere (shown in the right panel). The dragged heavy plasma deforms the magnetic field lines (shown as magenta lines) and produces negative magnetic patch in the middle chromosphere.

Figure 6.14 shows the motion of the transition region at the initial phase of the jet formation around $(X, Y) \sim (2, 8)$ Mm. The chromospheric jets begin to rise in the region of $X = 2$–4 Mm and $Y \sim 8$ Mm at time = 405.0 min. This rising region corresponds to the region of negative magnetic patch in the chromosphere shown in Figure 6.12. The rising region is deformed and rotated by the swirling motion in the chromosphere throughout the emergence of chromospheric jets.

Figure 6.15 shows the (Y, Z)-slice at $X = 3$ Mm. The negative vertical magnetic field is located at $Y = 8$ Mm. The cool plasma is lifted upward along this vertical field. Because the plasma beta is low enough in the upper chromosphere, this upward motion is mainly driven by the Lorentz force, which can be understood as the part of the rotational

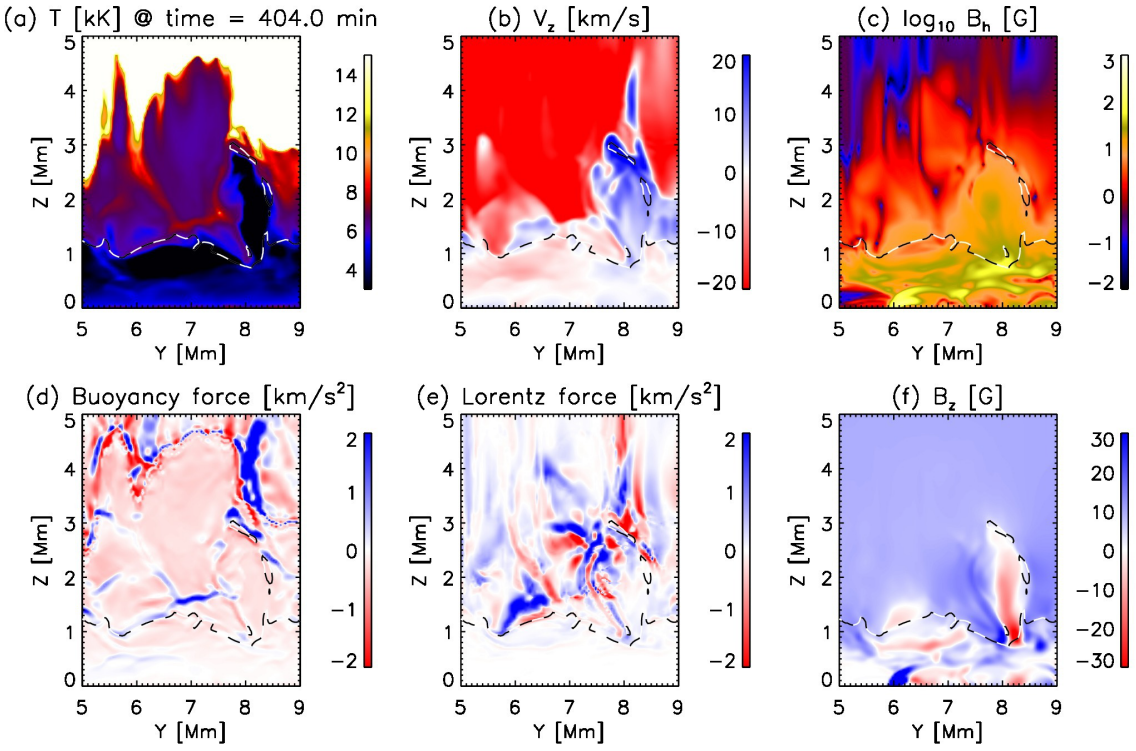

Figure 6.15: Physical quantities on the (Y, Z)-plane at $X = 3$ Mm. Shown are (a) the gas temperature, (b) the vertical velocity, (c) the logarithm of horizontal magnetic field, (d) the vertical component of the buoyancy (gas pressure gradient plus gravitational) force, (e) the vertical component of the Lorentz force, and (f) the vertical magnetic field at the time of 404 min. The dashed lines indicate the plasma-beta unity.

motion of the "tornado" in Figure 6.10. The accelerated cool and dense plasma hits the transition region at $(Y, Z) \sim (8, 3)$ Mm and produces the tall chromospheric jets.

6.7 Discussion

In this study, we present the results of a three-dimensional simulation of solar chromospheric jets. We successfully reproduce a cluster of chromospheric jets with the maximum height of 10–11 Mm and lifetime of 8–10 min under the corona of 1 MK. The transition region becomes higher above the strong concentration of the magnetic field in the photosphere. The tall chromospheric jets above the strong magnetic flux tube is driven by the Lorentz force that relates to the rotational motion of the flux tube.

The tall chromospheric jets are found above the strong magnetic field concentrations in the photospheric level. This result is consistent with the relation between chromospheric jets and the network magnetic field (Suematsu et al., 1995; Langangen et al., 2008b; Tian et al., 2014). The typical tall chromospheric jets in our simulation show parabolic path with the maximum height of about 11 Mm, the lifetime of about 9 min, the maximum velocity of about 50 km/s, and the deceleration of about 192 m/s^2. These parameters are in good agreement with the observed properties of the spicules in the quiet region (e.g., Skogsrud et al., 2015).

We find the strongly twisted streamlines in the chromosphere. The tornado-like streamlines above the strong magnetic concentration are reported by Wedemeyer-Böhm et al. (2012) and numerically investigated by several authors (e.g., Wedemeyer-Böhm et al., 2012; Kitiashvili et al., 2013; Shelyag et al., 2013) without including the corona above the chromosphere. In our simulation, the chromospheric magnetic field is also twisted following the swirling motion. Kitiashvili et al. (2013) reported weakly twisted magnetic field lines produced by the chromospheric swirls. Because the average vertical magnetic field strength of 10 G in their simulation is same as ours, the difference is probably produced by the position of the top boundary. The simulations by Wedemeyer-Böhm et al.

(2012) and Shelyag et al. (2013) investigated the cases with stronger magnetic field. Both of them exhibit little twist of the magnetic field probably due to the fast Alfvén speed in the chromosphere. The effect of the average vertical magnetic field strength on the formation of chromospheric jets should be investigated in the future.

We show that the dragging of the chromospheric material by the torsional motion plays an important role for the production of chromospheric jets. In the real solar chromosphere, the ambipolar diffusion produced by the drift motion between the ions and neutrals will reduce the efficiency of the dragging of chromospheric material, which will lead to the smaller scale of chromospheric jets. The similar reduction of the drag of chromospheric plasma is investigated in the context of the flux emergence and active region formation (Leake & Arber, 2006; Arber et al., 2007; Leake & Linton, 2013). Another effect of the ambipolar diffusion is to help the formation of thin current sheets (Parker, 1963; Brandenburg & Zweibel, 1994) and the occurrence of the fast magnetic reconnection in the chromosphere. A further study with more focus on the ambipolar diffusion is therefore suggested.

We find that the produced chromospheric jets form a cluster with the diameter of several Mm with finer strands. Suematsu et al. (2008) reported similar multi-threaded nature of spicules. Skogsrud et al. (2014) suggested that the Kelvin-Helmholtz instability by the swaying motion like in the coronal loop (Antolin et al., 2014) produces the multi-threaded nature. We find the strong swirl and resulting twisted magnetic field in the chromosphere. We also show that the initial phase of the chromospheric jets formation is deformed by this swirling motion (see Figure 6.14). Further analysis is recommended to clarify the exact mechanism of the horizontal structure formation and the relation between the radiative emission and horizontal structure of the chromospheric material.

Chapter 7

Concluding remarks

7.1 Summary of the results

In this dissertation, we investigate the formation and dynamics of solar chromospheric jets based on the radiation magnetohydrodynamic (MHD) simulations. The dissertation consists of the development of numerical code (Chapter 2 and 3) and investigation of chromospheric jets (Chapter 4 , 5, and 6).

In Chapter 2, we newly propose a new numerical scheme for the multidimensional MHD simulations. The solar atmosphere is magnetic pressure dominated, highly nonlinear due to the strong shock waves, and turbulent. A robust and high-resolution numerical scheme is required for the dynamic simulations of solar atmosphere. We propose a modified version of the approach by Balsara (2009) to get more cost-effective MHD scheme. The proposed scheme is validated by many test problems.

In Chapter 3, based on the MHD scheme proposed in Chapter 2, we develop a new radiation MHD code for the comprehensive dynamical modeling of solar atmosphere. The effect of the non-local radiation energy transport, Spitzer-type thermal conduction, latent heat of partial ionization and molecule formation, and gravity are implemented to the magnetohydrodynamic code. The numerical algorithm is chosen from the standpoint of the efficiency and compatibility with the massively parallel computation.

In Chapter 4, we investigate the effect of the coronal condition on the scale and dynamics of solar chromospheric jets using the developed radiation MHD code. The higher coronal temperature causes the higher density at the transition region, which leads to the small amplification of shock waves under the density stratification in the chromosphere. The chromospheric jets become shorter under the hot corona. We find that the coronal temperature also affects the deceleration of chromospheric jets. The taller chromospheric jets like spicules tend to obey the ballistic (free-fall) motion. On the other hand, the short chromospheric jets similar to dynamic fibrils sometimes experience the stronger deceleration by the pressure gradient force produced by shock waves.

In Chapter 5, we study the role of magnetic field on chromospheric jets. The scale of chromospheric jets is not strongly affected by the average strength of magnetic field. The inclination of magnetic field in the strong field case reduces the deceleration and produces slightly longer jets. The role of magnetic field becomes important when we focus on the dependence on the local magnetic structure. The expansion of flux tube and lack of strong wave excitation process leads the shorter chromospheric jets above the strong magnetic flux tube. On the other hand, the assembled shock waves between the flux tubes cause stronger perturbation and taller chromospheric jets.

In Chapter 6, we investigate the effect of three-dimensional domain on the scale of chromospheric jets and the relation between jets and photospheric magnetic structure. A cluster of tall chromospheric jets is formed above the strong magnetic field concentrations at the photospheric level. These tall chromospheric jets are driven by the Lorentz force of the strongly entangled chromospheric magnetic field.

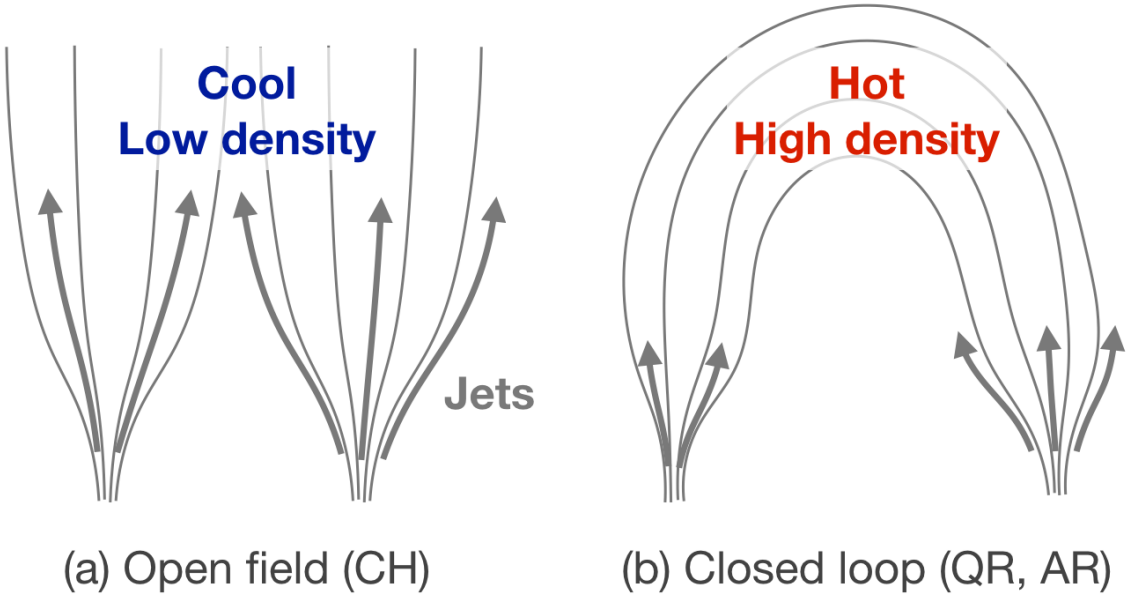

Figure 7.1: Schematic illustration of a scenario on the regional difference of chromospheric jets. Open field regions like in coronal holes (panel (a)) have the cool corona with low density, which produces tall chromospheric jets. The closed loop structure of magnetic field (panel (b)) provides hot and dense coronal plasma, which reduces the scale of chromospheric jets.

7.2 Discussion

7.2.1 Regional difference of chromospheric jets

One of the most important findings in this dissertation is that the coronal temperature and density significantly affect the scale of chromospheric jets (Chapter 4). We also find that the difference of average magnetic field strength does not efficiently change the scale of jets (Chapter 5). These findings suggest a scenario of the regional difference of chromospheric jets as illustrated in Figure 7.1. Open field regions like in coronal holes (panel (a)) have the cool corona with low density by the moderate coronal heating rate and the mass leakage as the solar wind. The cool corona in the open field regions allows strong amplification of chromospheric shock waves and produces tall chromospheric jets. On the other hand, the closed loop structure of magnetic field (panel (b)) allows the efficient coronal heating, which produces hot and dense coronal plasma. The amplification of

chromospheric shock waves is suppressed. Therefore, short chromospheric jets appear below closed coronal loops.

The magnetic field does not directly affect the scale of chromospheric jets in this scenario. It changes the efficiency of coronal heating and resulting temperature and density in the corona, which significantly affects the scale of chromospheric jets. In the open-field regions like coronal holes, the reflection and phase mixing of Alfvén wave, in addition to the shock dissipation, are important for the coronal heating (e.g., Suzuki & Inutsuka, 2005, 2006; Matsumoto & Suzuki, 2012, 2014). The resulting coronas in the previous literatures are relatively cool. In the closed loops observed in quiet and active regions, the magnetic braiding will be more important and produces hot corona (Parker, 1983, 1989; Galsgaard & Nordlund, 1996; Gudiksen & Nordlund, 2005). The length of coronal loops seems to be also related to the heating rate in the corona (Rosner et al., 1978).

We should note the possibility that the scale of the magnetically-driven chromospheric jets like the reconnection-driven jets will be directly controlled by the average strength of the magnetic field. However, Takasao et al. (2013) noted that the amplification of shock waves in the chromosphere is important even if the jets are driven by the magnetic reconnection in the photosphere or chromosphere. This result implies that the coronal condition significantly affects the scale of chromospheric jets even when they are driven by the magnetic energy release in the lower atmosphere. Ishikawa & Tsuneta (2009) reported that the distribution of small magnetic structures formed through the small-scale dynamo process is essentially same in a plage region and a quiet region. An implication of this result is that the average strength of the magnetic field only affects on the large-scale magnetic field but the small-scale magnetic field, which greatly influences the amplitude of the magnetic energy release, remains unchanged. These implications also support our scenario on the regional difference. In three-dimensional simulation (Chapter 6), we find that the entangled magnetic field above the chromospheric swirl plays an important role for the generation of tall chromospheric jets. The numerical simulations of chromospheric swirls (Wedemeyer-Böhm et al., 2012; Kitiashvili et al., 2013; Shelyag et al., 2013) show

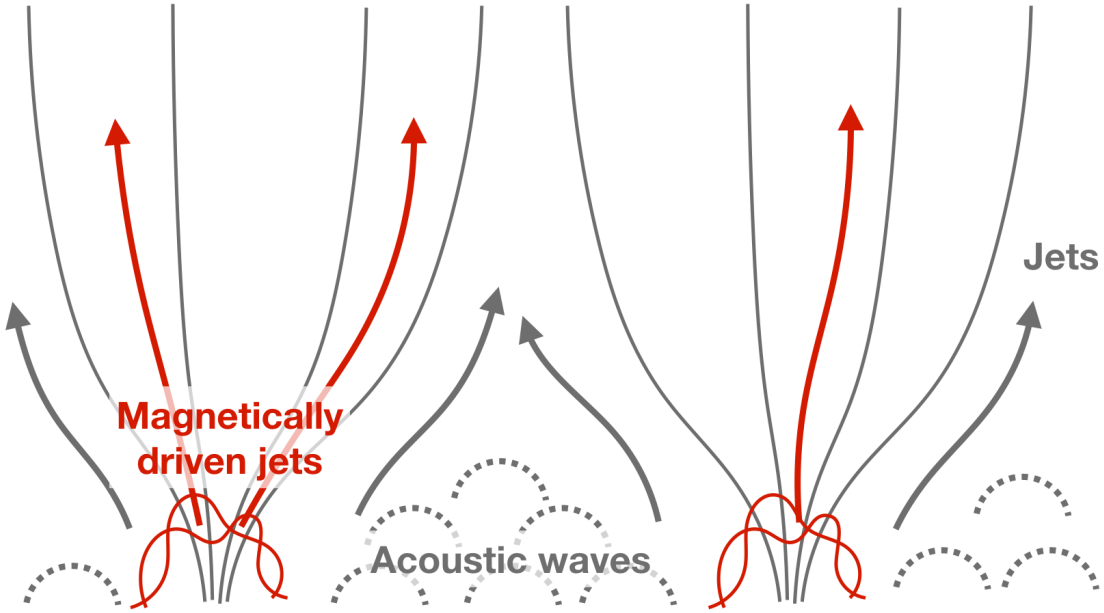

Figure 7.2: Schematic illustration of a scenario on the relation between chromospheric jets and the network magnetic field. The acoustic waves ubiquitously drive the chromospheric jets with the moderate size (black arrows). The complex structure of the magnetic field along the magnetic network drives tall chromospheric jets (red arrows) through the Lorentz force.

the non-negligible dependence of the complexity of the chromospheric magnetic field on the average magnetic field strength. It is possible that the scale of chromospheric jets driven by the torsional motion of flux tube is also affected by the average magnetic field strength.

7.2.2 Relation between chromospheric jets and magnetic network

In this dissertation, we also focus on the relation between chromospheric jets and strong magnetic field concentrations. We find the shorter chromospheric jets above the strong magnetic flux tube in the photosphere in the two-dimensional simulations as described in Chapter 5. On the other hand, the tall chromospheric jets are formed above the photospheric magnetic flux concentrations in the three-dimensional simulation as reported in Chapter 6.

These results implies a scenario on the observational relation between chromospheric

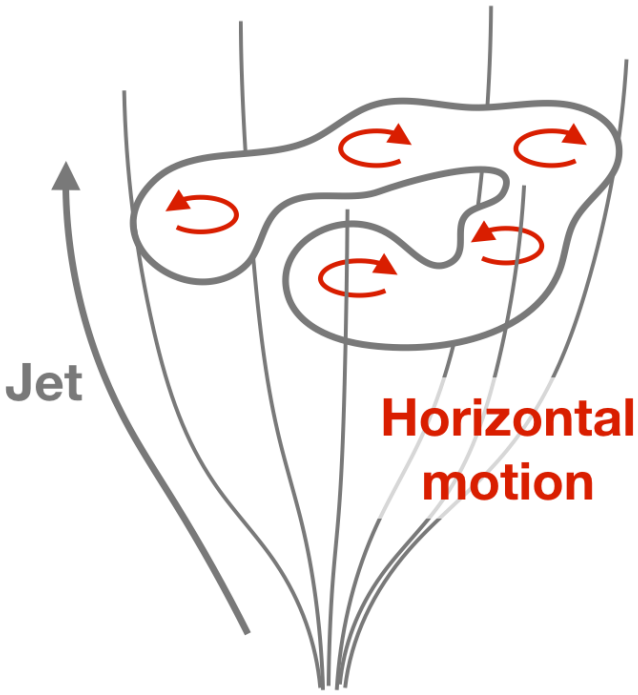

Figure 7.3: Schematic illustration of the horizontal motion of chromospheric jets found in Chapter 6. The cluster of chromospheric jets possesses the fine-scale horizontal structure and turbulent motion (red arrows).

jets and the magnetic network (Suematsu et al., 1995; Langangen et al., 2008b; Tian et al., 2014) as shown in Figure 7.2. The acoustic waves ubiquitously drive the chromospheric jets with the moderate size both along the magnetic network and in the inter-network regions. The generation of acoustic waves directly from the swaying, torsional, or compressive motion is not efficient in the magnetic flux tube. The entangled chromospheric magnetic field is generated by the small-scale motion in the photosphere and lower chromosphere. This complex structure of the magnetic field releases the stored magnetic energy and drives the tall chromospheric jets along the magnetic network.

7.2.3 Formation of horizontal structure

The formation process of the horizontal structure of chromospheric jets, e.g., the horizontal width of jets and the multi-stranded nature of spicules, is one of the most important remaining problems. We successfully reproduce many thin chromospheric jets. Although

the numerical convergence on the horizontal scale of simulated jets is not yet achieved in the current resolution, our simulations motivate us to think about the origin of the horizontal structure of chromospheric jets. Here, we suggest the possible candidates of the formation of the horizontal structure.

The first candidate is the interaction of shock waves and magnetic flux tube discussed in Section 5.4.3. As we have shown, the shock waves produces the spatially localized slow-mode perturbation in the magnetic flux tube through this interaction, which will influence the with of chromospheric jets.

The next candidate is the phase mixing of slow-mode waves in the chromosphere like the one discussed in Heyvaerts & Priest (1983) for the shear Alfvén waves. The small horizontal difference of the slow-mode phase speed in the chromosphere leads the large difference of the time when the shock wave reaches the transition region, which can produce the horizontal structure of chromospheric jets from the temporally and horizontally uniform perturbation in the photosphere.

The beat phenomena by the difference between the lifetime of chromospheric jets and the period of acoustic waves will also produce the horizontal structure of the chromosphere. We sometimes find that only a part of the fan-shaped acoustic waves interacts with the transition region (see figures in Section 5.4.3), because of the large horizontal deformation of transition region, whose horizontal structure will be produced by the former shock-transition region interaction.

In the three-dimensional simulation in Chapter 6, we find that the thinner threads of chromospheric jets form a cluster. This is consistent with the observation of spicules (Suematsu et al., 2008; Skogsrud et al., 2014). The torsional motion inside the cluster illustrated in Figure 7.3 will play an important role for the formation of horizontal structure in the cluster. Skogsrud et al. (2014) suggested that the large-scale swaying motion can also generate the small-scale vortexes as investigated in Antolin et al. (2014) for the coronal loop, which will also contribute the formation of horizontal structure of chromospheric jets.

7.2.4 Driving mechanism of chromospheric jets

In Chapter 4 and 5, we find that the acoustic wave is the dominant driver of the chromospheric jets in the two-dimensional simulations. In the three-dimensional simulation (Chapter 6), although the acoustic waves produce many jets that has properties similar to those in the two-dimensional simulations, we find that the magnetically-driven jets are much taller than the acoustically-driven jets.

In active regions, we speculate that the acoustic wave is the main driver of the dynamic fibrils. The parameter ranges and correlations of the length, lifetime, maximum upward velocity, and deceleration in the two-dimensional simulation with the hot corona (Chapter 4) are sufficiently consistent with the observation of, e.g., De Pontieu et al. (2007a). This speculation is consistent with the arguments in the previous studies (Hansteen et al., 2006; De Pontieu et al., 2007a; Heggland et al., 2007). The remaining problem is how to suppress the scale of the magnetically-driven jets in active regions. Because the Lorentz force can drive tall chromospheric jets, we expect that there exists any mechanism that reduces the frequency or power of the magnetically-driven jets. One possibility is that the magnetic pressure by the strong coronal magnetic field suppresses the formation of complex structure of the chromospheric magnetic field, which is required for the strong magnetic energy release.

We should be more careful for the origin of chromospheric jets in quiet regions and coronal holes. If the two-dimensional effect is not strong for the scale of jets driven by acoustic waves, the acoustic wave can explain at least some part of spicules and mottles. More quantitatively speaking, the chromospheric jets that are shorter than 6 Mm in quiet regions and 8 Mm in coronal holes can be produced by the acoustic waves. However, the taller jets, e.g., of 10 Mm in quiet regions, should be driven by the Lorentz force. Because we analyze only single event of the magnetically-driven jets, the statistical investigation should be undertaken to determine the available parameter range and properties of the magnetically-driven jets. We do not find any indication of the chromospheric jets with

the maximum velocity faster than 100 km/s as reported for the type II spicules (e.g., De Pontieu et al., 2007b). Further investigation is required to determine the origin of tall chromospheric jets, including the type II spicules.

7.2.5 Limitation of the numerical model

The roughest approximation used in our model is the treatment of the chromosphere. The local thermodynamic equilibrium (LTE) equation of states is used to avoid the computational cost required for the simulation with coupling between the radiation and the energy level of atoms. However, many chromospheric lines are in the condition of so-called non-LTE and we should not neglect the coupling between the equation of states and radiation (e.g., Vernazza et al., 1981). As pointed out in Carlsson & Stein (2002), the time scale for the ionization equilibrium in the chromosphere is long, i.e., several minutes to several hours, which is comparable to the time scale of the shock wave propagation and the chromospheric jets. This non-equilibrium effect is important for the non-LTE diagnosis of the chromosphere. For more accurate equation of states, we have to solve the rate equations, the evolution equation of the number density for each state, in combination with the magnetohydrodynamic equations. Moreover, the radiative rate coefficients in the rate equations require the information of the radiative intensity for the particular transitions. Ultimately, we have to solve the non-gray radiative transfer with the effect of partial redistribution and scattering, in combination with the rate equations and MHD equations. This is too computationally high in the three-dimension. There were a few codes that directly solve the hydrodynamic equations with non-LTE radiative transfer and the rate equations (although with many approximation like complete redistribution), such as Carlsson & Stein (1992) and Rammacher & Ulmschneider (2003). The ad-hoc modeling of the radiative rate coefficients to include the effect of the non-equilibrium ionization was also suggested by Sollum (1999) and implemented in the Bifrost code. However, the problem on the wrong convergence was reported (Golding, 2010). Further study is

required in this topic.

The gray approximation in the radiative transfer is assumed from the convection zone to the photosphere. The validity of the gray approximation was investigated by Vögler (2004). They concluded that the gray approximation is sufficient for the modeling of surface convection, but the non-gray multi-group method (Nordlund, 1982; Skartlien, 2000; Vögler et al., 2004) is required for the detailed temperature structure inside the strongly concentrated magnetic flux tube. Skartlien (2000) and Hayek et al. (2010) pointed out that the line scattering is important for the radiative cooling rate from the upper photosphere to the chromosphere. However, the radiative cooling rate in the upper photosphere from the gray approximation is larger than the multi-group method (Vögler, 2004), and the radiative cooling rate by the multi-group method is smaller than the multi-group method without scattering (Skartlien, 2000; Hayek et al., 2010). From these studies, we conclude that our approach of gray non-scattering approximation is sufficiently meaningful to understand the dynamics of the chromospheric jets.

We employ the "effectively optically thin" radiative cooling by Goodman & Judge (2012) for the chromospheric radiative cooling. The other possible choice is the recipe by Carlsson & Leenaarts (2012). However, as pointed out in Carlsson & Leenaarts (2012), the multi-dimensional effect is important for the horizontal variation of the cooling rate. We also note that the chromospheric radiation should be coupled with the equation of states for more accurate solution. The coronal approximation is used for the radiative cooling rate in the transition region and corona. This does not include the effect of the incident radiation heating in the chromosphere caused by the radiation from the transition region and corona (Wahlstrom & Carlsson, 1994). The multi-dimensional effect is also important to this effect (Carlsson & Leenaarts, 2012).

We assume the one-fluid magnetohydrodynamics and do not consider the explicit viscosity nor magnetic diffusion. Cheung & Cameron (2012) and Martínez-Sykora et al. (2012) reported that the slippage between the neutral and ionized particles is important for the chromospheric reconnection (Parker, 1963; Brandenburg & Zweibel, 1994) and heat-

ing in the low temperature region (Martínez-Sykora et al., 2015). However, as pointed out by Martínez-Sykora et al. (2012), the approximation by the generalized Ohm's law (e.g., Pandey & Wardle, 2008) is not sufficient in the chromosphere and the additional evolution equation is required to take account of the drift motion of neutral particles.

There are several ways for the verification of the approximation used in our simulation. The best way is to compare the observable radiative intensity and line profile from our simulation with the observation. This approach requires the non-LTE radiative transfer code and should be investigated in the future. Another way is to compare with the other numerical codes. The comparison of the several famous photospheric convection simulation codes is reported by Beeck et al. (2012). We confirm that our model without the corona is consistent with this report. The verification of the approximation in the upper atmosphere is more difficult. We find that the statistical properties of the chromospheric jets in our two-dimensional simulation (Chapter 4 and 5) with the coronal temperature of 1 MK are consistent with the results by Heggland et al. (2011) that use the Bifrost code. Because many physical processes are included in our code, further studies for more detailed verification should be under taken.

From the limitations mentioned above, we apply the developed code only for the dynamics of the chromosphere and do not apply to the diagnosis. Even with these limitations, the dynamical model with the realistic surface convection provides us new physical insights to the phenomena in the solar chromosphere, as we show for chromospheric jets in this dissertation.

7.3 Future prospect

Before closing this dissertation, we make prospects for the future research. Our new findings on the chromospheric jets and the comprehensive numerical model of the solar atmospheric dynamics allow a wide variety of applications.

7.3.1 Physical aspect

- The relation between the magnetic network and chromospheric jets is one interesting topic for research. The deep convection zone with long integration time is required for the reproduction of the large-scale magnetic structure in the numerical simulation. The inclusion of large-scale convective motion will change the structure of the photospheric magnetic field, which is important for the distribution and formation of chromospheric jets.

- The appropriate treatment of the small-scale dynamo process is also an interesting issue for the simulation of chromospheric jets. As we found in Chapter 6, the complexity of the small-scale magnetic field is important for the production of chromospheric jets. This is a challenging topic because of the large numerical costs to resolve the small-scale dynamo process.

- The formation of horizontal structure is one of the most important issues related to the chromospheric jets. There will be many approaches. One example is to focus on the formation of torsional motion in the chromospheric jets as found in Chapter 6. Not only the photospheric vortex but also the large-scale swaying motion or the reflection and interaction of Alfvén waves will drive the torsional motion.

- The diagnosis of the simulation is crucially important for the accurate comparison with the observation. Especially, to understand the multi-threaded nature of spicules will require the careful treatment of radiative transfer. The nature of type II spicules that fades without falling motion is also an interesting topic for the diagnostic analysis of the simulation.

- It is interesting to extend the focus to wider varieties of chromospheric jets, such as the fine-scale jets in the sunspot penumbra (Katsukawa et al., 2007) and the chromospheric anemone jets (Shibata et al., 2007). Because both jets are observed around the sunspot, the Lorentz force should be more important than the jets studied

in this dissertation. This application will extend our unified understandings for various chromospheric jets.

- The radiation magnetohydrodynamic code developed in this dissertation is designed for the comprehensive dynamical modeling of solar atmosphere. We can apply the code for other phenomena on the sun, such as the Ellerman bombs, prominence, flare, active region formation, etc.

7.3.2 Numerical aspect

- One important next step for the developed code is to implement the non-equilibrium ionization of hydrogen. Because the hydrogen is the most important supplier of election in the chromosphere, the dynamic ionization of hydrogen drastically affects the opacity and radiative intensity. This is an inevitable effect for the realistic diagnostics of simulations.

- The feedback from the non-local radiative transfer to the equation of state through the rate equations should be included in the future. The completely self-consistent treatment of the feedback requires unrealizable numerical costs in the current understanding. Therefore, the efficient and accurate numerical method to treat this effect should be developed.

- The multi-fluid effect will be also important for the future research. The inclusion of the ambipolar magnetic diffusion will enhance the occurrence of magnetic energy release in the chromosphere.

7.4 Conclusion

Since the discovery of spicules (Secchi, 1875; Roberts, 1945), significant amounts of efforts have been made on the observational and theoretical studies of solar chromospheric

jets. This dissertation is devoted to extending our knowledge of the formation and dynamics of solar chromospheric jets using the radiation magnetohydrodynamic simulations. The most important new results in this dissertation are (1) the reproduction of tall ($>$ 6 Mm) chromospheric jets using the simulation with realistic physical processes, (2) the quantification of the effect of the coronal condition and magnetic field on the scale of jets, and (3) the reproduction of the cluster of jets with fine-scale internal structure. We conclude that the solar chromospheric jets reflect the information of not only the magnetic field but also the corona and fine-scale motion in the lower atmosphere.

References

Abbett, W. P. 2007, ApJ, 665, 1469

Alexiades, V., Amiez, G., & Gremaud, P.-A. 1996, Communications in numerical methods in engineering, 12, 31

Anan, T., Kitai, R., Kawate, T., et al. 2010, PASJ, 62, 871

Antolin, P., Yokoyama, T., & Van Doorsselaere, T. 2014, ApJ, 787, L22

Arber, T. D., Haynes, M., & Leake, J. E. 2007, ApJ, 666, 541

Asplund, M., Grevesse, N., & Sauval, A. J. 2006, Communications in Asteroseismology, 147, 76

Asplund, M., Grevesse, N., Sauval, A. J., & Scott, P. 2009, ARA&A, 47, 481

Auer, L. 2003, in Astronomical Society of the Pacific Conference Series, Vol. 288, Stellar Atmosphere Modeling, ed. I. Hubeny, D. Mihalas, & K. Werner, 3

Avrett, E. H., & Loeser, R. 2008, ApJS, 175, 229

Balsara, D. S. 2001, Journal of Computational Physics, 174, 614

Balsara, D. S. 2004, The Astrophysical Journal Supplement Series, 151, 149

Balsara, D. S. 2009, Journal of Computational Physics, 228, 5040

Balsara, D. S. 2010, Journal of Computational Physics, 229, 1970

Balsara, D. S. 2012, Journal of Computational Physics, 231, 7504

Balsara, D. S., & Kim, J. 2004, The Astrophysics Journal, 602, 1079

Balsara, D. S., Meyer, C., Dumbser, M., Du, H., & Xu, Z. 2013, Journal of Computational Physics, 235, 934

Balsara, D. S., Rumpf, T., Dumbser, M., & Munz, C.-D. 2009, Journal of Computational Physics, 228, 2480

Balsara, D. S., & Spicer, D. S. 1999, Journal of Computational Physics, 149, 270

Beckers, J. M. 1963, ApJ, 138, 648

Beckers, J. M. 1968, Sol. Phys., 3, 367

Beckers, J. M. 1972, ARA&A, 10, 73

Beeck, B., Collet, R., Steffen, M., et al. 2012, A&A, 539, A121

Bercik, D. J. 2002, PhD thesis, Michigan State University

Bhavilai, R. 1965, MNRAS, 130, 411

Bogdan, T. J., Carlsson, M., Hansteen, V. H., et al. 2003, ApJ, 599, 626

Borges, R., Carmona, M., Costa, B., & Don, W. S. 2008, Journal of Computational Physics, 227, 3191

Brackbill, J. U., & Barnes, D. C. 1980, Journal of Computational Physics, 35, 426

Brandenburg, A., & Zweibel, E. G. 1994, ApJ, 427, L91

Bruls, J. H. M. J., Vollmöller, P., & Schüssler, M. 1999, A&A, 348, 233

Carlsson, M., & Leenaarts, J. 2012, A&A, 539, A39

Carlsson, M., & Stein, R. F. 1992, ApJ, 397, L59

Carlsson, M., & Stein, R. F. 2002, ApJ, 572, 626

Cheung, M. C. M., & Cameron, R. H. 2012, ApJ, 750, 6

Cheung, M. C. M., Schüssler, M., Tarbell, T. D., & Title, A. M. 2008, ApJ, 687, 1373

Colella, P., & Woodward, P. R. 1984, Journal of Computational Physics, 54, 174

Courant, R., Friedrichs, K., & Lewy, H. 1967, IBM Journal of Research and Development, 11, 215

de Jager, C. 1957, Bull. Astron. Inst. Netherlands, 13, 133

De Pontieu, B. 1999, A&A, 347, 696

De Pontieu, B., Erdélyi, R., & De Moortel, I. 2005, ApJ, 624, L61

De Pontieu, B., Hansteen, V. H., Rouppe van der Voort, L., van Noort, M., & Carlsson, M. 2007a, ApJ, 655, 624

De Pontieu, B., McIntosh, S. W., Hansteen, V. H., & Schrijver, C. J. 2009, ApJ, 701, L1

De Pontieu, B., McIntosh, S., Hansteen, V. H., et al. 2007b, PASJ, 59, 655

Dedner, A., Kemm, F., Kröner, D., et al. 2002, Journal of Computational Physics, 175, 645

Dumbser, M., & Käser, M. 2007, Journal of Computational Physics, 221, 693

Evans, C. R., & Hawley, J. F. 1988, The Astrophysical Journal, 332, 659

Fujimura, D., & Tsuneta, S. 2009, ApJ, 702, 1443

Galloway, D. J., & Weiss, N. O. 1981, ApJ, 243, 945

Galsgaard, K., & Nordlund, Å. 1996, J. Geophys. Res., 101, 13445

Gardiner, T. A., & Stone, J. M. 2005, Journal of Computational Physics, 205, 509

Golding, T. P. 2010, Master's Thesis, University of Oslo

Goldreich, P., Murray, N., & Kumar, P. 1994, ApJ, 424, 466

Goodman, M. L., & Judge, P. G. 2012, ApJ, 751, 75

Gottlieb, S., Ketcheson, D. I., & Shu, C.-W. 2009, Journal of Scientific Computing, 38, 251

Gottlieb, S., Shu, C.-W., & Tadmor, E. 2001, SIAM Review, 43, 89

Gudiksen, B. V., Carlsson, M., Hansteen, V. H., et al. 2011, A&A, 531, A154

Gudiksen, B. V., & Nordlund, Å. 2005, ApJ, 618, 1020

Guerreiro, N., Carlsson, M., & Hansteen, V. 2013, ApJ, 766, 128

Haerendel, G. 1992, Nature, 360, 241

Hansteen, V., Guerreiro, N., De Pontieu, B., & Carlsson, M. 2015, ApJ, 811, 106

Hansteen, V. H., De Pontieu, B., Rouppe van der Voort, L., van Noort, M., & Carlsson, M. 2006, ApJ, 647, L73

Hansteen, V. H., Hara, H., De Pontieu, B., & Carlsson, M. 2010, ApJ, 718, 1070

Hasan, S. S., & Kalkofen, W. 1999, ApJ, 519, 899

Hasan, S. S., & van Ballegooijen, A. A. 2008, ApJ, 680, 1542

Hayek, W., Asplund, M., Carlsson, M., et al. 2010, A&A, 517, A49

Heggland, L., De Pontieu, B., & Hansteen, V. H. 2007, ApJ, 666, 1277

Heggland, L., De Pontieu, B., & Hansteen, V. H. 2009, ApJ, 702, 1

Heggland, L., Hansteen, V. H., De Pontieu, B., & Carlsson, M. 2011, ApJ, 743, 142

Heyvaerts, J., & Priest, E. R. 1983, A&A, 117, 220

Hollweg, J. V. 1982, ApJ, 257, 345

Hollweg, J. V. 1992, ApJ, 389, 731

Hollweg, J. V., Jackson, S., & Galloway, D. 1982, Sol. Phys., 75, 35

Iglesias, C. A., & Rogers, F. J. 1996, ApJ, 464, 943

Iijima, H., & Yokoyama, T. 2015, ApJ, 812, L30

Irwin, A. W. 1981, ApJS, 45, 621

Ishikawa, R., & Tsuneta, S. 2009, A&A, 495, 607

Isobe, H., Proctor, M. R. E., & Weiss, N. O. 2008, ApJ, 679, L57

James, S. P., & Erdélyi, R. 2002, A&A, 393, L11

Jiang, G.-S., & Shu, C.-W. 1996, Journal of Computational Physics, 126, 202

Kato, Y., Steiner, O., Steffen, M., & Suematsu, Y. 2011, ApJ, 730, L24

Katsukawa, Y., Berger, T. E., Ichimoto, K., et al. 2007, Science, 318, 1594

Kawai, S. 2013, Journal of Computational Physics, 251, 292

Kitiashvili, I. N., Kosovichev, A. G., Lele, S. K., Mansour, N. N., & Wray, A. A. 2013, ApJ, 770, 37

Kudoh, T., & Shibata, K. 1999, ApJ, 514, 493

Kunasz, P., & Auer, L. H. 1988, J. Quant. Spec. Radiat. Transf., 39, 67

Kurucz, R. L. 1970, SAO Special Report, 309

Landi, E., Del Zanna, G., Young, P. R., Dere, K. P., & Mason, H. E. 2012, ApJ, 744, 99

Langangen, Ø., Carlsson, M., Rouppe van der Voort, L., Hansteen, V., & De Pontieu, B. 2008a, ApJ, 673, 1194

Langangen, Ø., De Pontieu, B., Carlsson, M., et al. 2008b, ApJ, 679, L167

Leake, J. E., & Arber, T. D. 2006, A&A, 450, 805

Leake, J. E., & Linton, M. G. 2013, ApJ, 764, 54

Leake, J. E., Lukin, V. S., Linton, M. G., & Meier, E. T. 2012, ApJ, 760, 109

Leake, J. E., DeVore, C. R., Thayer, J. P., et al. 2014, Space Sci. Rev., 184, 107

Lee, D., & Deane, A. E. 2009, Journal of Computational Physics, 228, 952

Leenaarts, J., Carlsson, M., Hansteen, V., & Gudiksen, B. V. 2011, A&A, 530, A124

Leighton, R. B., Noyes, R. W., & Simon, G. W. 1962, ApJ, 135, 474

Londrillo, P., & del Zanna, L. 2004, Journal of Computational Physics, 195, 17

Martínez-Sykora, J., De Pontieu, B., & Hansteen, V. 2012, ApJ, 753, 161

Martínez-Sykora, J., De Pontieu, B., Hansteen, V., & Carlsson, M. 2015, Philosophical Transactions of the Royal Society of London Series A, 373, 40268

Martínez-Sykora, J., Hansteen, V., & Carlsson, M. 2008, ApJ, 679, 871

Martínez-Sykora, J., Hansteen, V., De Pontieu, B., & Carlsson, M. 2009, ApJ, 701, 1569

Martínez-Sykora, J., Hansteen, V., & Moreno-Insertis, F. 2011, ApJ, 736, 9

Martínez-Sykora, J., De Pontieu, B., Leenaarts, J., et al. 2013, ApJ, 771, 66

Matsumoto, T., & Suzuki, T. K. 2012, ApJ, 749, 8

Matsumoto, T., & Suzuki, T. K. 2014, MNRAS, 440, 971

McIntosh, S. W., & De Pontieu, B. 2009, ApJ, 707, 524

Meyer, C. D., Balsara, D. S., & Aslam, T. D. 2012, MNRAS, 422, 2102

Meyer, C. D., Balsara, D. S., & Aslam, T. D. 2014, Journal of Computational Physics, 257, 594

Michalitsanos, A. G. 1973, Sol. Phys., 30, 47

Mihalas, D., Auer, L. H., & Mihalas, B. R. 1978, ApJ, 220, 1001

Miyoshi, T., & Kusano, K. 2011, Plasma and Fusion Research, 6, 1124

Moore, R. L., Sterling, A. C., Cirtain, J. W., & Falconer, D. A. 2011, ApJ, 731, L18

Nakamura, N., Shibata, K., & Isobe, H. 2012, ApJ, 761, 87

Nordlund, Å. 1982, A&A, 107, 1

Nordlund, Å., & Stein, R. F. 2001, ApJ, 546, 576

Ôno, Y., Sakashita, S., & Yamazaki, H. 1960, Progress of Theoretical Physics, 23, 294

Osterbrock, D. E. 1961, ApJ, 134, 347

Pandey, B. P., & Wardle, M. 2008, MNRAS, 385, 2269

Pariat, E., Antiochos, S. K., & DeVore, C. R. 2009, ApJ, 691, 61

Pariat, E., Antiochos, S. K., & DeVore, C. R. 2010, ApJ, 714, 1762

Pariat, E., Dalmasse, K., DeVore, C. R., Antiochos, S. K., & Karpen, J. T. 2015, A&A, 573, A130

Parker, E. N. 1963, ApJS, 8, 177

Parker, E. N. 1964, ApJ, 140, 1170

Parker, E. N. 1978, ApJ, 221, 368

Parker, E. N. 1983, ApJ, 264, 642

Parker, E. N. 1989, Sol. Phys., 121, 271

Parnell, C. E., DeForest, C. E., Hagenaar, H. J., et al. 2009, ApJ, 698, 75

Pasachoff, J. M., Jacobson, W. A., & Sterling, A. C. 2009, Sol. Phys., 260, 59

Pereira, T. M. D., De Pontieu, B., & Carlsson, M. 2012, ApJ, 759, 18

Pereira, T. M. D., De Pontieu, B., Carlsson, M., et al. 2014, ApJ, 792, L15

Pietarila, A., Hirzberger, J., Zakharov, V., & Solanki, S. K. 2009, A&A, 502, 647

Pikel'ner, S. B. 1969, Soviet Ast., 13, 259

Pikel'ner, S. B. 1971, Comments on Astrophysics and Space Physics, 3, 33

Powell, K. G., Roe, P. L., Linde, T. J., Gombosi, T. I., & De Zeeuw, D. L. 1999, Journal of Computational Physics, 154, 284

Rammacher, W., & Ulmschneider, P. 2003, ApJ, 589, 988

Rempel, M., Schüssler, M., & Knölker, M. 2009, ApJ, 691, 640

Roberts, W. O. 1945, ApJ, 101, 136

Rogers, F. J., Swenson, F. J., & Iglesias, C. A. 1996, ApJ, 456, 902

Rosenthal, C. S., Bogdan, T. J., Carlsson, M., et al. 2002, ApJ, 564, 508

Rosner, R., Tucker, W. H., & Vaiana, G. S. 1978, ApJ, 220, 643

Rouppe van der Voort, L., Leenaarts, J., De Pontieu, B., Carlsson, M., & Vissers, G. 2009, ApJ, 705, 272

Rouppe van der Voort, L. H. M., De Pontieu, B., Hansteen, V. H., Carlsson, M., & van Noort, M. 2007, ApJ, 660, L169

Rutten, R. J. 2006, in Astronomical Society of the Pacific Conference Series, Vol. 354, Solar MHD Theory and Observations: A High Spatial Resolution Perspective, ed. J. Leibacher, R. F. Stein, & H. Uitenbroek, 276

Rutten, R. J. 2007, in Astronomical Society of the Pacific Conference Series, Vol. 368, The Physics of Chromospheric Plasmas, ed. P. Heinzel, I. Dorotovič, & R. J. Rutten, 27

Ryu, D., Jones, T. W., & Frank, A. 1995, The Astrophysical Journal, 452, 785

Ryu, D., Miniati, F., Jones, T. W., & Frank, A. 1998, The Astrophysical Journal, 509, 244

Schüssler, M. 1990, in IAU Symposium, Vol. 138, Solar Photosphere: Structure, Convection, and Magnetic Fields, ed. J. O. Stenflo, 161

Secchi, A. 1875, Le Soleil, doi:10.3931/e-rara-14748

Sharma, P., & Hammett, G. W. 2007, Journal of Computational Physics, 227, 123

Shelyag, S., Cally, P. S., Reid, A., & Mathioudakis, M. 2013, ApJ, 776, L4

Shibata, K., & Suematsu, Y. 1982, Sol. Phys., 78, 333

Shibata, K., Nakamura, T., Matsumoto, T., et al. 2007, Science, 318, 1591

Shimizu, T. 2015, Physics of Plasmas, 22, 101207

Simon, G. W., & Leighton, R. B. 1964, ApJ, 140, 1120

Singh, K. A. P., Shibata, K., Nishizuka, N., & Isobe, H. 2011, Physics of Plasmas, 18, 111210

Skartlien, R. 2000, ApJ, 536, 465

Skartlien, R., Stein, R. F., & Nordlund, Å. 2000, ApJ, 541, 468

Skogsrud, H., Rouppe van der Voort, L., & De Pontieu, B. 2014, ApJ, 795, L23

Skogsrud, H., Rouppe van der Voort, L., De Pontieu, B., & Pereira, T. M. D. 2015, ApJ, 806, 170

Sollum, E. 1999, Master's Thesis, University of Oslo

Spruit, H. C. 1979, Sol. Phys., 61, 363

Stein, R. F., Lagerfjärd, A., Nordlund, Å., & Georgobiani, D. 2011, Sol. Phys., 268, 271

Stein, R. F., & Nordlund, Å. 1998, ApJ, 499, 914

Stein, R. F., & Nordlund, Å. 2001, ApJ, 546, 585

Steiner, O., Grossmann-Doerth, U., Knölker, M., & Schüssler, M. 1998, ApJ, 495, 468

Sterling, A. C. 2000, Sol. Phys., 196, 79

Sterling, A. C., & Mariska, J. T. 1990, ApJ, 349, 647

Sterling, A. C., Shibata, K., & Mariska, J. T. 1993, ApJ, 407, 778

Strang, G. 1968, SIAM Journal on Numerical Analysis, 5, 506

Suematsu, Y. 1990, in Lecture Notes in Physics, Berlin Springer Verlag, Vol. 367, Progress of Seismology of the Sun and Stars, ed. Y. Osaki & H. Shibahashi, 211

Suematsu, Y., Ichimoto, K., Katsukawa, Y., et al. 2008, in Astronomical Society of the Pacific Conference Series, Vol. 397, First Results From Hinode, ed. S. A. Matthews, J. M. Davis, & L. K. Harra, 27

Suematsu, Y., Shibata, K., Neshikawa, T., & Kitai, R. 1982, Sol. Phys., 75, 99

Suematsu, Y., Wang, H., & Zirin, H. 1995, ApJ, 450, 411

Suresh, A., & Huynh, H. T. 1997, Journal of Computational Physics, 136, 83

Suzuki, T. K., & Inutsuka, S.-i. 2005, ApJ, 632, L49

Suzuki, T. K., & Inutsuka, S.-I. 2006, Journal of Geophysical Research (Space Physics), 111, 6101

Takasao, S., Isobe, H., & Shibata, K. 2013, PASJ, 65, 62

Thomas, R. N. 1948, ApJ, 108, 130

Tian, H., DeLuca, E. E., Cranmer, S. R., et al. 2014, Science, 346, 1255711

Tóth, G. 2000, Journal of Computational Physics, 161, 605

Tsiropoula, G., & Schmieder, B. 1997, A&A, 324, 1183

Tsiropoula, G., Tziotziou, K., Kontogiannis, I., et al. 2012, Space Sci. Rev., 169, 181

Uchida, Y. 1961, PASJ, 13, 321

Uchida, Y. 1969, PASJ, 21, 128

Ulrich, R. K. 1996, ApJ, 465, 436

Vardya, M. S. 1965, MNRAS, 129, 205

Vernazza, J. E., Avrett, E. H., & Loeser, R. 1981, ApJS, 45, 635

Vögler, A. 2004, A&A, 421, 755

Vögler, A., Bruls, J. H. M. J., & Schüssler, M. 2004, A&A, 421, 741

Vögler, A., Shelyag, S., Schüssler, M., et al. 2005, A&A, 429, 335

Wahlstrom, C., & Carlsson, M. 1994, ApJ, 433, 417

Wedemeyer-Böhm, S., Scullion, E., Steiner, O., et al. 2012, Nature, 486, 505

Withbroe, G. L., & Noyes, R. W. 1977, ARA&A, 15, 363

Yang, L., He, J., Peter, H., et al. 2013, ApJ, 777, 16

Yokoyama, T., & Shibata, K. 1995, Nature, 375, 42

Yokoyama, T., & Shibata, K. 2001, ApJ, 549, 1160

Zaqarashvili, T. V., & Erdélyi, R. 2009, Space Sci. Rev., 149, 355

Zhang, Y. Z., Shibata, K., Wang, J. X., et al. 2012, ApJ, 750, 16